CFD Tools for Design and Simulation of Transient Flows in Hypersonic Facilities

P.A. Jacobs, R.J. Gollan, D.F. Potter, D.E. Gildfind, T.N. Eichmann, B.F. O'Flaherty,
School of Mechanical and Mining Engineering, The University of Queensland, Australia.
D.R. Buttsworth
Faculty of Engineering and Surveying, University of Southern Queensland, Australia.
Email: peterj@mech.uq.edu.au

March 24, 2010

Abstract

Shock tunnels and expansion tubes are our tools of choice for producing high-enthalpy flows in aerothermodynamic studies relevant to hypersonic flight. The detailed flow in these machines turns out to be quite complex and computer models are needed to completely and accurately describe the experimental flow properties and to diagnose the gas dynamic behaviour of the machine when developing new operating conditions. We describe a couple of the flow simulation codes that we have written to assist us in our experimental work. The first is a quasi-one-dimensional flow code that is capable of modelling entire free-piston driven facilities, albeit with some significant limitations. The second is a finite-volume flow code that can more accurately capture the strong viscous and thermochemical interactions that affect strongly expanding flows that are an operating characteristic of expansion tube facilities. Some application studies are then described.

1 INTRODUCTION

High flow speeds, in the range of 4 to 10 km/s, are required for the ground-based study of supersonic combustion and the aerothermodynamics of planetary entry. The operation of a continuous wind tunnel producing the requisite flow speeds is problematic. First, it is difficult to design a facility that would bear the sustained heating rates to the tube walls for long periods and, second, the energy requirements for continuous operation are prohibitive. Impulse facilities, such as shock tunnels and expansion tubes, are thus the machines of choice for testing at hypersonic speeds.

The hypersonics research group at The University of Queensland has a number of free-piston driven shock tunnels and expansion tubes designed to produce high-enthalpy, short-duration test flows. These machines have been constructed and operated over the past three decades and there is now a degree of confidence in designing new machines and predicting their behaviour. Although the gas dynamic processes in the machines are dominated by unsteady one-dimensional wave interactions which can be sketched as a *wave diagram*, there are significant secondary processes driven by viscous effects and finite-rate chemical kinetics. To cope with increasing model complexity, a number of flow simulation tools have been developed over the past twenty years to

- assist the design of new machine components such as hypersonic nozzles,
- provide the answers to "What if..." questions in the design of new operating conditions, and to
- be a key component in fully specifying each facility's test flow conditions.

This paper will be limited to describing our efforts in modelling the Drummond shock tunnel and the X2 expansion tube, as well as the computer codes that we use for that modelling. These particular facilities have been selected to demonstrate different capabilities of the simulation tools. The Drummond shock tunnel is a good starting example because relatively simple computational modelling can do a reasonable job of estimating its overall performance. Also, there are complex fluid dynamic interactions associated with the shock reflection process that can be explored in the absence of high-temperature thermochemical effects. The X2 facility is a good example of a high performance machine, and comes with the associated complications of a free-piston driver and significant thermochemical nonequilibrium.

2 THE FLOW FACILITIES

2.1 Small Shock Tunnel

The Small Shock Tunnel (SST) facility (Figure 1) operated by the hypersonics group at UQ is an old shock tube from the Australian Defence Science and Technology Organisation (DSTO) [1] that has been redeveloped into a reflected-shock tunnel. It is also known as the *Drummond* Tunnel after the DSTO researcher responsible for its original construction. The tunnel has been used as (i) a facility for testing new ideas for hypersonic nozzles [2] and diagnosing tunnel operation problems [3]; (ii) a relatively low enthalpy gas dynamics facility for both teaching and research; and (iii) a test facility for the development of laser-based flow diagnostics [4].

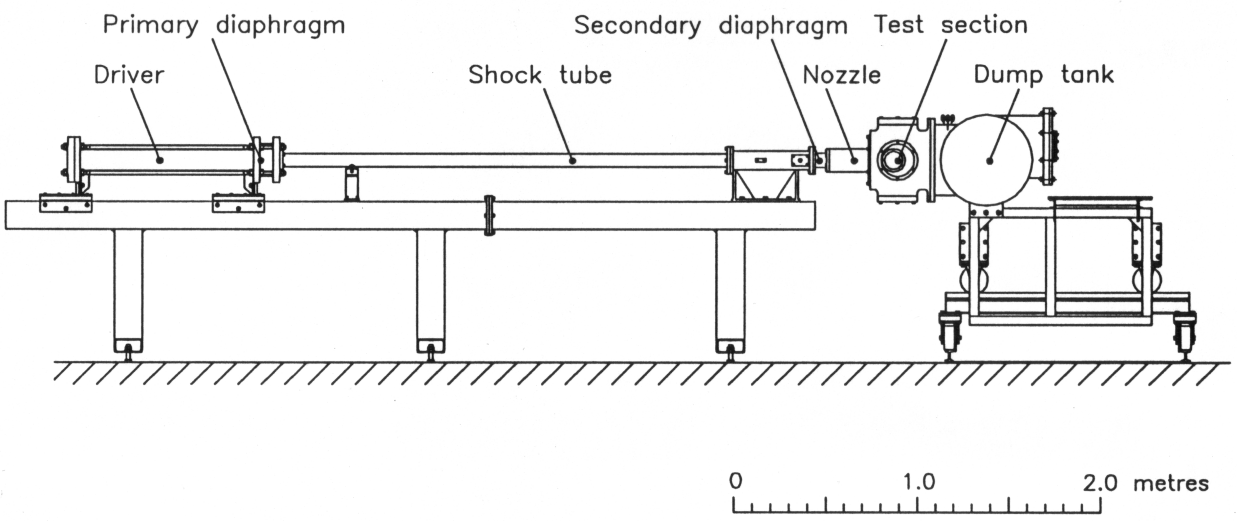

Figure 1: Layout of the small reflected-shock tube known as the Drummond tunnel [2].

The motivation for using the SST facility as a prototyping facility arose from an anomoly seen in the flows produced by large free-piston driven shock tubes. Calibrations of Mach 8 axisymmetric nozzles on both the T4 facility at UQ [5] and the HEG shock tunnel in Göttingen [6] showed significant disturbances in Pitot pressure near the centreline of the test flow. These disturbances occur at the start of the flow period and, for high enthalpies, make much of the test flow unusable. The SST facility was used, together with the `mbcns2` code, to identify the flow disturbance mechanism.

The SST initally operated in a non-reflecting configuration in which the test gas was accelerated by an incident shock and then flowed over the model under test. This produced a high speed but relatively low Mach number ($M \leq 2$) flow in a tube with limited optical access. In order to produce flows with higher

Mach numbers, the facility was modified to include a converging-diverging nozzle and a test section with reasonably large windows. With these additions, the facility is now operated in a reflected-shock mode where the nozzle effectively closes off the downstream end of the shock tube. As shown in Figure 2, the test gas that is processed by the incident shock is brought to rest upstream of the nozzle throat via a reflected shock. This hot, nearly stagnant gas is then expanded through the converging-diverging nozzle to a Mach number of approximately 4 or 7, depending on the nozzle contour. The static temperature in the test flow is quite low for either nozzle so, for generating flows at the high-end of the enthalpy range, we typically use a facility with a free-piston driver.

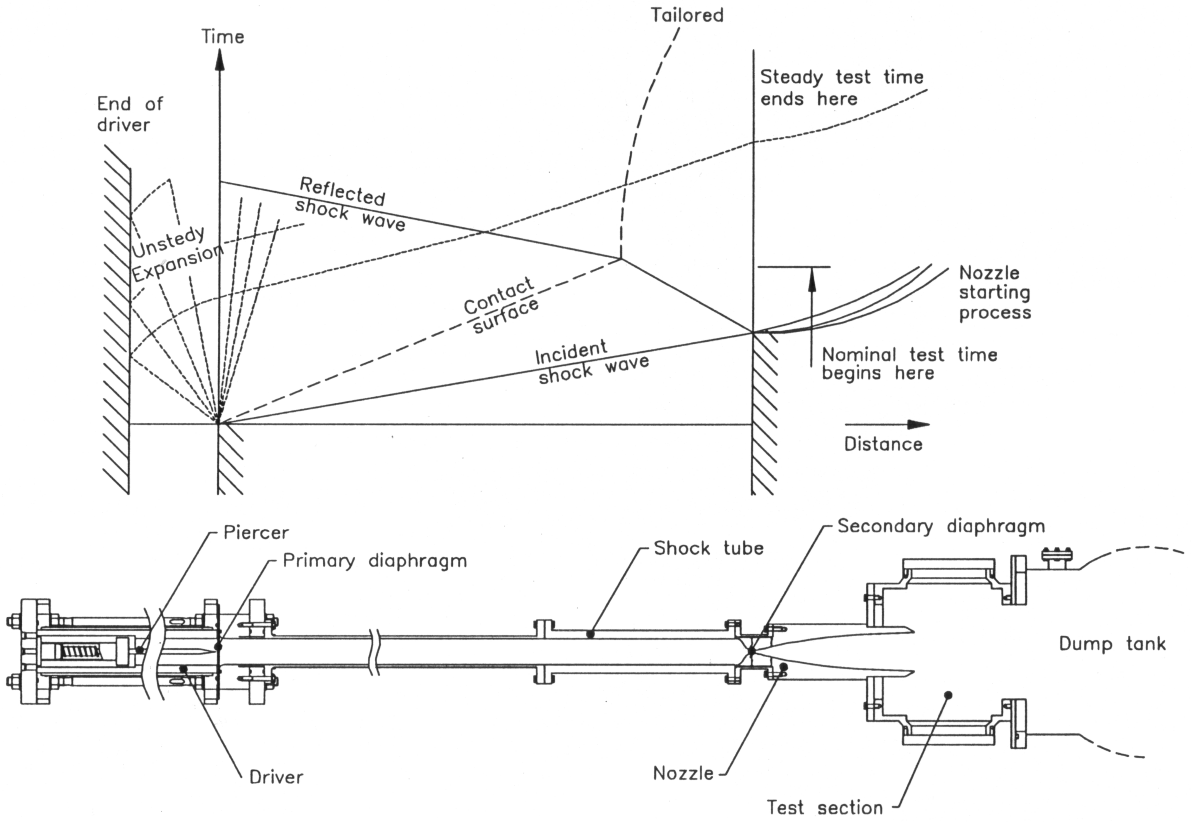

Figure 2: Wave diagram and internal view of the Drummond tunnel [2].

2.2 X2 Expansion Tube

There are three expansion tube facilities at the University of Queensland. In order of their commissioning, and physical size, they are: X1, X2 and X3. The following discussion will focus on the specifics of the X2 facility, though the principles of operation are the same in all three facilities. Much of their recent work has been directed toward the study of the aerothermodynamics of naturally radiating flows.

In expansion tube mode, experiments are performed on subscale models of aeroshell configurations. Because the models in the experiment are scaled, the flow conditions also require appropriate scaling to maintain similarity between the experiment and the true flight conditions. Typically, the product of density and length is kept the same as for the full scale vehicle and, although this provides similarity for some aerothermodynamic processes, the radiative energy exchange scales differently. When it is necessary to study a radiating flow field at exact flight conditions, the expansion tube may be operated in nonreflected shock tube mode. When using nonreflected shock tube mode, there is no subscale model placed in the test

flow. Instead, the object of observation is the relaxing flow immediately behind the shock as it propagates into the test gas. It is helpful to think of this type of experiment as observing the bow shock that is driven by the aeroshell. There is no actual aeroshell driving the shock, rather just high pressure gas generated in the shock tube. The two types of experiment, subscale testing in expansion tube mode and direct observation in nonreflected shock tube mode, are shown in Figure 3.

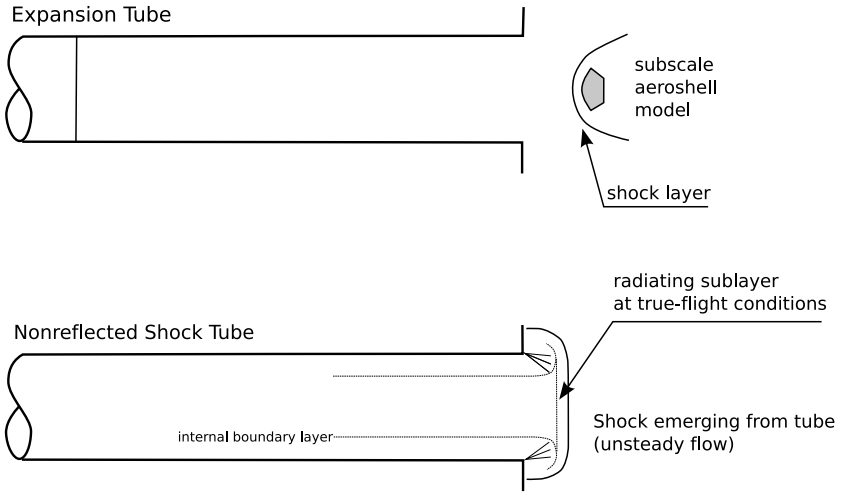

Figure 3: Schematic representation of types of experiments performed in X2 for the study of radiating blunt body flows.

Figure 4 shows a schematic of the X2 facility and a wave diagram of the flow process. The representation in Figure 4 corresponds to use of the facility in expansion tunnel mode. The test gas which eventually passes over the model (or in this diagram, the Pitot rake), initially resides in the shock tube. The gas initially at rest in the acceleration tube is called the accelerator gas. In the diagram, $t = 0$ corresponds to the rupture of the primary diaphragm; at this point the 35 kg piston is nearing the end of its stroke. The primary diaphragm is made of mild steel. Its thickness is varied according to the desired rupture pressure. The rupture of the diaphragm produces a shock, labelled the primary shock. This shock travels through the shock tube compressing and accelerating the test gas. The secondary diaphragm is only very light and so ruptures when the primary shock arrives. The secondary shock propagates into the acceleration tube, its faster speed a consequence of the lower density medium. The compressed test gas now expands, in an unsteady manner, into the acceleration tube. This expansion process drives the low pressure accelerator gas before it. This interface between test gas and accelerator gas is labelled as the contact surface. The test gas expansion is controlled by the pressure of the accelerator gas; a lower pressure accelerator gas results in a stronger expansion. The steady test time, as indicated in Figure 4, is limited by the arrival of a $u + a$ wave from the centred expansion. For further details about the principles of expansion tubes see References [7, 8].

Numerical simulations aid the expansion tube testing by estimating a full set of flow properties that are not directly measurable. For example, numerical simulations help to establish the set of flow conditions in the test gas when operated in expansion tunnel mode. This is important because these are the flow conditions which form the free stream flow for the subscale model; subsequent analysis of the experiment depends on reliable estimates of the free stream flow conditions. An example simulation for a condition in the X2 facility, operated in expansion tube mode is presented in Section 4.4. This simulation targets the 25 MJ/kg CO_2–N_2 operating condition developed in Reference [9] to obtain spectrally resolved radiation intensity measurements of the recompression shock formed over a finite cylinder. The model and optics layout in the test-section is illustrated in Figure 5.

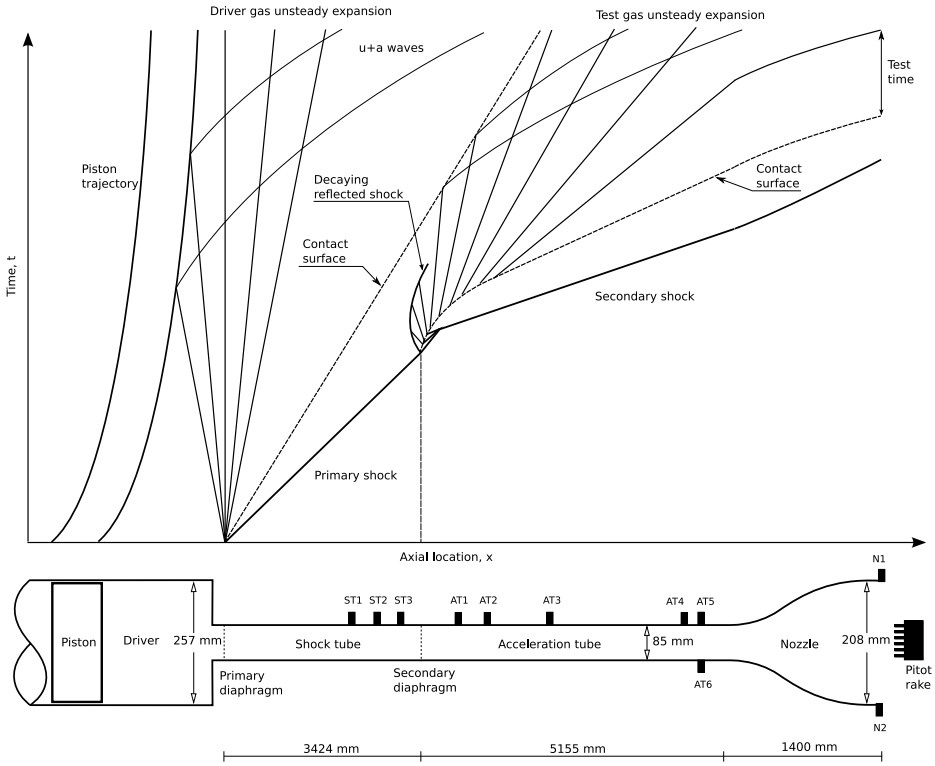

Figure 4: A schematic of the X2 facility configured for expansion tunnel operation. A wave diagram ($x - t$ diagram) shows the flow process.

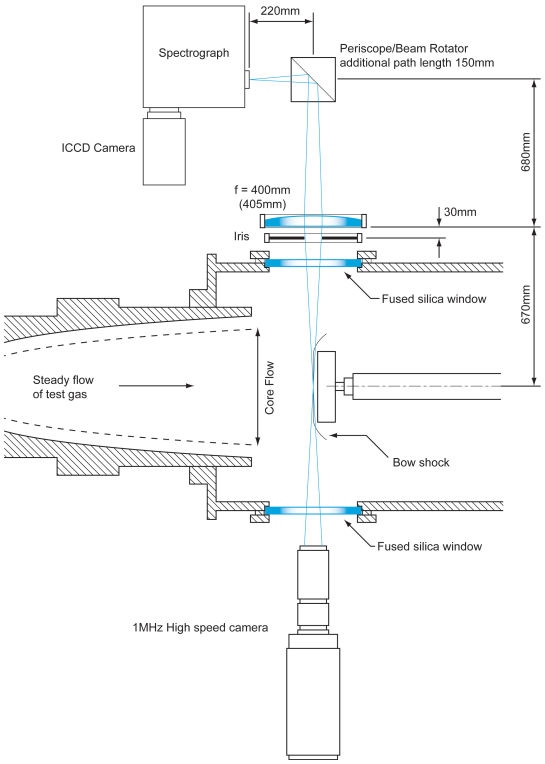

Figure 5: Schematic of bluntbody shock layer spectroscopy experiment with 25mm OD by 102mm cylinder.

The X2 facility is operated as a conventional shock tube when used in nonreflected shock tube mode. Figure 6 shows a schematic of the facility and a wave diagram for the flow process. Prior to $t = 0$, the piston compresses the driver gas which is often a mixture of helium and argon. The rupture of the diaphragm corresponds to $t = 0$ in Figure 6. After diaphragm rupture, the shock then propagates into the shock tube which contains the test gas. The experiment involves making optical measurements of the radiating flow as the shock emerges from the shock tube and into the test section. The section of the flow labelled test time in Figure 6 distinguishes this mode of operation from the expansion tunnel mode: for the nonreflected shock tube mode, the gas immediately behind the primary shock is of interest whereas for the expansion tunnel mode, the test gas has been previously "gathered up" in the shock tube and allowed to expand in the accelerator tube. In the experiments using nonreflected shock tube mode only a small portion of the test gas is of interest, namely, the nonequilibrium radiating gas immediately behind the shock.

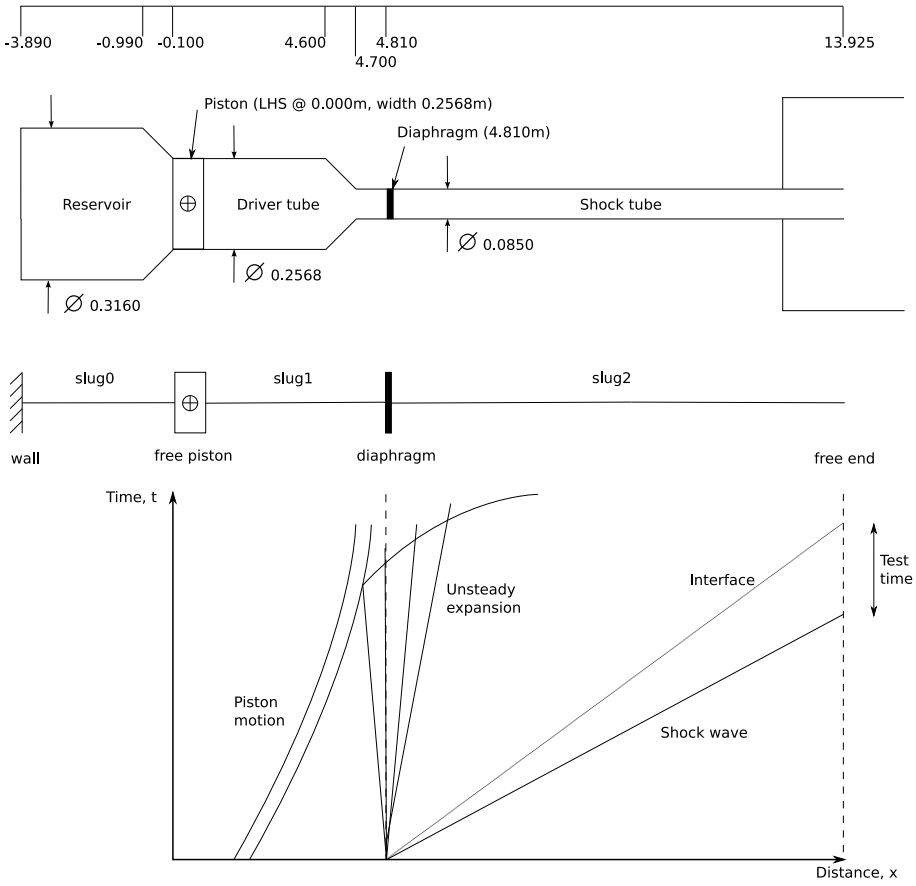

Figure 6: A schematic of the X2 facility configured for nonreflected shock tube operation. A wave diagram ($x - t$ diagram) shows the flow process. *This figure is provided courtesy of Carolyn Jacobs.*

3 THE SIMULATION CODES

Because the experimental facilities are complex multiscale machines, we have a range of codes, each with quite different capability and computational requirements. The codes that will be discussed here are:

- `L1d2`: a simulation code for time-dependent quasi-one-dimensional flows, used to simulate entire facilities with moderate level of detail, and
- `mbcns2`: a time-accurate simulation code for two-dimensional, axisymmetric or planar flows, used when multidimensional effects cannot be separated from the transient flow.

3.1 One-dimensional Flow Code, L1d2

In order to estimate the performance of a free-piston driven impulse facility, one must consider the both the dynamics of the piston and gases, and the viscous effects (including heat transfer) simultaneously. Models which omit these effects require a number of facility-specific fudge factors which can be obtained accurately only after the construction and operation of the facility. This section describes the numerical modelling behind the computer code `L1d2`, which is capable of simulating the (gas-dynamic) operation of a free-piston driven facility during the design process. It is closely related to other light-gas gun codes (see e.g. [10], [11], [12], [13], [14]) and borrows a number of ideas from some of them. The principal features of the code are:

- Quasi-one-dimensional formulation for the gas-dynamics. There is only one spatial coordinate but gradual variation of duct area is allowed.
- The ability to simulate several independent (or interacting) slugs of gas. Also, several pistons/projectiles and multiple diaphragms may be included. Coupling to the gas dynamics is via the boundary conditions of the gas slugs.
- A Lagrangian discretization of the gas slugs. This is done by dividing each gas slug into a set of control-masses (or gas particles) and following the positions of these particles.
- Nominal second-order accuracy in both space and time combined with a robust shock-capturing scheme. The use of a shock capturing scheme means that the same set of equations is used to compute the motion of the gas whether a shock is present or not. This simplifies the code (as shocks do not need to be explicitly identified or tracked) and is especially important in situations where shocks may form from the merger of finite compression waves and where multiple shocks and contact surfaces interact in a complicated manner. It also results in a smearing of the shocks over a couple of computational cells. However, in practice, this is not a problem as any smeared shocks can be sharpened by increasing the grid resolution.
- Viscous effects are included using the standard engineering correlations for friction and heat transfer in pipe flow. Although these correlations are generally derived for steady incompressible flow, they seem to perform adequately in the simulations where the flows are predominantly unsteady and are very compressible.

The general procedure for modelling a specific facility (or system) is to divide the facility into its component parts such as the tube, pistons, diaphragms and volumes of gas (i.e. gas slugs). The description of each component is formulated separately and components allowed to interact through boundary conditions. The core of `L1d2` is a time-stepping loop which first applies the specified boundary conditions and then advances the state of the entire system forward in time by a small increment (or time step). The generic components described in the following sections include a slug of compressible gas, a piston and a diaphragm.

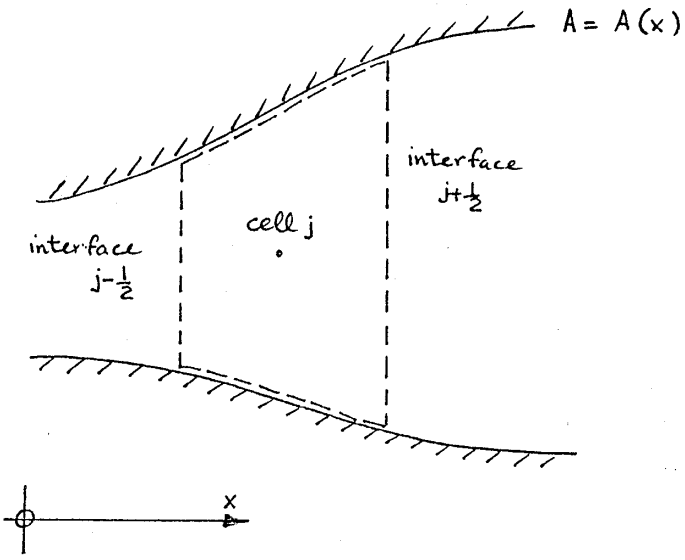

Figure 7: A typical control-mass or Lagrangian cell.

3.1.1 Gas Dynamics

Each slug of gas is treated in a Lagrangian framework in which the slug is divided into a number of control-mass elements (or cells) moving in a variable-area duct. Flow in one dimension only is considered and any area changes in the tube area are assumed to be gradual. Although the boundary layer along the tube wall is not completely modelled in the formulation of the gas-dynamic equations, some of its effects are modelled in the momentum equation by the addition of a wall shear stress. These approximations are arguably the most troublesome part of the modelling process as they cannot be fixed later by simply increasing the grid resolution.

Figure 7 shows a typical control-mass cell (labelled j) with interfaces (labelled $j-\frac{1}{2}$ and $j+\frac{1}{2}$) to adjacent cells. At each interface, the Lagrangian description equates the local fluid velocity to the interface velocity as

$$\frac{dx_{j\pm\frac{1}{2}}}{dt} = u_{j\pm\frac{1}{2}} \quad , \tag{1}$$

where x is the position of the interface and u is the local gas velocity computed with a Riemann solver (to be described later).

The average density within the cell is given by

$$\overline{\rho_j} = \frac{m_j}{\overline{A_j}\left(x_{j+\frac{1}{2}} - x_{j-\frac{1}{2}}\right)} \quad , \tag{2}$$

where $\overline{(\cdots)}$ represents a cell average, A is the area of the duct and m_j is the (constant) mass of gas in cell j.

The rate of change of momentum in the cell is due to the pressure forces acting on the cell interfaces and viscous forces acting at the duct wall. It is given by

$$\frac{d}{dt} m_j \overline{u_j} = \left[P_{j-\frac{1}{2}} A_{j-\frac{1}{2}} - P_{j+\frac{1}{2}} A_{j+\frac{1}{2}} + \overline{P_j}\left(A_{j+\frac{1}{2}} - A_{j-\frac{1}{2}}\right) - \overline{F_{wall}} - \overline{F_{loss}}\right] \quad , \tag{3}$$

where F_{wall} is the shear friction force at the wall and F_{loss} is an effective body-force due to pipe-fitting losses, for example. Evaluation of these loss terms will be discussed in the viscous effects section 3.1.2.

The rate of change of energy within the cell is due to the work done at the cell interfaces plus the heat transferred through the duct wall. It is given by

$$\frac{d}{dt} m_j \overline{E_j} = \left[P_{j-\frac{1}{2}} A_{j-\frac{1}{2}} u_{j-\frac{1}{2}} - P_{j+\frac{1}{2}} A_{j+\frac{1}{2}} u_{j+\frac{1}{2}} + \overline{q_j} \right] \ , \tag{4}$$

where $E = e + \frac{1}{2}u^2$ is the total specific energy of the gas and q is the rate of heat transfer into the cell. Evaluation of q will appear later in section 3.1.2. Note that there is no shear stress term in the total energy equation. This is because the energy removed from the kinetic energy component by the wall shear stress is deposited into the internal energy component of the gas near the wall and, since there is no transfer of mass from one cell to the next, the total energy of the cell is unchanged (by this mechanism).

The governing differential equations for the gas dynamics (i.e. equations (1), (3) and (4)) are completed by specifying the thermodynamic properties of the gas as described in Section 3.3.

3.1.2 Viscous Effects

The viscous shear force on a gas cell is given by

$$\overline{F_{wall}} = \tau_0 \, \pi \, \overline{D} \, (x_{j+\frac{1}{2}} - x_{j-\frac{1}{2}}) \ , \tag{5}$$

where τ_0 is the local shear stress at the wall and $\overline{D}$ is the (average) effective diameter of the tube. Assuming a circular cross-section

$$\overline{D} = 2 \, (\overline{A}/\pi)^{1/2} \ . \tag{6}$$

The wall shear stress is obtained from the Darcy formula for for steady incompressible flow (see e.g. [15, 16])

$$\tau_0 = \frac{-\rho \, f \, u \, |u|}{8} \ , \tag{7}$$

where f is the Darcy-Weisbach friction factor. With minor changes, we follow [13] and use

$$\begin{aligned} f &= \frac{64}{\Lambda \, Re} \ , \quad Re < 2000 \ , \\ f &= \frac{0.032}{\Lambda} \left[\frac{Re}{2000} \right]^{0.3187} \ , \quad 2000 \le Re \le 4000 \ , \\ f &= \frac{1}{\Lambda} \left[1.14 - 2 \log_{10} \left(21.25 \, Re^{-0.9} + \frac{\epsilon}{D} \right) \right]^{-2} \ , \quad Re > 4000 \ , \end{aligned} \tag{8}$$

where the Re is the local Reynolds number based on tube diameter

$$Re = \frac{\rho^* \, D \, |u|}{\mu^*} \ , \tag{9}$$

and ϵ is the absolute wall roughness. The explicit expression for f for the turbulent regime is taken from [17] and is within 1% of the well known Colebrook-White equation. For Reynolds numbers up to 10^5 in shock-tube type flows, it is reasonable to assume a smooth wall and use

$$f = \frac{1}{\Lambda} \left[1.8 \log_{10}(Re) - 1.5147 \right]^{-2} \ , \quad Re > 4000 \ . \tag{10}$$

The properties μ^* and $\rho^* = \rho T / T^*$ are evaluated at the Eckert reference temperature (see e.g. [18] section 5.12)

$$T^* = T + 0.5(T_w - T) + 0.22(T_{aw} - T) \ , \tag{11}$$

where T is the cell-average temperature, T_w is the specified wall temperature and

$$T_{aw} = \Lambda\, T \quad . \tag{12}$$

is the adiabatic wall temperature. Since, we are interested in flows which may have very high Mach numbers, a compressibility correction is applied via the the compressibility factor [19]

$$\Lambda = 1 + \frac{(\gamma - 1)}{2}\, \Omega\, M^2 \quad , \tag{13}$$

where M is the local Mach number and Ω is the recovery factor. Although the compressibility factor Λ in equations (8) and (10) was suggested for rough surfaces, we have used it to adjust the friction factor for all values of Re. For laminar flow (i.e. $Re < 2000$), the recovery factor is set to $\Omega = (Pr)^{1/2}$ while, for turbulent flow, $\Omega = (Pr)^{1/3}$.

Pressure losses due to sudden changes in tube cross-section are computed for each cell as

$$\overline{F_{loss}} = \frac{\Delta P_{loss}}{L_{loss}}\, \overline{A}\, (x_{j+\frac{1}{2}} - x_{j-\frac{1}{2}}) \quad , \tag{14}$$

where

$$\Delta P_{loss} = -K_L\, \frac{1}{2}\, \rho\, u\, |u| \quad , \tag{15}$$

and L_{loss} is the length of tube over which the pressure loss is distributed. Values of K_L/L_{loss} are stored along with the cross-sectional area for the tube. For a contraction and a diaphragm station, we use $K_L = 0.25$.

Heat transfer into a gas cell is given by ([18], section 5.12)

$$q = h\, \pi\, \overline{D}\, (x_{j+\frac{1}{2}} - x_{j-\frac{1}{2}})\, (T_w - T_{aw}) \quad , \tag{16}$$

where the heat transfer coefficient is

$$h = \rho\, C_p\, |u|\, St \tag{17}$$

and the Stanton number is given by the modified Reynolds analogy for turbulent flow in pipes ([18], section 6.2)

$$St = \frac{f}{8}\, Pr^{-2/3} \quad . \tag{18}$$

The dynamic viscosity of the gas is given by the Sutherland expression

$$\mu = \mu_0 \left(\frac{T}{T_0}\right)^{3/2} \left(\frac{T_0 + S_1}{T + S_1}\right) \quad , \tag{19}$$

where values of μ_0, T_0 and S_1 are given by the thermochemistry module. The viscosities for mixtures of gases is obtained from Wilke's [20] expression

$$\mu_{mix} = \sum_{s=1}^{N} \frac{f_s\, \mu_s}{MW_s\, \Phi_s} \quad , \tag{20}$$

where

$$\Phi_s = \sum_{s'=1}^{N} \frac{f_{s'}}{MW_{s'}} \left[1 + \left(\frac{\mu_s}{\mu_{s'}}\right)^{1/2} \left(\frac{MW_{s'}}{MW_s}\right)^{1/4}\right]^2 \left[8\left(1 + \frac{MW_s}{MW_{s'}}\right)\right]^{-1/2} \quad . \tag{21}$$

Following [13], the Prandtl number is given approximately as

$$Pr = \frac{20\gamma}{39\gamma - 15} \quad . \tag{22}$$

3.1.3 Data Structures

Data for each slug of gas is stored in a data structure (called "slug_data") which contains an array of "L_cell" structures (one element for each Lagrangian cell) and other data such as boundary flags and time step information. Each Lagrangian cell (L_cell) structure contains the location of the cell midpoint, the location of the interface to the right, the mass contained by the cell, a cell average of the local flow state, and time derivatives of the state variables. Full details may be obtained from the header file "l1d.h".

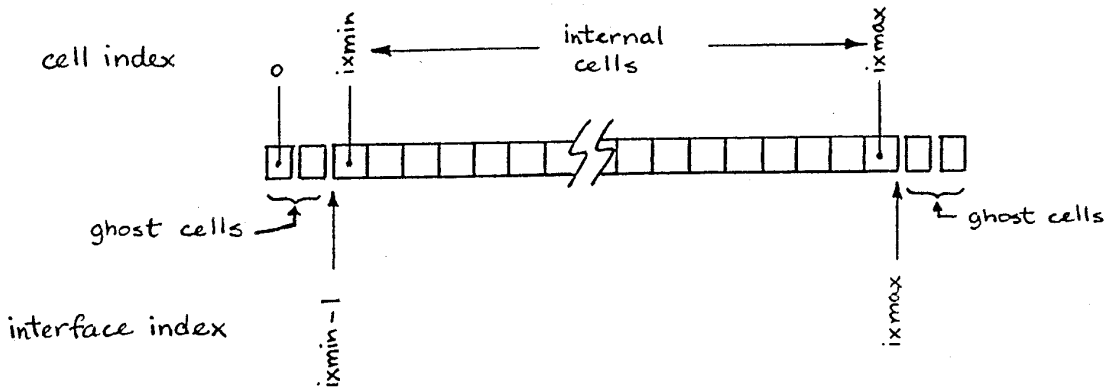

Figure 8: Data storage for a single slug of gas. The indexing for the cells is shown above the array while the indexing scheme for the interfaces is shown below.

Figure 8 shows the indexing arrangement for the cells within each slug data structure. The array consists of both internal cells ($ixmin \le ix \le ixmax$) and ghost cells at each end ($ixmin-2$, $ixmin-1$, $ixmax+1$, $ixmax+2$). The ghost cells lie outside the physical gas slug and contain data used in the application of the boundary conditions.

3.1.4 Internal-Interface Pressures and Velocities

The pressures and velocities used in equations (3) and (4) are obtained by first interpolating the flow state (consisting of a set of values for ρ, u, v, e, P, a) from the cell centres to either side of each interface at the start of the time step and then applying a Riemann solver to estimate the flow states at the interfaces during the time step.

The state of the flow either side of each interface "L" and "R" is interpolated (or reconstructed) from the set of cell averaged states by assuming a linear variation of the variables within cells. This interpolation is performed separately for each primary variable. For example, the density either side of interface $(j+\frac{1}{2})$ is obtained by a nonlinear interpolation (or reconstruction) using the expressions

$$\begin{aligned} \rho_L &= \rho_j + (x_{j+\frac{1}{2}} - x_j)\,\mathrm{MINMOD}((\Delta-)_j, (\Delta+)_j) \ , \\ \rho_R &= \rho_{j+1} + (x_{j+\frac{1}{2}} - x_{j+1})\,\mathrm{MINMOD}((\Delta-)_{j+1}, (\Delta+)_{j+1}) \ , \end{aligned} \tag{23}$$

where

$$\begin{aligned} (\Delta-)_j &= \frac{\rho_j - \rho_{j-1}}{x_j - x_{j-1}} \ , \\ (\Delta+)_j &= \frac{\rho_{j+1} - \rho_j}{x_{j+1} - x_j} \ , \end{aligned} \tag{24}$$

represent two possible estimates of the slope of the density for cell j and x_{j-1}, x_j, x_{j+1} are the midpoints of the cells $j-1$, j and $j+1$ respectively. The MINMOD limiter function selects the slope with the minimum magnitude if both slopes have the same sign and returns zero otherwise (see e.g. [21]).

Interpolation for the other variables is done similarly. To make the code more robust, the conditions $\rho_L, \rho_R \geq \rho_{MIN}$ and $e_L, e_R \geq e_{MIN}$ are imposed after interpolation but before the application of the Riemann solver. Details of the Riemann solver are already available in [22], but for completeness and because the solver is related to the implementation of the specified-velocity boundary condition, a complete description is included here.

The Riemann solver used here is a 2-stage approximate solver in which the first stage computes the intermediate pressure and velocity assuming isentropic wave interaction. A second stage, based on the strong-shock relations, may be invoked to improve the first-stage estimate if the pressure jumps across either wave are sufficiently large. In practice, this modification has been required only in extreme conditions [22]. If stage 2 (strong shock modification) is not invoked, the solver is much like Osher's approximate Riemann solver [23].

STAGE 1: The first stage of the Riemann solver assumes that a spatially constant left state (subscript L) and right state (subscript R) interact through a pair of finite-amplitude (and isentropic) compression or rarefaction waves. Perfect gas relations ([24] cited in [25]) are used to obtain the intermediate states (L^*, R^*) in the gas after the passage of left-moving and right-moving waves, respectively. The expressions implemented in the code are

$$P_L^* = P_R^* = P^* = P_L \left[\frac{(\gamma-1)(\overline{U}_L - \overline{U}_R)}{2a_L(1+Z)} \right]^{2\gamma/(\gamma-1)} , \tag{25}$$

and

$$u_L^* = u_R^* = u^* = \frac{\overline{U}_L Z + \overline{U}_R}{1+Z} , \tag{26}$$

where the Riemann invariants are

$$\begin{aligned} \overline{U}_L &= u_L + \frac{2a_L}{\gamma-1} , \text{ and} \\ \overline{U}_R &= u_R - \frac{2a_R}{\gamma-1} , \end{aligned} \tag{27}$$

and the intermediate variable Z is given by

$$Z = \frac{a_R}{a_L} \left(\frac{P_L}{P_R} \right)^{(\gamma-1)/(2\gamma)} . \tag{28}$$

In the exceptional situation of $(\overline{U}_L - \overline{U}_R) < 0$, we assume that a (near) vacuum has formed at the cell interface and set all of the interface quantities to minimum values.

STAGE 2: If the pressure jump across either wave is large (say, a factor of 10), then the guess for the intermediate pressure is modified using the strong shock relations.

If $P^* > 10\ P_L$ and $P^* > 10\ P_R$ then both waves are taken to be strong shock waves and the intermediate pressure and velocity can be determined directly as

$$P^* = \frac{\gamma+1}{2} \rho_L \left[\frac{\sqrt{\rho_R}}{\sqrt{\rho_R} + \sqrt{\rho_L}} (u_L - u_R) \right]^2 , \tag{29}$$

and

$$u^* = \frac{\sqrt{\rho_L}\, u_L + \sqrt{\rho_R}\, u_R}{\sqrt{\rho_R} + \sqrt{\rho_L}} . \tag{30}$$

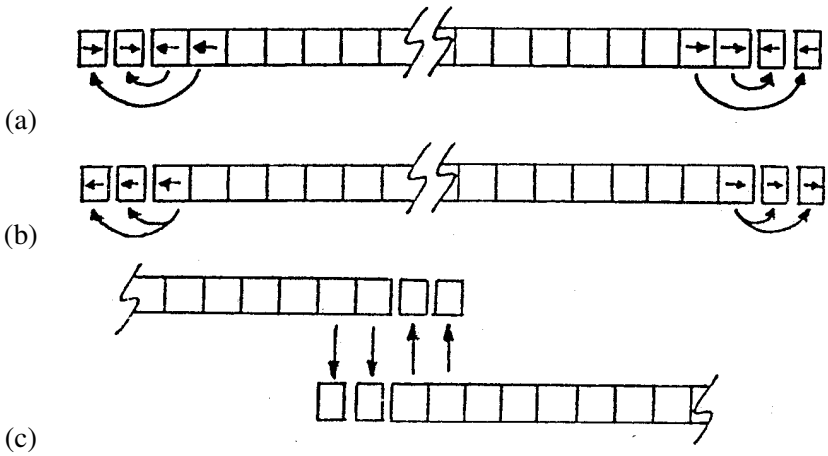

Figure 9: Applying boundary conditions via ghost cells: (a) reflecting end condition; (b) supersonic outflow; (c) gas-gas interface (or direct exchange of data).

If P^* is greater than P_L or P_R (but not both), the stage-1 estimate for P^* can be improved with two Newton-Raphson steps of the form

$$P^*_{n+1} = P^*_n - F_n \left(\frac{dF_n}{dP^*} \right)^{-1} \quad , \tag{31}$$

where

$$F_n = u^*_L(P^*_n) - u^*_R(P^*_n) \quad , \tag{32}$$

and

$$u^*_L = \begin{cases} \overline{U}_L - \frac{2a_L}{\gamma-1} \left(\frac{P^*}{P_L} \right)^{\frac{\gamma-1}{2\gamma}} \quad , & P^* \le 10\, P_L \quad , \\ u_L - \left(\frac{2P^*}{\rho_L(\gamma+1)} \right)^{1/2} \quad , & P^* > 10\, P_L \quad , \end{cases} \tag{33}$$

$$u^*_R = \begin{cases} \overline{U}_R + \frac{2a_R}{\gamma-1} \left(\frac{P^*}{P_R} \right)^{\frac{\gamma-1}{2\gamma}} \quad , & P^* \le 10\, P_R \quad , \\ u_R + \left(\frac{2P^*}{\rho_R(\gamma+1)} \right)^{1/2} \quad , & P^* > 10\, P_R \quad . \end{cases} \tag{34}$$

During the update, we ensure that $P^* \ge P_{MIN}$ where P_{MIN} is some small value. After updating P^*, the intermediate velocity is evaluated using the relevant strong-shock relation from (33) or (34).

The pressure and velocity at each interface may now be substituted back into equations (1), (3) and (4) to give the motion of the cell interfaces and the rate of change of momentum and energy within the cells.

3.1.5 Boundary Conditions

Before interpolation, the inviscid boundary conditions are applied by setting up two layers of ghost cells along each of the boundaries. This is shown schematically in Fig. 9. For a supersonic inflow boundary, all of the ghost-cell quantities are specified as fixed while, for a supersonic outflow boundary, the ghost-cell quantities are extrapolated from active cells just inside the boundary. Solid-wall (i.e. reflective) boundary conditions are applied by setting all of the scalar quantities in the ghost cells equal to those in the active cells adjacent to the boundary but setting the ghost-cell velocities to the negative of the velocities in the active

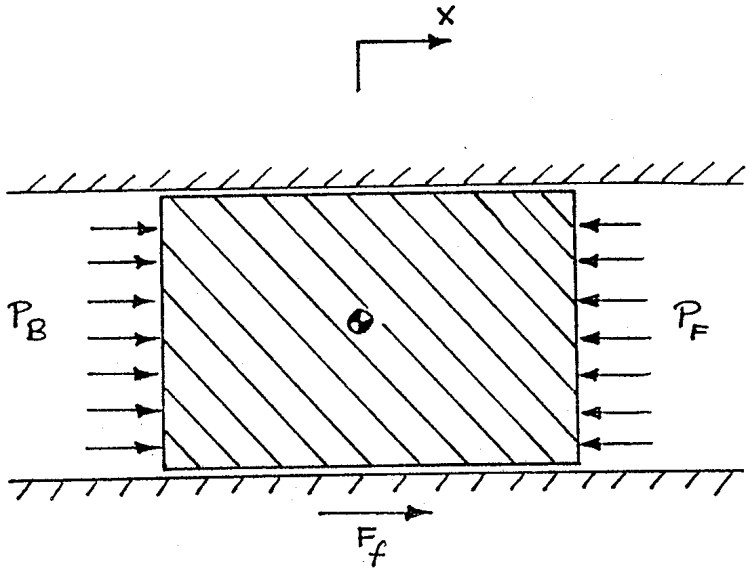

Figure 10: Schematic diagram showing the pressure forces on a piston.

cells. Where two gas slugs interact, data between the two end-cells of the first slug and the corresponding ghost-cells of the second slug are exchanged as shown in Fig. 9.

Where the gas interacts with a piston (or end wall), the boundary-interface velocity u^* is specified. The interface pressure may then be determined from the isentropic relations which, for a right-end boundary, give

$$P^* = \left[(\overline{U}_L - u^*) \frac{(\gamma - 1)}{2\gamma^{1/2}} \left(\frac{\rho_L}{P_L^{1/\gamma}} \right)^{1/2} \right]^{2\gamma/(\gamma-1)} . \tag{35}$$

Similarly, the interface pressure at a left-end boundary is given as

$$P^* = \left[(u^* - \overline{U}_R) \frac{(\gamma - 1)}{2\gamma^{1/2}} \left(\frac{\rho_R}{P_R^{1/\gamma}} \right)^{1/2} \right]^{2\gamma/(\gamma-1)} . \tag{36}$$

3.1.6 Piston Dynamics

Each piston is assumed to have fixed mass (m_p), length (L_p) and frontal area (A_p). The piston state is given by a flag indicating whether the piston is constrained, its centroid position (x_p) and its velocity (V_p). The governing differential equations are

$$\begin{aligned} \frac{d}{dt} x_p &= V_p \ , \\ \frac{d}{dt} V_p &= \frac{1}{m_p} \left[A_p (P_B - P_F) + F_f \right] \ , \end{aligned} \tag{37}$$

where P_B and P_F are the pressures on the "back" and "front" piston faces respectively and F_f is the total frictional force. Refer to Fig. 10 for the general arrangement. If the piston is initially restrained, a specified value of back-face pressure (P_B) must be exceeded before the piston is released.

For the simulation of the X2 facility, the frictional force is assumed to be due to the "chevron" seal near the front face of the piston. The maximum magnitude of the frictional force is

$$|F_f|_{max} = \mu_f A_{seal} P_F \ , \tag{38}$$

where μ_f is the coefficient of friction of the seal material on the tube wall (taken to be 0.2) and A_{seal} is the effective frontal-area of the seal. The actual value of F_f used in equation (37) is

$$F_f = \begin{cases} -sign(V_p)\ |F_f|_{max} & \text{if } (|V_p| \geq V_{tol} \text{ or } |A_p(P_B - P_F)| \geq |F_f|_{max}) \\ -A_p(P_B - P_F) & \text{if } (|V_p| < V_{tol} \text{ and } |A_p(P_B - P_F)| < |F_f|_{max}) \end{cases} \tag{39}$$

where the velocity tolerance is $V_{tol} = 10^{-6}\ m/s$.

3.1.7 Diaphragms

Diaphragms are implemented as a flag for the status of the diaphragm (intact or burst) and a burst pressure. Note that the burst pressure is a "dynamic" burst pressure which may be significantly higher than the burst pressure obtained in hydrostatic rupture tests [26]. The effect of the diaphragm is coded directly into l1d.cxx as a change in boundary conditions selected by the diaphragm's status flag. For example, two gas slugs initially separated by a diaphragm will have reflective boundary conditions applied at the diaphragm station. On rupture, the applied boundary conditions will be changed to a data-exchange condition.

3.1.8 Time Stepping

The state quantities for both pistons and gas slugs are advanced from time level n to time level $n+1$ with the predictor-corrector scheme

$$\begin{aligned} \Delta U^{(1)} &= \Delta t \, \frac{dU^{(n)}}{dt} \ , \\ U^{(1)} &= U^{(n)} + \Delta U^{(1)} \ , \\ \Delta U^{(2)} &= \Delta t \, \frac{dU^{(1)}}{dt} \ , \\ U^{(n+1)} &= U^{(1)} + \frac{1}{2}\left(\Delta U^{(2)} - \Delta U^{(1)}\right) \ , \end{aligned} \tag{40}$$

where the superscripts (1) and (2) indicate intermediate results and $(\frac{dU}{dt})$ includes the rate of change of interface positions, cell momentum, cell energy, piston velocity and piston position. If a first-order scheme is desired, only the first stage is used and $U^{(n+1)} = U^{(1)}$. Although first-order time-stepping requires fewer operations than second-order time-stepping, it is also less robust.

To maintain stability, the time step is restricted to

$$\Delta t \leq \Delta t_{allowed} = CFL\ \Delta t_{signal} \ , \tag{41}$$

where $\Delta t_{allowed}$ is the smallest value for all cells (and all gas slugs) and CFL is the specified Courant-Friedrichs-Lewy number. It is normally restricted to $CFL \leq 0.5$ in the simulations discussed later. For each cell, the inviscid signal time is approximated as

$$\Delta t_{signal} = \frac{\Delta x}{|u| + a} \ . \tag{42}$$

3.2 Axisymmetric Flow Code, mbcns2

For simulating two-dimensional flow fields, we use the code `mbcns2` [27] is an extension of the single-block Navier–Stokes integrator `CNS4U` [28] to structured multiple-block domains. The name `mbcns2` is an acronym for Multiple-Block Compressible Navier-Stokes solver, second version. The code solves the compressible Navier–Stokes equations via a cell-centred time-dependent finite-volume formulation. The governing equations are expressed in integral form over arbitrary quadrilateral cells, with the time rate of change of conserved quantities in each cell specified as a summation of the mass, momentum and energy flux through the cell interfaces. The code is capable of considering both planar and axisymmetric two-dimensional geometries and the thermochemistry module can handle gases in chemical equilibrium or nonequilibrium. When simulating gases with finite-rate chemistry and radiation energy exchange, these physical processes are treated with an operator-split approach. The computational core of `mbcns2` is written in a combination of C and C++, with the option for user-defined functions such as boundary conditions provided as Lua scripts. Preprocessing (*i.e.* grid generation) and postprocessing is handled by a collection of Python programs.

3.2.1 Governing Equations for the Gas Dynamics

The code is formulated around the integral form of the Navier-Stokes equations, which can be expressed as

$$\frac{\partial}{\partial t}\int_V U dV = -\int_S \left(\overline{F}_i - \overline{F}_v\right)\cdot \hat{n}\, dA + \int_V Q dV\,, \tag{43}$$

where S is the bounding surface and $\hat{n}$ is the outward-facing unit normal of the control surface. For axisymmetric flow as considered in the present study, V is the volume and A the area of the cell boundary per unit radian in the radial direction.

The array of conserved quantities is dependent on the thermal model under consideration, and for the thermal nonequilibrium models is

$$U = \begin{bmatrix} \rho \\ \rho u_x \\ \rho u_y \\ \rho E \\ \rho e_{v_m} \\ \rho e_e \\ \rho f_s \end{bmatrix}\,. \tag{44}$$

Here, the conserved quantities are respectively density, x-momentum per volume, y-momentum per volume, total energy per volume, vibrational energy for mode m, electronic-electron energy and mass density of species s. Note that ρe_e includes both bound and free electron energy. We choose to solve both total and all individual species continuity equations to add rigour to our solver: the redundant information gives us a good idea when the numerics are running into trouble. Conversely, when only solving $n-1$ species equations, it is easier for undetected error in mass fractions to accumulate. Thus for 11 species air with 6 vibrating molecules and the inclusion of electrons, for example, there are 22 conserved quantities.

The flux vectors are divided into inviscid and viscous contributions. The inviscid component in thermal nonequilibrium is

$$\overline{F}_i = \begin{bmatrix} \rho u_x \\ \rho u_x^2 + p \\ \rho u_y u_x \\ \rho E u_x + p u_x \\ \rho e_{v_m} u_x \\ \rho e_e u_x + p_e u_x \\ \rho f_s u_x \end{bmatrix}\hat{i} + \begin{bmatrix} \rho u_y \\ \rho u_x u_y \\ \rho u_y^2 + p \\ \rho E u_y + p u_y \\ \rho e_{v_m} u_y \\ \rho e_e u_y + p_e u_y \\ \rho f_s u_y \end{bmatrix}\hat{j}\,, \tag{45}$$

and the viscous component is

$$\overline{F}_v = \begin{bmatrix} 0 \\ \tau_{xx} \\ \tau_{yx} \\ \tau_{xx}u_x + \tau_{yx}u_y + q_x \\ q_{x,v_m} \\ q_{x,e} \\ J_{x,s} \end{bmatrix} \hat{i} + \begin{bmatrix} 0 \\ \tau_{xy} \\ \tau_{yy} \\ \tau_{xy}u_x + \tau_{yy}u_y + q_y \\ q_{y,v_m} \\ q_{y,e} \\ J_{y,s} \end{bmatrix} \hat{j} \; . \tag{46}$$

where the axisymmetric viscous stresses are

$$\begin{aligned} \tau_{xx} &= 2\mu\frac{\partial u_x}{\partial x} + \lambda\left(\frac{\partial u_x}{\partial x} + \frac{\partial u_y}{\partial y} + \frac{u_y}{y}\right) \; , \\ \tau_{yy} &= 2\mu\frac{\partial u_y}{\partial y} + \lambda\left(\frac{\partial u_x}{\partial x} + \frac{\partial u_y}{\partial y} + \frac{u_y}{y}\right) \; , \\ \tau_{xy} = \tau_{yx} &= \mu\left(\frac{\partial u_x}{dy} + \frac{\partial u_y}{dx}\right) \; , \end{aligned} \tag{47}$$

and where the secondary viscosity coefficient λ is expressed in terms of the primary coefficient μ via Stokes hypothesis, $\lambda = -\frac{2}{3}\mu$. The viscous heat fluxes are

$$\begin{aligned} q_x &= k_{tr}\frac{\partial T}{\partial x} + \sum_{s=\text{mol.}} k_{v_s}\frac{\partial T_{v_s}}{\partial x} + k_e\frac{\partial T_e}{\partial x} + \sum_{s=\text{all}} J_{x,s}h_s \; , \\ q_y &= k_{tr}\frac{\partial T}{\partial y} + \sum_{s=\text{mol.}} k_{v_s}\frac{\partial T_{v_s}}{\partial y} + k_e\frac{\partial T_e}{\partial y} + \sum_{s=\text{all}} J_{y,s}h_s \; , \\ q_{x,v_m} &= k_{v_m}\frac{\partial T_{v_m}}{\partial x} + J_{x,m}h_{v_m} \; , \\ q_{y,v_m} &= k_{v_m}\frac{\partial T_{v_m}}{\partial y} + J_{y,m}h_{v_m} \; , \\ q_{x,e} &= k_e\frac{\partial T_e}{\partial x} + \sum_{s=\text{all}} J_{x,s}h_{e_s} \; , \\ q_{y,e} &= k_e\frac{\partial T_e}{\partial y} + \sum_{s=\text{all}} J_{y,s}h_{e_s} \; . \end{aligned} \tag{48}$$

The vector of source terms is separated into geometric, chemistry, thermal energy exchange and radiation contributions in order to apply the operator-splitting integration approach, Eq. 49.

$$Q = Q_{\text{geom.}} + Q_{\text{chem.}} + Q_{\text{therm.}} + Q_{\text{rad.}} \tag{49}$$

The geometric source term vector for axisymmetric geometries is

$$Q_{\text{geom.}} = \begin{bmatrix} 0 \\ 0 \\ (p - \tau_{\theta\theta})\, A_{xy}/V \\ 0 \\ 0 \\ 0 \end{bmatrix} \; , \tag{50}$$

where A_{xy} is the projected area of the cell in the (x,y)-plane and

$$\tau_{\theta\theta} = 2\mu\frac{u_y}{y} + \lambda\left(\frac{\partial u_x}{\partial x} + \frac{\partial u_y}{\partial y} + \frac{u_y}{y}\right) . \tag{51}$$

For planar geometries $Q_{\text{geom.}}$ is a zero vector. See the original ICASE report [28] for a derivation of these terms.

The chemistry source term vector is

$$Q_{\text{chem.}} = \begin{bmatrix} 0 \\ 0 \\ 0 \\ 0 \\ \Omega_m^{VC} \\ \sum_{s=\text{ion.}} \Omega_s^{EC} \\ \dot{\omega}_s \end{bmatrix} , \tag{52}$$

and the thermal energy-exchange source term vector is

$$Q_{\text{therm.}} = \begin{bmatrix} 0 \\ 0 \\ 0 \\ 0 \\ \Omega_m^{VT} + \Omega_m^{VV} + \Omega_m^{VE} \\ \sum_{s=\text{mol.}} \Omega_s^{EV} + \sum_{s=\text{all.}} \Omega_s^{ET} \\ 0 \end{bmatrix} , \tag{53}$$

The radiation source term vector is

$$Q_{\text{rad.}} = \begin{bmatrix} 0 \\ 0 \\ 0 \\ -\nabla \cdot q_{rad} \\ 0 \\ -\nabla \cdot q_{rad} \\ 0 \end{bmatrix} \tag{54}$$

where any purely vibrational component of radiative heat loss (or gain) has been neglected. The transport, thermodynamic and chemical kinetic source term models will be discussed in detail in Section 3.3.

3.2.2 Discretised Equations and Time-Stepping Procedure

The conservation equations are applied to straight-edged quadrilateral cells for which the boundary, projected onto the (x,y)-plane, consists of four straight lines. These lines (or cell interfaces) are labelled North, East, South and West and the integral equation is approximated as the algebraic expression

$$\frac{dU}{dt} = -\frac{1}{V}\sum_{NESW}\left(\overline{F}_i - \overline{F}_v\right)\cdot\hat{n}\,dA + Q\,, \tag{55}$$

where U and Q now represent cell-average values. An operator-splitting approach as advocated by Oran and Boris [29] (see Chapter 11 of their text) is applied whereby the physical mechanisms are applied in a

decoupled fashion. The time integration of the ODE system shown in Eq. 55 is then approximated by

$$\begin{aligned}\int_{\Delta t} \frac{dU}{dt} dt &= \int_{\Delta t} \left(\frac{dU}{dt}\right)_{\text{inv.}} dt + \int_{\Delta t} \left(\frac{dU}{dt}\right)_{\text{visc.}} dt \\ &+ \sum_{N_c} \left[\int_{\Delta t_c} \left(\frac{dU}{dt}\right)_{\text{chem.}} dt\right] + \sum_{N_t} \left[\int_{\Delta t_t} \left(\frac{dU}{dt}\right)_{\text{therm.}} dt\right] , \end{aligned} \tag{56}$$

where,

$$\left(\frac{dU}{dt}\right)_{\text{inv.}} = -\frac{1}{V} \sum_{NESW} \left(\overline{F}_i\right) \cdot \hat{n}\, dA + Q_{\text{geom.}} + Q_{\text{rad.}} , \tag{57}$$

$$\left(\frac{dU}{dt}\right)_{\text{visc.}} = -\frac{1}{V} \sum_{NESW} \left(-\overline{F}_v\right) \cdot \hat{n}\, dA , \tag{58}$$

$$\left(\frac{dU}{dt}\right)_{\text{chem.}} = Q_{\text{chem.}} , \tag{59}$$

$$\left(\frac{dU}{dt}\right)_{\text{therm.}} = Q_{\text{therm.}} . \tag{60}$$

Integration, in time, of the discretised equations proceeds in a *loosely coupled* fashion. The order of operations for a single time-step for a radiating gas in thermochemical nonequilibrium is shown in Figure 11. Some of the chemical kinetic and thermal energy-exchange ODE systems are "stiff" and so "subcycling" is used over the global integration time step via smaller steps if the system fails to solve. The number of chemical and thermal subcycles are,

$$\begin{aligned} N_c &= \Delta t / \Delta t_c , \\ N_t &= \Delta t / \Delta t_t . \end{aligned}$$

Currently the radiative source term vector, Q_{rad}, is applied closely coupled with the inviscid fluxes. This seems to be adequate for the work done thus far, but may need to be revised for strongly radiatively coupled flows.

The advantage of the operator-splitting approach is that the optimal integration scheme for each component of the physics can be implemented. This is especially useful for solving large chemical kinetic systems. The resultant set of ODE systems are integrated in a time via a simple predictor-corrector scheme for the inviscid and viscous increments, one of a selection of methods (including a method for stiff systems) for the chemistry increment (see Section 3.3) and the 4$^{\text{th}}$ order Runge-Kutta-Fehlberg method for the thermal energy-exchange increment.

3.2.3 Multiple-Block Grids, Parallelisation and Boundary Conditions

As shown in Figure 12, the data arrays for each block are dimensioned such that there is a buffer region, two cells deep, around the *active cells*, which completely defines the flow domain covered by the block. The buffer region contains *ghost cells* which are used to hold a copy of the flow information from adjacent blocks or to implement the boundary conditions.

For a boundary common to two blocks, the ghost cells in the buffer region of each block overlap the active cells of the adjacent block. The only interaction that occurs between blocks is the exchange of boundary data, prior to the reconstruction phase of each time step. For the *shared memory* version of the code, the exchange of cell-average data along the block boundaries takes place as a direct copy from the active-cell of one block to the ghost-cell of the other block. Thus, the cells along the common boundary of each block must match in

1. compute gas transport due to inviscid flux:
   (a) apply inviscid boundary conditions or exchange data at boundaries for each block as appropriate
   (b) reconstruct the flow field sate on both sides of each interface
   (c) compute the inviscid fluxes $\overline{F_i} \cdot \hat{n}$
   (d) compute the radiative source term $-\nabla \cdot q_{rad}$ for each cell
   (e) integrate Eq. 57 over the timestep
   (f) decode the conserved quantities via an equation-of-state call
   (g) repeat for corrector update
2. compute gas transport due to viscous flux:
   (a) apply viscous boundary conditions at solid walls
   (b) compute the viscous fluxes as $\overline{F_v} \cdot \hat{n}$
   (c) integrate Eq. 58 over the timestep
   (d) decode the conserved quantities via an equation-of-state call
   (e) repeat for corrector update
3. compute change of gas state due to chemical reactions:
   (a) compute all chemical source terms
   (b) integrate Eq. 59 over the timestep
   (c) decode the conserved quantities via an equation-of-state call
   (d) redo via smaller subcycles if failed and apply call to equation-of-state more frequently
4. compute change of gas state due to thermal energy-exchange:
   (a) compute all chemical source terms
   (b) integrate Eq. 60 over the timestep
   (c) decode the conserved quantities via an equation-of-state call
   (d) redo via smaller subcycles if failed and apply call to equation-of-state more frequently

Figure 11: Sequence of operations for a time-step update in `mbcns2`.

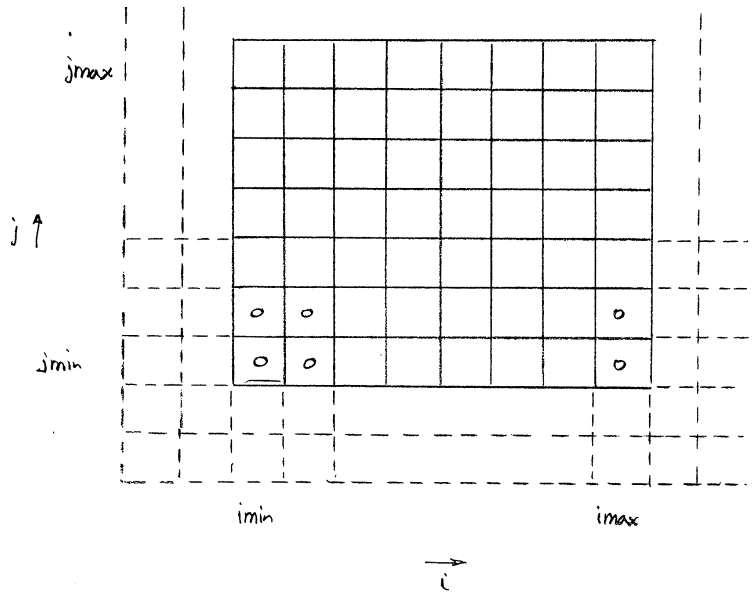

Figure 12: Active and ghost cells for a single block grid for `mbcns2`.

both number and position. Some logic is used within the exchange routines to set the appropriate indexing direction for each boundary. The information on the connections between block boundaries is stored in a (global) connectivity array. For each boundary on each block, this array stores the identity of the adjacent block and the name of the connecting boundary on the adjacent block.

Except for this block to block communication (and the occasional checking of time step magnitudes), the rest of the calculation can be done independently for all blocks. Thus, the algorithm is fairly easy to implement on a multiple-instruction, multiple-data (MIMD) parallel computer and we have a single-program-multiple-data (SPMD) version of the code for computationally-intensive facility calculations as shown in Section 4.4. When running such simulations, there are many copies of the program running independently on separate processors, with each copy of the program handling the computation for a single block. To exchange block-boundary data, each program instance must communicate with the other programs for adjacent blocks. The communication and synchronisation tasks are handled via a standard message passing library: MPI [30].

The inviscid-component of other boundary conditions is also applied via the buffer region of ghost cells. Typically, the tunnel surfaces in the later sections are assigned fixed temperature, no-slip, catalytic (chemical equilibrium at wall gas state) boundary conditions. Such viscous boundary conditions also have a component implemented using data at the cell interfaces that lie along the boundary surface.

3.2.4 Inviscid Flux Calculation

The flow-state at the cell interfaces are calculated using a piecewise-parabolic scheme and then the interface fluxes can then be calculated via an appropriate flux-calculator. When computing the inviscid fluxes at each interface, the velocity field is rotated into a local (n, p)-coordinate system with unit vectors

$$\begin{aligned} \hat{n} &= n_x\,\hat{i} + n_y\,\hat{j} \quad , \\ \hat{p} &= p_x\,\hat{i} + p_y\,\hat{j} \quad , \end{aligned} \tag{61}$$

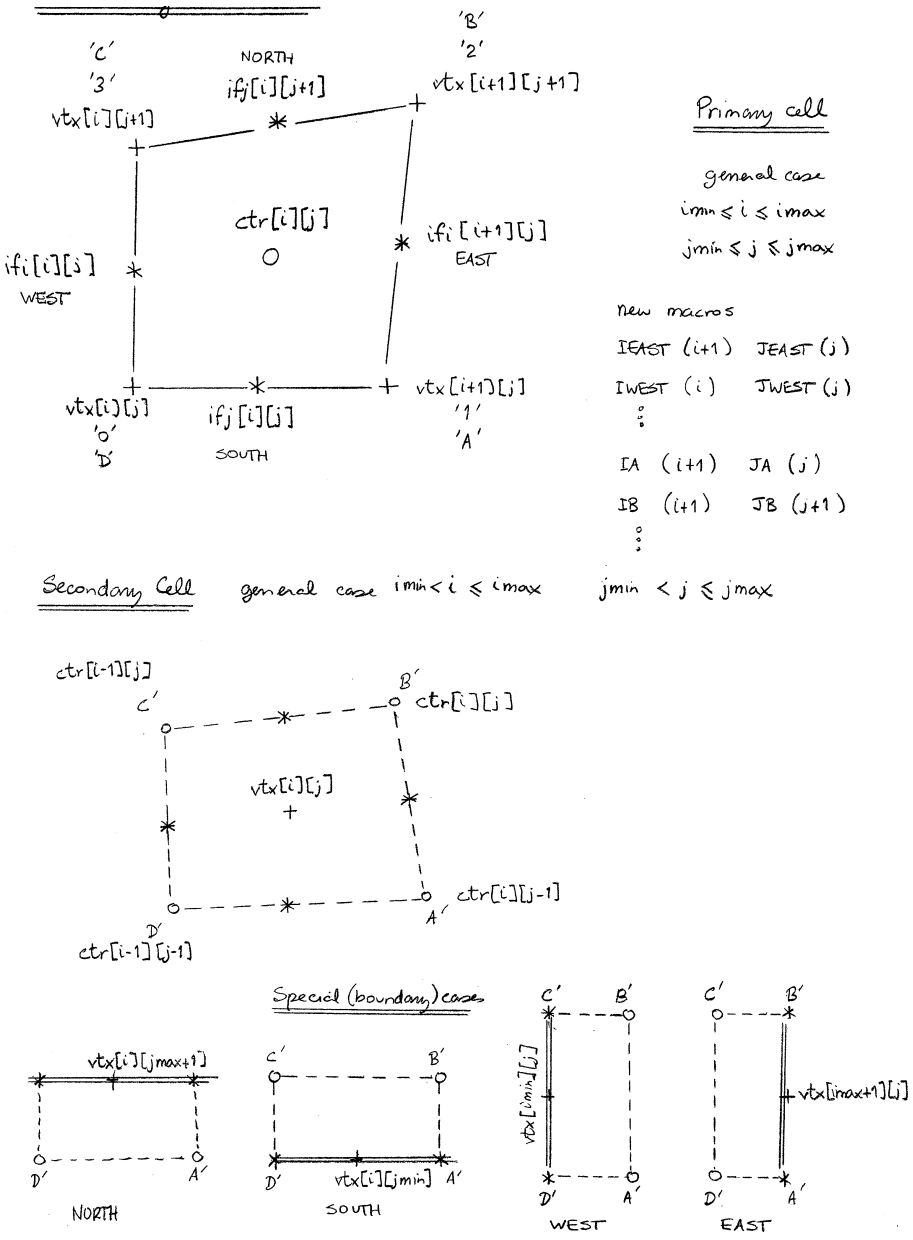

Figure 13: Cell, interface and vertex indexing for `mbcns2`. The upper half of the figure shows the primary cells defining the finite-volumes for the conservation equations. The lower part of the figure shows the secondary cells, used for computing spatial derivatives.

normal and tangental to the cell interface respectively. We have chosen the tangential direction $p_x = -n_y$ and $p_y = n_x$. The normal and tangential velocity components

$$\begin{aligned} u_n &= n_x\, u_x + n_y\, u_y \quad , \\ u_p &= p_x\, u_x + p_y\, u_y \quad , \end{aligned} \tag{62}$$

are then used, together with the other flow properties either side of the interface, to compute the fluxes

$$\begin{bmatrix} F_{mass} \\ F_{n-momentum} \\ F_{p-momentum} \\ F_{energy} \\ F_{species-s} \end{bmatrix} = \begin{bmatrix} \rho u_n \\ \rho u_n u_n + p \\ \rho u_n u_p \\ \rho u_n E + p u_n \\ \rho u_n f_s \end{bmatrix} \quad , \tag{63}$$

in the local reference frame. These are then transformed back to the (x, y)-plane as

$$\overline{F} \cdot \hat{n} = \begin{bmatrix} F_{mass} \\ F_{x-momentum} \\ F_{y-momentum} \\ F_{energy} \\ F_{species-s} \end{bmatrix} = \begin{bmatrix} F_{mass} \\ F_{n-momentum} n_x + F_{p-momentum} p_x \\ F_{n-momentum} n_y + F_{p-momentum} p_y \\ F_{energy} \\ F_{species-s} \end{bmatrix} \quad . \tag{64}$$

For the simulation of shock and expansion tubes, the shock waves can be extremely strong so we use the default adaptive scheme in which the equilibrium flux method (EFM) [31] is applied near shocks and a modified AUSMDV calculator [32] is applied elsewhere.

Reconstruction The primary data held by the code are cell-average data, associated with cell centres. To get the fluxes at cell interfaces, a variable-by-variable reconstruction is made of the flow field. This is done in a one-dimensional fashion, working along one-index direction at a time. *Left* and *Right* values (w_L and w_R respectively) of a flow variable at a cell interface are evaluated as the corresponding cell average value plus a limited higher-order interpolated increment. Given an array of cell-centres $[L1, L0, R0, R1]$ with an interface located between $L0$ and $R0$, the interpolated values are

$$\begin{aligned} w_L &= w_{L0} + \alpha_{L0} \left[\Delta_{L+} \times (2h_{L0} + h_{L1}) + \Delta_{L-} \times h_{R0}\right] s_L \quad , \\ w_R &= w_{R0} - \alpha_{R0} \left[\Delta_{R+} \times h_{L0} + \Delta_{R-} \times (2h_{R0} + h_{R1})\right] s_R \quad , \\ \Delta_{L-} &= \frac{w_{L0} - w_{L1}}{\frac{1}{2}\left(h_{L0} + h_{L1}\right)} \quad , \\ \Delta_{L+} &= \frac{w_{R0} - w_{L0}}{\frac{1}{2}\left(h_{R0} + h_{L0}\right)} = \Delta_{R-} \quad , \\ \Delta_{R+} &= \frac{w_{R1} - wR0}{\frac{1}{2}\left(h_{R0} + h_{R1}\right)} \quad , \\ \alpha_{L0} &= \frac{h_{L0}/2}{h_{L1} + 2h_{L0} + h_{L0}} \quad , \\ \alpha_{R0} &= \frac{h_{R0}/2}{h_{L0} + 2h_{R0} + h_{R1}} \quad , \end{aligned} \tag{65}$$

where the h represents the width of a cell and the van Albada limiter [33] is implemented as

$$\begin{aligned} s_L &= \frac{\Delta_{L-}\Delta_{L+} + |\Delta_{L-}\Delta_{L+}|}{\Delta_{L-}^2 + \Delta_{L+}^2 + \epsilon} \ , \\ s_R &= \frac{\Delta_{R-}\Delta_{R+} + |\Delta_{R-}\Delta_{R+}|}{\Delta_{R-}^2 + \Delta_{R+}^2 + \epsilon} \ , \\ \epsilon &= 1.0 \times 10^{-12} \ . \end{aligned}$$

Finally, minimum and maximum limits are applied so that the newly interpolated values lie within the range of the original cell-centred values. Unlimited, this reconstruction scheme has third-order truncation errors and, with the limiter active, a sine function is reconstructed with an effective truncation error order of 2.7.

Typically, reconstruction is done for density, internal energy, velocity components, and species mass fractions. Other flow quantities that are needed at the interfaces for the inviscid flux calculation are then obtained from the thermochemical model.

EFM Calculation The equilibrium flux method (EFM) [31] is used for its dissipative nature in the vicinity of very strong compressions. The method assumes that the gas is in equilibrium and the molecular velocities of the gas either side of the interface can be described with the Boltzmann distribution. As implemented in Reference [34], the flux of mass from the left state, moving to the right is

$$F_{massL} = W_L^+ \, \rho_L \, u_{nL} + D_L^+ \, \rho_L \, \sqrt{2RT_L} \ , \tag{66}$$

where

$$\begin{aligned} W_L^+ &= \frac{1}{2}\left(1 + \mathrm{erf}\left(\frac{u_{nL}}{\sqrt{2RT_L}}\right)\right) \ , \\ D_L^+ &= \frac{1}{2\sqrt{\pi}}\exp\left(-\left(\frac{u_{nL}}{\sqrt{2RT_L}}\right)^2\right) \ , \\ \mathrm{erf}(s) &= \frac{2}{\sqrt{\pi}}\int_0^s \exp(-t^2)\, dt. \end{aligned} \tag{67}$$

Similarly, the flux of mass from the right state, moving to the left is

$$F_{massR} = W_R^- \, \rho_R \, u_{nR} + D_R^- \, \rho_R \, \sqrt{2RT_R} \ , \tag{68}$$

where

$$\begin{aligned} W_R^- &= \frac{1}{2}\left(1 - \mathrm{erf}\left(\frac{u_{nR}}{\sqrt{2RT_R}}\right)\right) \ , \\ D_R^- &= \frac{1}{2\sqrt{\pi}}\exp\left(-\left(\frac{u_{nR}}{\sqrt{2RT_R}}\right)^2\right) \ . \end{aligned} \tag{69}$$

The flux vector components are then

$$\begin{aligned}
F_{mass} &= F_{massL} + F_{massR} \ , \\
F_{n-momentum} &= F_{massL}\, u_{nL} + F_{massR}\, u_{nR} + W_L^+\, p_L + W_R^-\, p_R \ , \\
F_{p-momentum} &= F_{massL}\, u_{pL} + F_{massR}\, u_{pR} \ , \\
F_{energy} &= \left(W_L^+\, \rho_L\, u_{nL}\right) \left(e_L + \frac{p_L}{\rho_L} + \frac{1}{2}\left(u_{nL}^2 + u_{pL}^2\right)\right) \\
&\quad + \left(W_R^-\, \rho_R\, u_{nR}\right) \left(e_R + \frac{p_R}{\rho_R} + \frac{1}{2}\left(u_{nR}^2 + u_{pR}^2\right)\right) \\
&\quad + \left(D_L^+\, \sqrt{2RT_L}\, \rho_L\right) \left(\frac{1}{2}\left(u_{nL}^2 + u_{pL}^2\right) + \frac{1}{2}\frac{\gamma+1}{\gamma-1} RT_L\right) \\
&\quad + \left(D_R^-\, \sqrt{2RT_R}\, \rho_R\right) \left(\frac{1}{2}\left(u_{nR}^2 + u_{pR}^2\right) + \frac{1}{2}\frac{\gamma+1}{\gamma-1} RT_R\right) \ . \qquad (70)
\end{aligned}$$

Species mass fractions are just transported by the net mass flux as scalar quantities. Note that the gas constants, R and γ, are not really constant; they are density-weighted averages derived from the local values for left and right gas states.

AUSMDV calculation Most of the flow field fluxes are computed with the AUSMDV [32] because of its reasonably low dissipation. The calculation procedure starts by computing the weighting parameters for the velocity splitting

$$\begin{aligned}
\alpha_L &= \frac{2\, p_L/\rho_L}{p_L/\rho_L + p_R/\rho_R} \ , \\
\alpha_R &= \frac{2\, p_R/\rho_R}{p_L/\rho_L + p_R/\rho_R} \ , \qquad (71)
\end{aligned}$$

and the sound speed and Mach numbers in the normal direction to the interface

$$\begin{aligned}
a_m &= \max(a_L, a_R) \ , \\
M_L &= \frac{u_{nL}}{a_m} \ , \\
M_R &= \frac{u_{nR}}{a_m} \ . \qquad (72)
\end{aligned}$$

The components from pressure splitting are then

$$\begin{aligned}
p_L^+ &= \frac{p_L}{4}(M_L+1)^2\,(2-M_L) \ , \ |M_L| \le 1.0 \ , \\
&= \frac{p_L\, du_L}{u_{nL}} \ , \ \text{otherwise} \ , \\
p_R^- &= \frac{p_R}{4}(M_R-1)^2\,(2+M_R) \ , \ |M_R| \le 1.0 \ , \\
&= \frac{p_R\, du_R}{u_{nR}} \ , \ \text{otherwise} \ , \qquad (73)
\end{aligned}$$

where $du_L = \frac{(u_{nL}+|u_{nL}|)}{2}$ and $du_R = \frac{(u_{nR}-|u_{nR}|)}{2}$. The components from the velocity splitting are

$$\begin{aligned}
u_L^+ &= \alpha_L \left(\frac{(u_{nL}+a_m)^2}{4\, a_m} - du_L\right) + du_L \ , \ |M_L| \le 1.0 \ , \\
&= du_L \ , \ \text{otherwise} \ , \\
u_R^- &= -\alpha_R \left(\frac{(u_{nR}-a_m)^2}{4\, a_m} + du_R\right) + du_R \ , \ |M_R| \le 1.0 \ , \\
&= du_R \ , \ \text{otherwise} \ , \qquad (74)
\end{aligned}$$

These components are then combined into a mass flux

$$(\rho u)_{\frac{1}{2}} = u_L^+ \, \rho_L + u_R^- \, \rho_R \tag{75}$$

and a pressure flux

$$p_{\frac{1}{2}} = p_L^+ + p_R^- \tag{76}$$

and a normal-momentum flux $(\rho u^2)_{\frac{1}{2}}$ as a blend of AUSMV and AUSMD fluxes

$$\begin{aligned} (\rho u^2)_{AUSMV} &= u_L^+ \, \rho_L \, u_{nL} + u_R^- \, \rho_R \, u_{nR} \ , \\ (\rho u^2)_{AUSMD} &= \frac{1}{2}\Big((\rho u)_{\frac{1}{2}}(u_{nL} + u_{nR}) - |(\rho u)_{\frac{1}{2}}|(u_{nR} - u_{nL})\Big) \ , \\ (\rho u^2)_{\frac{1}{2}} &= (\frac{1}{2} + s)(\rho u^2)_{AUSMV} + (\frac{1}{2} - s)(\rho u^2)_{AUSMD} \ , \end{aligned} \tag{77}$$

with the switching function, s, based on the pressure gradient

$$s = \frac{1}{2} \min\left(1, K \frac{|p_R - p_L|}{\min(p_L, p_R)}\right) \ , \tag{78}$$

with $K = 10$.

The flux vector components can be assembled from these pieces as

$$\begin{aligned} F_{mass} &= (\rho u)_{\frac{1}{2}} \ , \\ F_{n-momentum} &= (\rho u^2)_{\frac{1}{2}} + p_{\frac{1}{2}} \ , \end{aligned} \tag{79}$$

and depending on which way the wind is blowing, the remaining flux vector components are assembled from either the right or left flow properties. For $(\rho u)_{\frac{1}{2}} \geq 0$,

$$\begin{aligned} F_{p-momentum} &= (\rho u)_{\frac{1}{2}} \, u_{pL} \ , \\ F_{energy} &= (\rho u)_{\frac{1}{2}} \, H_L \ . \end{aligned} \tag{80}$$

$$\tag{81}$$

otherwise

$$\begin{aligned} F_{p-momentum} &= (\rho u)_{\frac{1}{2}} \, u_{pR} \ , \\ F_{energy} &= (\rho u)_{\frac{1}{2}} \, H_R \ . \end{aligned} \tag{82}$$

$$\tag{83}$$

where $H = e + \frac{p}{\rho} + \frac{1}{2}\left(u_n^2 + u_p^2\right)$ is the total enthalpy of the gas. Again, species mass fractions are just transported by the mass flux as scalar quantities.

Finally, an entropy fix is applied, as per Section 3.5 in Reference [32]. This first determines if the interface includes an expansion sonic point

Case A: $u_{nL} - a_L < 0$ and $u_{nR} - a_R > 0$
Case B: $u_{nL} + a_L < 0$ and $u_{nR} + a_R > 0$

and increments the flux if only a single expansion wave is detected

$$\begin{aligned} F_{mass} &-= \Delta_{ua}\left(\rho_R - \rho_L\right) , \\ F_{n-momentum} &-= \Delta_{ua}\left(\rho_R u_{nR} - \rho_L u_{nL}\right) , \\ F_{p-momentum} &-= \Delta_{ua}\left(\rho_R u_{pR} - \rho_L u_{pL}\right) , \\ F_{energy} &-= \Delta_{ua}\left(\rho_R H_R - \rho_L H_L\right) , \end{aligned} \tag{84}$$

where

$$\begin{aligned} \Delta_{ua} &= 0.125((u_{nR} - a_R) - (u_{nL} - a_L)) \text{ , for A and not B,} \\ &= 0.125((u_{nR} + a_R) - (u_{nL} + a_L)) \text{ , for B and not A,} \\ &= 0 \text{ , otherwise.} \end{aligned} \tag{85}$$

Shock Detector The switching between the two flux calculators is governed by a shock (or compression) detector. This is simply a measure of the relative change in normal velocity at interfaces. Specifically, we indicate a strong compression at cell-interface $i + \frac{1}{2}$ when

$$\frac{u_{n,i+1} - u_{n,i}}{\min(a_{i+1}, a_i)} < \text{Tol} \ , \tag{86}$$

where Tol is the compression tolerance and is typically set at -0.05. This measure is applied to all interfaces in a block and then a second pass propagates the information to near-by interfaces. If a first cell-interface is identified as having a strong compression, the EFM flux calculator is used for all interfaces attached to the cell containing that first cell-interface.

3.2.5 Viscous Fluxes

The viscous flux calculation is then performed based on the the updated cell-centre flow state. The spatial derivates required in the viscous stress and heat flux terms, Eq. 47 and 48, are obtained by applying the divergence theorem to each of the secondary cells surrounding a primary-cell vertex (as shown in Figure 13, and then averaging the vertex derivatives to obtain a cell centre value. Secondary cells of half size are used along the boundaries and viscous boundary conditions for velocity (*e.g.* no slip) and temperature are applied at those boundary interfaces.

3.3 Thermochemistry

In both simulation codes, `L1d2`and `mbcns2`, the governing equations are closed by a set of relations between the various thermodynamic properties of the gas mixture. This section describes a gas library which provides various models of gas behaviour for use in the simulation codes.

There are a number of gas models available as part of the gas library. They are desribed here:

ideal gas mix

The ideal gas mix is used to model one or more components, all of which have ideal (perfectly elastic collisions and calorically perfect) behaviour.

equilibrium gas mix

The equilibrium gas mix models a fixed-composition gas mix which is assumed to be in thermal and chemical equilibrium at the local thermodynamic conditions.

thermally perfect gas mix

The thermally perfect gas mix models a gas with one or more components, all of which have perfect (collisional) behaviour but each have all internal energy modes excited to an equilibrium described by a single temperature

multi-temperature gas mix

This model represents a mixture of gases with perfect collisional behaviour but the the internal energy modes are ascribed different Boltzmann temperatures in order to model the effect of thermal nonequilibrium.

Noble-Abel gas mix

The Nobel-Abel gas mix model is used in interior ballistics work where high pressures mean that real gas effects cannot be neglected. It models the effect of the finite volume occupied by gas particles when computing the equation of state. Collisions between gas particles are still considered to be perfectly elastic.

van der Waals gas mix

The van der Waals gas mix models real gas effects at high pressures/densities. The finite volume occupied by the gas particles and the non-ideal particle collisions due to van der Waals' forces are considered in the model.

In simulating impulse facilities, we typically only use the equilibrium gas and thermally perfect gas models. Therefore, these two models are discussed in the remainder of this section. The thermally perfect gas mix is used when we also wish to simulate the effect of finite-rate chemistry between the gases. The multi-temperature gas mix has also been used recently to model the X2 facilities [35], however, we consider the validation of this model a work in progress.

3.3.1 An equilibrium gas mixture

At higher temperatures, the gases in impulse facilities will undergo chemical reactions. For example in air, by 2 000 K oxygen molecules will begin to dissociate, and by 4 000 K nitrogen molecules will begin to dissociate. When the chemical reactions are rapid compared to the flow transit times, we use a model of the gas which assumes chemical equilibrium. Along with the assumption of chemical equilibrium, thermal equilibrium is also assumed; the internal energy modes of the gas rapidly equilibriate with the translational temperature when compared to the characteristic flow time. This assumption is most appropriate in the high pressure, high temperature gas that is driven by the piston against an unruptured diaphgram: the high pressures and temperatures give rise to rapid changes in chemical composition.

The equilibrium gas mix is implemented as a look-up table where the thermodynamic properties are interpolated (or extrapolated) from a table with indexing based on density and internal energy. The look-up table is built for a fixed gas composition over a range of densities and energies prior to the gas dynamics simulation and is read into memory at the start of the simulation. A tool provided in the gas library builds the look-up table by running the CEA2 program [36] numerous times.

3.3.2 A mixture of thermally perfect gases

As mentioned above, the gas model for a mixture of thermally perfect gases is often used in conjunction with a finite-rate chemistry simulation. The thermodynamic relations for the gas mixture are presented here. The implementation of finite-rate chemical effects is discussed in Section 3.3.3.

A single thermally perfect gas The assumed behaviour of a thermally perfect gas is that all internal energy modes are in equilibrium at a single temperature. For atoms this means that the Boltzmann distributions for translational and electronic energy are governed by one temperature value. Similarly for molecules, the Boltzmann distributions for translational, rotational, vibrational and electronic energy are described by a single temperature value.

To model a thermally perfect gas requires a knowledge of how the gas stores energy as a function of temperature. It is convenient to have available the specific heat at constant pressure as a function of temperature, $C_p(T)$. From this, specific enthalpy of the gas can be computed as

$$h = \int_{T_{ref}}^{T} C_p(T)dT + h(T_{ref}) \tag{87}$$

and entropy is given as

$$s = \int_{T_{ref}}^{T} \frac{C_P(T)}{T}dT + s(T_{ref}). \tag{88}$$

The transport properties, viscosity and thermal conductivity, can be calculated as a function of temperature for a single component of the gas mix. The transport properties for a single component can be combined by an appropriate mixing rule to give a mixture viscosity and thermal conductivity.

In the implementation, a thermally perfect gas is characterised by five curve fits all of which are functions of temperature:

1. specific heat at constant pressure, $C_p(T)$,
2. enthalpy, $h(T)$,
3. entropy, $s(T)$,
4. viscosity, $\mu(T)$, and
5. thermal conductivity, $k(T)$.

The form of these curve fits follows that used by McBride and Gordon [36]. The curve fits for thermodynamic properties in non-dimensional form are as follows:

$$\frac{C_p(T)}{R} = a_0T^{-2} + a_1T^{-1} + a_2 + a_3T + a_4T^2 + a_5T^3 + a_6T^4 \tag{89}$$

$$\frac{H(T)}{RT} = -a_0T^{-2} + a_1T^{-1}\log T + a_2 + a_3\frac{T}{2} + a_4\frac{T^2}{3} + a_5\frac{T^3}{4} + a_6\frac{T^4}{5} + \frac{a_7}{T} \tag{90}$$

$$\frac{S(T)}{R} = -a_0\frac{T^{-2}}{2} - a_1T^{-1} + a_2\log T + a_3T + a_4\frac{T^2}{2} + a_5\frac{T^3}{3} + a_6\frac{T^4}{4} + a_8 \tag{91}$$

The coefficients for these curve fits are available for a large number of gaseous species in the CEA program [36] (and associated database files). Each of these curve fits are only valid over a limited temperature range. For example, the thermodynamic curve fits for molecular nitrogen (N_2) are comprised of three segments: 200.0–1000.0 K, 1000.0–6000.0 K and 6000.0–20000.0 K. Beyond this range the values are extrapolated in this work. The extrapolations are based on a crude assumption of constant C_p outside of the range.

Thus the extrapolations are as follows:

$$\begin{aligned}
\frac{C_p(T < T_{low})}{R} &= \frac{C_p(T_{low})}{R} \\
\frac{C_p(T > T_{high})}{R} &= \frac{C_p(T_{high})}{R} \\
\frac{H(T < T_{low})}{RT} &= \frac{1}{T}\left\{H(T_{low})T_{low} - C_p(T_{low})(T_{low} - T)\right\} \\
\frac{H(T > T_{high})}{RT} &= \frac{1}{T}\left\{H(T_{high})T_{high} + C_p(T_{high})(T - T_{high})\right\} \\
\frac{S(T < T_{low})}{R} &= S(T_{low}) - C_p(T_{low}) \log\left(\frac{T_{low}}{T}\right) \\
\frac{S(T > T_{high})}{R} &= S(T_{high}) + C_p(T_{high}) \log\left(\frac{T}{T_{high}}\right)
\end{aligned}$$

The curve fits for viscosity and thermal conductivity are also in the same form as that used by the CEA program [36]. The curves are as follows.

$$\log \mu(T) = a_0 \log T + \frac{a_1}{T} + \frac{a_2}{T^2} + a_3$$

$$\log k(T) = b_0 \log T + \frac{b_1}{T} + \frac{b_2}{T^2} + b_3$$

Mixing rules for a collection of thermally perfect gases The thermodynamic state for a mixture of thermally perfect gases is uniquely defined by two state variables and the mixture composition. The internal energy is computed as a mass fraction weighted sum of individual internal energies,

$$e = \sum_{i=1}^{N} f_i e_i = \sum_{i=1}^{N} f_i \left(h_i - R_i T\right). \tag{92}$$

Pressure is computed from Dalton's law of partial pressures,

$$p = \sum_{i=1}^{N} \rho_i R_i T. \tag{93}$$

The specific gas constant for the mixture is defined as

$$R = \sum_{i=1}^{N} f_i R_i. \tag{94}$$

The calculation of C_p is based on a mass fraction weighted sum of component specific heats,

$$C_p = \sum_{i=1}^{N} f_i C_{p_i}. \tag{95}$$

The specific heat at constant volume is then computed as

$$C_v = C_p - R. \tag{96}$$

The ratio of specific heats, γ, is given by its definition,

$$\gamma = \frac{C_p}{C_v}. \tag{97}$$

The frozen sound speed for the mixture, a, is calculated as

$$a = \sqrt{\gamma RT}. \tag{98}$$

During a compressible flow simulation, the values of ρ and e are most readily available from the conserved quantities that are solved for during each time increment. This leads to the specific problem of solving for the thermodynamic state of the gas mixture given ρ, e, and the mixture composition, $\overrightarrow{f}$. However, the formulae previously presented are all explicit in temperature. We solve for temperature using the Newton iteration technique for zero solving,

$$T_{n+1} = T_n - \frac{f_0(T_n)}{f_0'(T_n)}, \tag{99}$$

where the zero function, $f_0(T)$, is based on the given internal energy, e, and a guess for internal energy based on temperature,

$$f_0(T) = e_{guess} - e = \sum_{i=1}^{N} f_i \left(h_i - R_i T_{guess}\right) - e. \tag{100}$$

Using the fact that $C_{vi} = \frac{de_i}{dt}$, we can conveniently find the derivative function for the Newton technique by computing the mixture C_v,

$$\frac{df_0(T)}{dT} = \sum_{i=1}^{N} f_i \frac{de_i}{dT} = \sum_{i=1}^{N} f_i C_{vi} = C_v. \tag{101}$$

The Newton iteration is set to converge when the accuracy of the temperature value is within $\pm 1.0 \times 10^{-6}$ K. Personal experience has shown that this kind of error tolerance is required when temperature is used in a finite-rate chemistry calculation to compute rates of composition change.

The calculation of mixture transport properties is not as straight forward as the thermodynamic properties. A mixing rule is required to compute the mixture viscosity and thermal conductivity. Wilke's mixing rule [20] has been implemented in the work presented here. Specifically, the mixing rules used by Gordon and McBride [37] in the CEA program are used for calculating mixture transport properties in this work; these rules are a variant of Wilke's original formulation [20].

$$\mu_{mix} = \sum_{i=1}^{N} \frac{x_i \mu_i}{x_i + \sum_{\substack{j=1 \\ j \neq i}}^{N} x_j \phi_{ij}} \tag{102}$$

and

$$k_{mix} = \sum_{i=1}^{N} \frac{x_i k_i}{x_i + \sum_{\substack{j=1 \\ j \neq i}}^{N} x_j \psi_{ij}} \tag{103}$$

where x_i is the mole fraction of species i.

The interaction potentials, ϕ_{ij} and ψ_{ij}, can be calculated a number of ways. Again, the formulae suggested by Gordon and McBride [37] have been used,

$$\phi_{ij} = \frac{1}{4}\left[1 + \left(\frac{\mu_i}{\mu_j}\right)^{1/2}\left(\frac{M_j}{M_i}\right)^{1/4}\right]^2 \left(\frac{2M_j}{M_i + M_j}\right)^{1/2} \tag{104}$$

and

$$\psi_{ij} = \phi_{ij}\left[1 + \frac{2.41(M_i - M_j)(M_i - 0.142M_j)}{(M_i + M_j)^2}\right] \tag{105}$$

where M_i and M_j refer to the molecular weights of species i and j respectively.

Once the mixture viscosity and thermal conductivity have been computed, it is possible to compute the mixture Prandtl number from its definition

$$Pr = \frac{\mu C_p}{k}. \tag{106}$$

3.3.3 Finite-rate chemistry implementation

Rates of species change due to chemical reaction By assuming a collection of simple reversible reactions, the chemically reacting system can be represented as,

$$\sum_{i=1}^{N} \alpha_i X_i \rightleftharpoons \sum_{i=1}^{N} \beta_i X_i, \tag{107}$$

where α_i and β_i represent the stoichiometric coefficients for the reactants and products respectively. The case of an irreversible reaction is represented by setting the backward rate to zero. For a given reaction j, the rate of concentration change of species i is given as,

$$\left(\frac{d[X_i]}{dt}\right)_j = \nu_i \left\{ k_f \prod_i [X_i]^{\alpha_i} - k_b \prod_i [X_i]^{\beta_i} \right\}, \tag{108}$$

where $\nu_i = \beta_i - \alpha_i$. By summation over all reactions, N_r, the total rate of concentration change is,

$$\frac{d[X_i]}{dt} = \sum_{j=1}^{N_r} \left(\frac{d[X_i]}{dt}\right)_j. \tag{109}$$

For certain integration schemes it is convenient to have the production and loss rates available as separate quantities. In this case,

$$\frac{d[X_i]}{dt} = q_i - L_i = \sum_{j=1}^{N_r} \dot{\omega}_{app_{i,j}} - \sum_{j=1}^{N_r} \dot{\omega}_{va_{i,j}} \tag{110}$$

The calculation of $\dot{\omega}_{app_{i,j}}$ and $\dot{\omega}_{va_{i,j}}$ depends on the value of ν_i in reach reaction j as shown in Table 1.

Table 1: The form of the chemical production and loss terms based on the value of ν_i

	$\nu_i > 0$	$\nu_i < 0$
$\dot{\omega}_{app_i}$	$\nu_i k_f \prod_i [X_i]^{\alpha_i}$	$-\nu_i k_b \prod_i [X_i]^{\beta_i}$
$\dot{\omega}_{va_i}$	$-\nu_i k_b \prod_i [X_i]^{\beta_i}$	$\nu_i k_f \prod_i [X_i]^{\alpha_i}$

The calculation of the reaction rate coefficients, k_f and k_b, and the solution methods for the ordinary differential equation system of species concentration changes are discussed in the subsequent sections.

Reaction rate coefficients The reaction rate coefficients for a reaction can be determined by experiment (often shock tube studies are used) or from theory. In a great number of cases, estimates of the reaction rate from theory can vary by orders of magnitude from experimentally determined values. For this reason, fits to experimental values are most commonly used.

For the single-temperature gas model discussed in this chapter, the forward reaction rate coefficients are calculated using the generalised Arrhenius form,

$$k_f = AT^n \exp\left(\frac{-E_a}{kT}\right) \tag{111}$$

where k is the Boltzmann constant and A, n and E_a are constants of the model.

The backward rate coefficient can also be calculated using a modified Arrhenius form,

$$k_b = AT^n \exp\left(\frac{-E_a}{kT}\right) \tag{112}$$

or it can be calculated by first calculating the equilibrium constant for the reaction,

$$k_b = \frac{k_f}{K_c}. \tag{113}$$

If the backward rate coefficient is calculated from the equilibrium constant, then a method of calculation of the equilibrium constant is required. The equilibrium constant for a specific reaction can be calculated from curve fits or, as is done in this work, using the principles of thermodynamics. The equilibrium constant based on concentration is related to the equilibrium constant based on pressure by,

$$K_c = K_p \left(\frac{p_{atm}}{\mathcal{R}T}\right)^{\nu} \tag{114}$$

where p_{atm} is atmospheric pressure in Pascals, $\mathcal{R}$ is the universal gas constant, $\nu = \sum_i^{N_S} \nu_i$ and

$$K_p = \exp\left(\frac{-\Delta G}{\mathcal{R}T}\right). \tag{115}$$

The derivation of the formula for K_p, the equilibrium constant based on partial pressures, can be found in any introductory text on classical thermodynamics which covers chemical equilibrium. The differential Gibbs function for the reaction, ΔG, is calculated using

$$\Delta G = \sum_i^{N_s} \nu_i G_i \tag{116}$$

where each G_i is computed from the definition of Gibbs free energy,

$$G_i(T) = H_i(T) - T \times S_i(T) \tag{117}$$

and G_i is in units of J/mol. H_i and S_i can be computed in the appropriate units by using the CEA polynomials and multiplying by $\mathcal{R}T$ and $\mathcal{R}$ respectively.

Some caution should be exercised in the selection and use of reaction rates for a specific flow problem. In many cases, a set of reaction rates may only be "tuned" for a specific problem domain. This problem of "tuned" sets of reaction rates and an explanation for why it arises is described by Oran and Boris (p. 38 of Ref. [38]):

A problem that often arises in chemical reactions is that there are fundamental inconsistencies in a measured reaction rate. For example, there may be experimental measurements of both the forward and reverse rate constants, k_f and k_r. Nonetheless, when either is combined with the equilibrium coefficient for that reaction, the other is not produced. This appears to represent a violation of equilibrium thermodynamics. The explanation is usually that k_f and k_r have been measured at rather different temperatures or pressures, and so there are inconsistencies when they are extrapolated outside the regime of validity of the experiments.

Solving the chemical kinetic ordinary differential equation The system represented in Equation 109 is a system of ordinary differential equations (ODEs) which can be solved by an appropriate method. For certain chemical systems, the governing ODEs form a stiff system due to rates of change varying by orders of magnitude for certain species. For these systems, special methods for stiff ODEs are required. In this work, four methods for the numerical solution of the ODE system have been implemented.

1. Euler method
2. modified Euler method
3. alpha-QSS method, and
4. Runge-Kutta-Fehlberg method

The Euler method and modified Euler method are standard techniques for solving ODEs and the details can be found in any text dealing with numerical methods and numerical analysis. The fourth-order Runge-Kutta method uses a fifth-order error estimate as a means for controlling the timestep used for integration as proposed by Fehlberg [39]. This is particularly efficient for non-stiff systems.

alpha-QSS method The alpha-QSS (quasi-steady-state) method was proposed in Mott's thesis [40]. It is an ODE solver aimed specifically at the problem of stiffness in chemical systems. This ODE solver makes use of the forward and backwards rates of concentration change as calculated by Equation 110. This is a predictor-corrector type scheme in which the corrector is iterated upon until a desired convergence is achieved. The predictor and corrector are,

$$[X_i]^1 = [X_i]^0 + \frac{\Delta t q_i^0}{1 + \alpha_i^0 \Delta t L_i^0} \tag{118}$$

$$[X_i]^{n+1} = [X_i]^0 + \frac{\Delta t \left(\bar{q}_i - [X_i]^0 \bar{L}_i \right)}{1 + \bar{\alpha}_i \Delta t \bar{L}_i}. \tag{119}$$

In the above equations,

$$\bar{L}_i = \frac{1}{2} \left(L_i^0 + L_i^n \right) \tag{120}$$

and

$$\bar{q}_i = \bar{\alpha}_i q_i^n + \left(1 - \bar{\alpha}_i \right) Q_i^0. \tag{121}$$

The key to the scheme is calculating α correctly. This α parameter controls how the update works on a given species integration. Note that α is defined as

$$\alpha(L\Delta t) \equiv \frac{1 - \left(1 - e^{-L\Delta t} \right) / (L\Delta t)}{1 - e^{-L\Delta t}}. \tag{122}$$

Using Pade's approximation,

$$e^x \approx \frac{360 + 120x + 12x^2}{360 - 240x + 72x^2 - 12x^3 + x^4} \tag{123}$$

it is possible to write a form of the expression for α which is more amenable to computation as the expensive exponential function evaluation is avoided. The approximation for α becomes,

$$\alpha(L\Delta t) \approx \frac{180r^3 + 60r^2 + 11r + 1}{360r^3 + 60r^2 + 12r + 1} \tag{124}$$

where $r \equiv 1/(L\Delta t)$.

Coupling chemistry effects to the flow solver Some details about the coupling of the chemistry effects to the gas dynamics simulation are provided here. In an unsteady, time-accurate flow simulation, the allowable timestep is constrained by the Courant-Friedrichs-Lewy (CFL) criterion. In a viscous compressible flow, the CFL criterion allows one to select an appropriate timestep and limit the propagation of flow information to distances less than one cell-width. The speed at which flow information propagates is a function of inviscid wave speeds and viscous effects.

When the effects of finite-rate chemistry are 'split' from the flow simulation, the chemical update is solved in a separate step in which the flow is held frozen. (In fact, in true timestep-splitting, *all* other contributing physics is frozen during the chemistry update.) Thus the chemistry problem is to find the updated species composition at the end of the flow timestep.

It may be, and is quite likely, that the flow timestep is not an appropriate timestep to solve the chemical kinetic ODE problem. When the timestep for the chemistry problem is smaller than the flow timestep, the chemistry problem is subcycled a number of times until the total elapsed time equals that of the flow timestep. It is common to have simulations where the chemistry timestep is 100–1000 times smaller than the flow timestep, that is, 100-1000 subcycles are required to solve the chemistry problem. When the timstep for the chemistry problem is larger than the flow timestep, it is simply set to the value of the flow timestep.

During the simulation process, the chemistry timestep is tracked for each finite-volume cell in the simulation. Although the flow 'moves on' in subsequent timesteps, if the change of flow conditions is not large, then the previous chemistry timestep will be a good estimate to begin the new chemistry problem in the subsequent timestep. An exceptional case is when a shock passes through the cell: the change of flow conditions does become large. In this instance, the old chemistry step is disregarded and a new step is selected. The selection procedure for a new step is discussed in the next paragraph. When using either the Runge-Kutta-Fehlberg or the alpha-QSS methods, an estimate of the new chemistry timestep is provided as part of the ODE update routine.

So, during a simulation, the old chemistry step at one iteration is used to begin the new chemistry problem in the next iteration. What is needed is a means to select the chemistry step on the initial iteration, or whenever the old suggestion is not reasonable (as in the case of a shock passing through the cell). In this work, the initial step for the chemistry problem is selected based on the suggestion by Young and Boris [41],

$$dt_{\text{chem}} = \epsilon_1 \min\left(\frac{[X_i](0)}{[\dot{X}_i](0)}\right) \tag{125}$$

where ϵ_1 is taken as 1.0×10^{-3} in this work, and the expression is evaulated at the initial values for the chemistry subproblem. Young and Boris [41] suggest that ϵ_1 be scaled from the convergence criteria. We have found that the fixed value is adequate for the problems of interest to our research group.

4 APPLICATIONS

In Section 4.1, the applications start with the simplest model of the smaller machine, the Drummond tunnel. The `L1d2` simulation gives quick results for bulk gas conditions in the shock tube but doesn't include the details of the reflected-shock interaction with the shock-tube boundary-layer. To capture these details, and the expansion process through a high Mach number nozzle, axisymmetric flow simulations are used (Section 4.2). Even though the Drummond tunnels is a relatively low enthalpy machine, the axisymmetric simulations of the full facility are computationally demanding.

For the modelling of the X2 expansion tube, we again start with the `L1d2` modelling of the whole facility to look at developing operating conditions with a new, light weight piston (Section 4.3). Since this mode of analysis in exploratory, we need to do many simulations and concentrate on the large-scale facility behaviours of piston motion and shock speed. Once the operational conditions are defined, we need to increase the level of detail of the simulation model in order to get complete estimates of the test-section flow conditions. The interaction of the final expansion and chemistry, together with substantial boundary layers growing in the acceleration tube, demands a high resolution numerical simulation. The computational cost for doing this high-resolution axisymmetric simulation for the entire X2 machine is very high so we make use of both simulation codes. The `L1d2` code is used to model the whole facility and transient flow data, just upstream of the secondary diaphragm, is fed to axisymmetric simulation of the unsteady expansion process through the acceleration tube and into the dump tank. An example of this hybrid simulation approach is discussed in Section 4.4.

4.1 One-Dimensional Modelling of the Drummond Tunnel

Using a nitrogen driver gas with nitrogen test gas gives a limited but simple-to-model operating conditon for the Drummond tunnel. The `L1d2` input listing, shown below, defines the simulation by specifying:

- the gas model,
- the internal surface description of the tunnel as a set of break-points in diameter, and
- the gas slugs, which are contained by the tube end walls, a contact surface (where the main diaphragm would have been) and a diaphragm at the nozzle throat.

The sudden contractions or expansions in tube diameter at the diaphragm and nozzle throat are also marked as regions of head loss. Figure 14 shows the representation of the internal surfaces of the machine. Note that all area transitions occur over finite axial distances. This is a limitation of the quasi-one-dimensional model implemented by `L1d2`, but also happens to be close to reality for the Drummond tunnel. Instrumentation locations in the actual machine are identified as "history locations" in the listing and data are written out for those locations at a high frequency (every 2 μs). Data for the entire flow path is written out every 30 μs.

```
# ~/cfcfd2/app/L1d/examples/Drummond/dn2.py
gdata.title = \
   "Drummond tunnel M4 nozzle P4 = 3.25MPa N2, P1 = 30kPa N2, 06-Jul-05"
gdata.case_id = 27
gdata.gas_name = "LUT"

# Define the tube walls.
gdata.n = 4000
add_break_point(-3.785,  0.0585)    # upstream-end of the driver tube
add_break_point(-3.035,  0.0585)
add_break_point(-3.015,  0.0620)    # steel-diaphragm station
# Note that there is no steel diaphragm in this simulation.
add_break_point( 0.000,  0.0620)    # downstrem end of shock tube
add_break_point( 0.043,  0.0620)    # start of contraction to throat
```

```
add_break_point( 0.080,  0.0220)    # start of throat
add_break_point( 0.100,  0.0220, 1) # start of nozzle (conical shape)
add_break_point( 0.2653, 0.0700, 1) # start of parallel test section
add_break_point( 0.30,   0.0700)
#
add_loss_region(-3.050, -3.000, 0.5) # at steel-diaphragm station
add_loss_region( 0.050,  0.120, 0.5) # at nozzle throat
#
gdata.T_nominal = 296.0

# Create the gas-path.
left_end = VelocityEnd(x0=-3.785, v=0.0)
driver_gas = GasSlug(p=3.25e6, u=0.0, T=296.0, nn=150,
                     viscous_effects=1, hcells=1, label="driver gas")
cs = GasInterface(x0=-3.015)
test_gas = GasSlug(p=30.0e3, u=0.0, T=296.0, nn=300,
                   viscous_effects=1, hcells=1, label="test gas")
diaph = Diaphragm(x0=0.10, p_burst=150.0e3)
dump_tank_gas = GasSlug(p=4.0e3, u=0.0, T=296.0, nn=6, to_end_L=1, cluster_strength=1.1,
                        viscous_effects=1, hcells=1, label="dump-tank gas")
right_end = FreeEnd(x0=0.3)
assemble_gas_path(left_end, driver_gas, cs, test_gas, diaph, dump_tank_gas, right_end)

# Set some time-stepping parameters
gdata.dt_init = 0.5e-6
gdata.cfl = 0.25
gdata.max_time = 8.0e-3
gdata.max_step = 100000
add_dt_plot(0.0, 30.0e-6, 2.0e-6)
add_history_loc(-0.295) # 0, heat flux gauge
add_history_loc(-0.078) # 1, pressure transducer
add_history_loc( 0.000) # 2, joint at nozzle block
add_history_loc( 0.090) # 3, mid-point of nozzle throat
add_history_loc( 0.265) # 4, nozzle exit plane
```

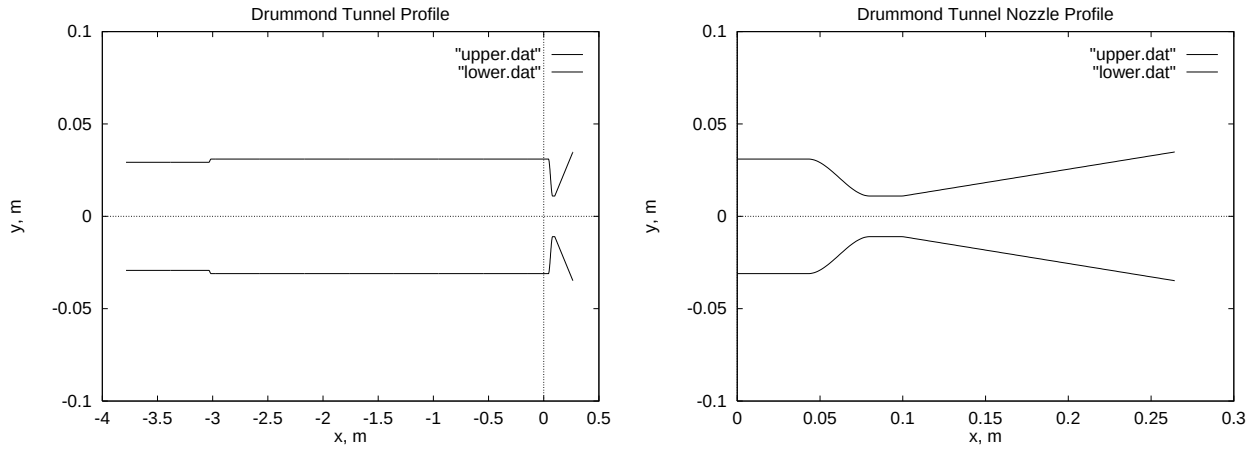

Figure 14: Drummond tunnel cross-section as modelled in `L1d2`.

From the data recorded throughout the simulation, the pressure values have been contoured on a logarithmic scale to form the space-time diagram shown in Figure 15. This clearly shows the shock and expansion wave motion within the machine, including the shock reflection at $t = 4$ ms and over-tailored interaction of the reflected shock with the test-gas driver-gas interface at $t = 5$ ms, both occuring at the downstream-end of the shock tube.

Comparison with experimental data is shown in Figure 16. There is good agreement, however, the simulation shows a number of sudden jumps in pressure, whilst the experimental traces show more gradual

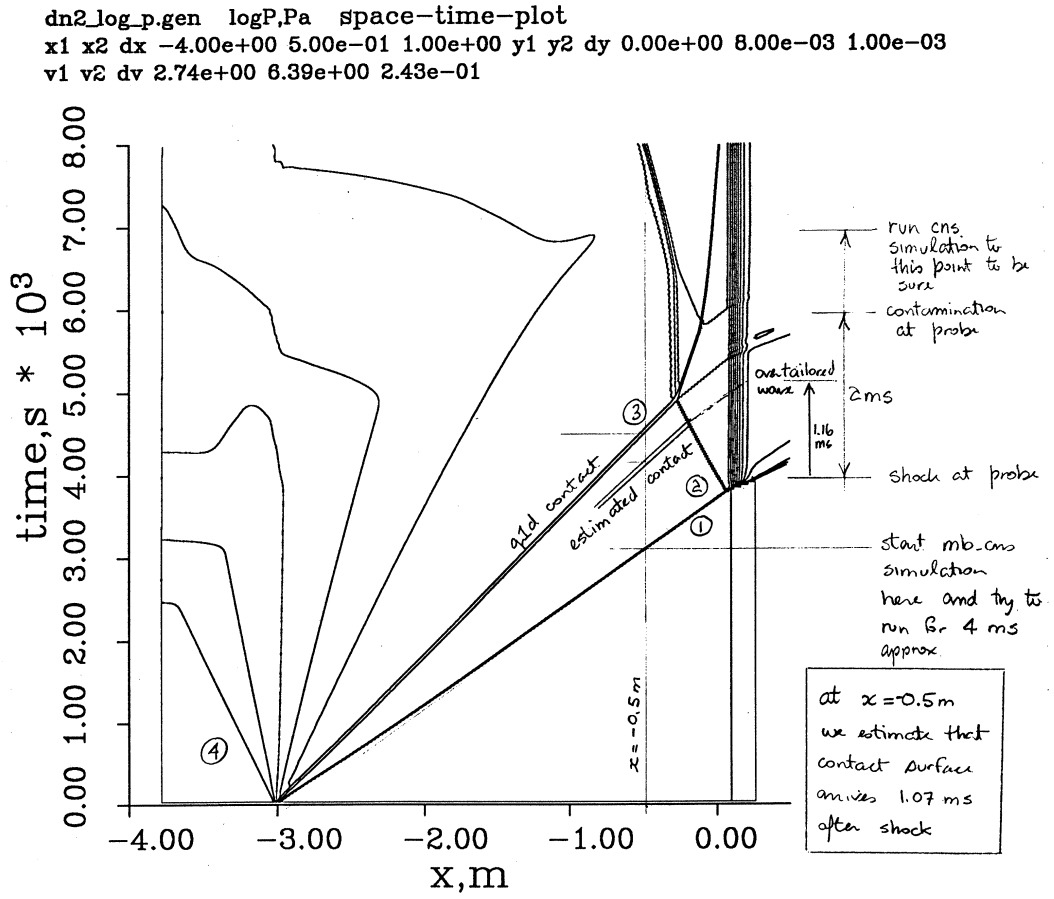

Figure 15: Computed wave diagram for Drummond tunnel operated with nitrogen driving nitrogen, over-tailored operation. This figure is scanned from PJ's workbook and the annotation relates to the set up of the axisymmetric simulation discussed in the following section.

changes at later times. This is a limitation of the quasi-one-dimensional nature of the simulation and the following section will show the far more interesting multidimensional wave interactions that occur after shock reflection.

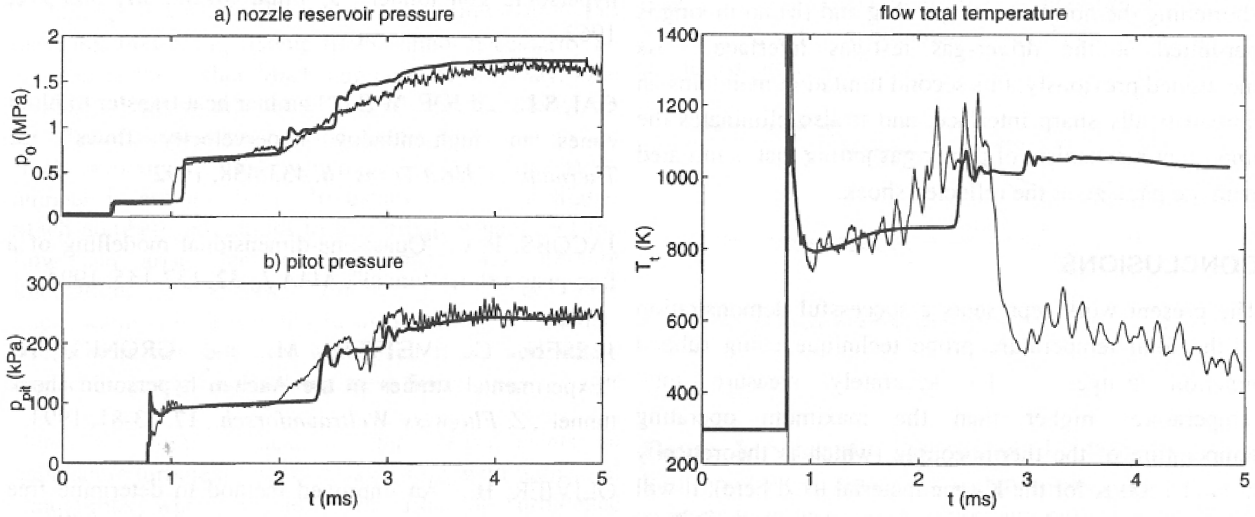

Figure 16: Nozzle-supply pressure, Pitot pressure and total temperature for Drummond tunnel, nitrogen driving nitrogen, over-tailored operation.

Comparison with experimental data was also made in Reference [42]. In this case, the pressure of the helium driver gas at diaphragm rupture was 3.25 MPa and the filling pressure of the nitrogen in the shock tube was set at 16.5 kPa to achieve tailored operation. Nozzle-supply pressure and Pitot pressure histories are shown in Figure 17. The shock speed, as estimated by `L1d2`, was 1.49 km/s and the nozzle supply conditions were $p_s = 2.14$ MPa and $T_s = 1920$ K. The actual (measured) nozzle-supply pressure was consistently around 2.0 MPa for a number of shots. These conditions are very similar to those produced with an earlier mode of operation using a double-diaphragm to control the initial release of the driver gas.

The simulation has accurately captured the incident shock features, both shock speed and pressure jump. It has also accurately captured the long term decay of the nozzle-supply pressure due to the relatively short driver tube. Where the simulation deviates noticeably is on shock reflection where the gas dynamics is quite complex. Here, `L1d2`'s flow approximation using only normal waves is lacking in the detail that can be captured with an axisymmetric analysis using `mbcns2`.

4.2 Axisymmetric Simulation of the Drummond Tunnel

Starting Flow in the Mach 7 Nozzle The next level of detail is captured by using `mbcns2` to do an axisymmetric-flow simulation of the last 0.5 metre section of the shock tube and the attached supersonic nozzle. Figure 18 shows the evolution of the shock reflection and nozzle-starting process for the Mach 7 contoured nozzle (designed by Craddock [2]).

In this simulation, the gas in the shock tube is ideal nitrogen, initially at $p_1 = 30$ kPa and $T_1 = 296$ K. With an incident shock speed of 782 m/s from the `L1d2` simulation, the post-shock conditions applied at the inflow plane are $p_2 = 176$ kPa, $T_2 = 564$ K and $u_g = 535$ m/s. These conditions are applied to the core flow of the inlet and a boundary layer velocity profile is superimposed. The simulation starts with the incident shock at the inflow plane, and the boundary layer profile grows in time.

The first frame in Figure 18 occurs shortly after the reflection of the shock off the tube endwall and the frames continue until the flow through the nozzle has mostly settled, although small distrubances are

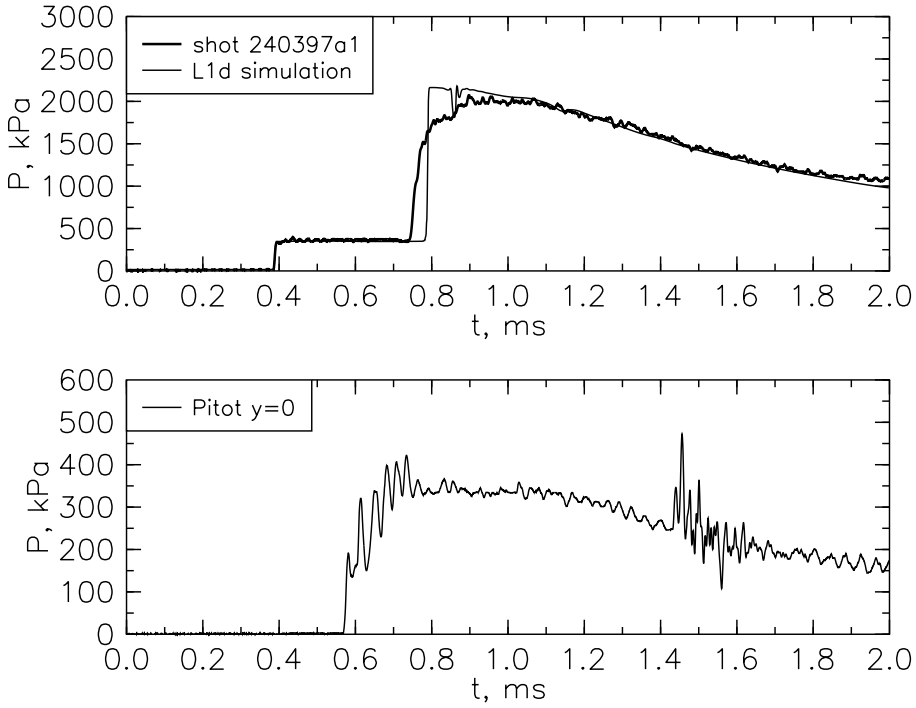

Figure 17: Wall-pressure history in the shock-reflection region and Pitot-pressure history at the nozzle exit plane for single-diaphragm operation (shot number 240397a3).

still working their way through the nozzle. There is much detail in the shock-reflection region but the main interest of this simulation is the complex starting process in the expanding part of the nozzle. The classic, nearly one-dimensional starting structure [43] seen in the first frame evolves into an extended structure with large separation zones supporting the oblique upstream-facing shocks. These shocks cause recompression that focuses towards the nozzle centreline. Because the separation line takes a relatively long time to be swept out of the nozzle, the disturbance near the centreline persists long after the one-dimensional theory indicates that the flow should have settled.

Reflected-Shock Interaction with the Boundary Layer The next step up in computational effort is an axisymmetric simulation of the whole machine. Figure 19 shows the evolution of the flow in the shock-reflection region for the over-tailored case of nitrogen driving nitrogen [3]. There is much of interest to be observed and there are precious few one-dimensional waves involved. The idea that the test gas is brought to rest by a reflected shock wave is seen to be far from the more detailed reality.

The main modelling complexity in this simulation is for the relatively slow opening process of the main diaphragm. Here the metal diaphragm is approximated as an opening iris, with the barrier between driver gas and test gas being removed from the computational domain over a number of time steps. The rest of the flow domain is bounded by solid walls, at 296 K, with no-slip boundary conditions.

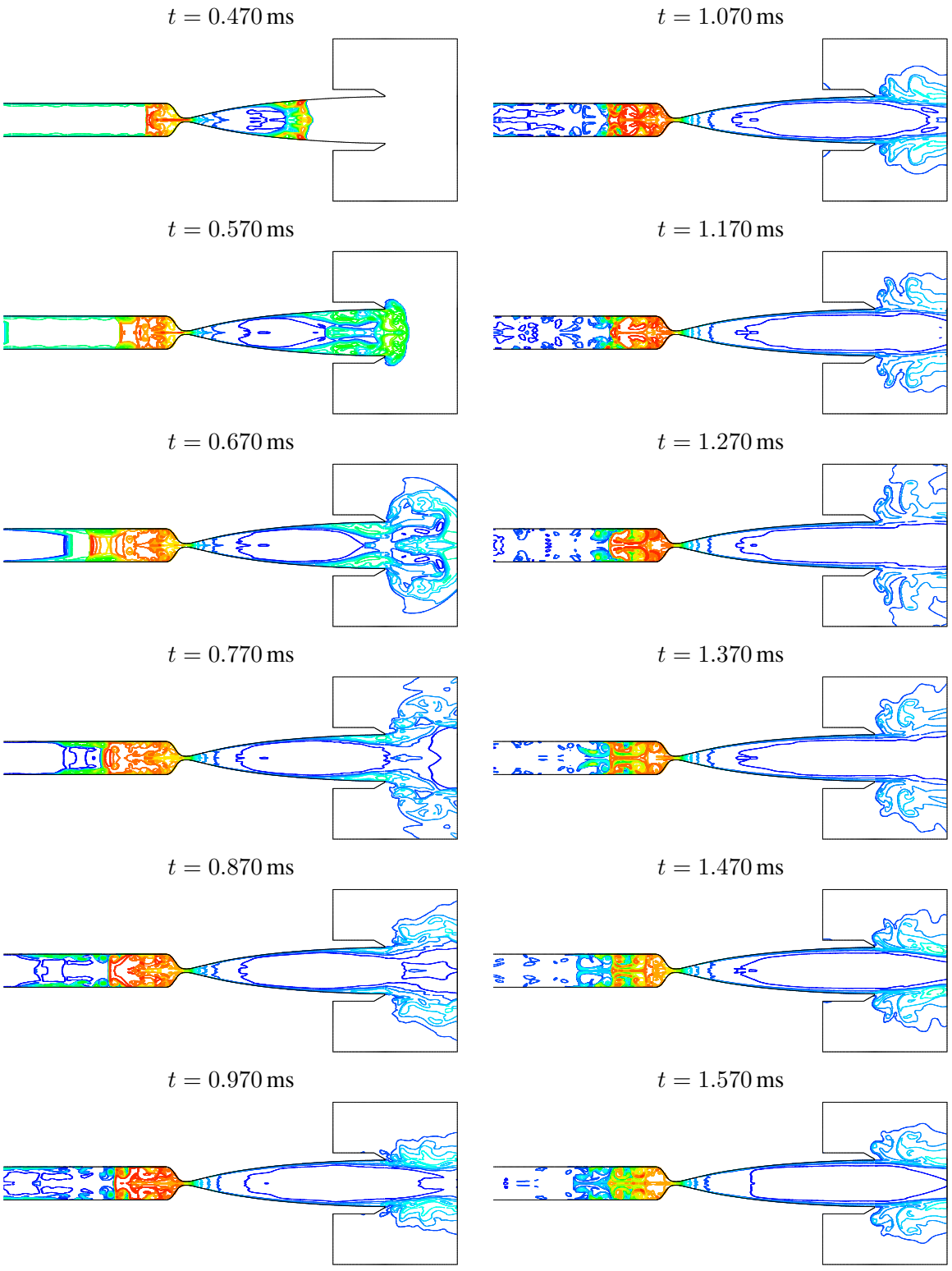

Figure 18: The development of flow in the Mach 7 nozzle of Drummond tunnel. The coloured contours indicate temperatures, with red indicating up to 2600 K and blue as low as 100 K.

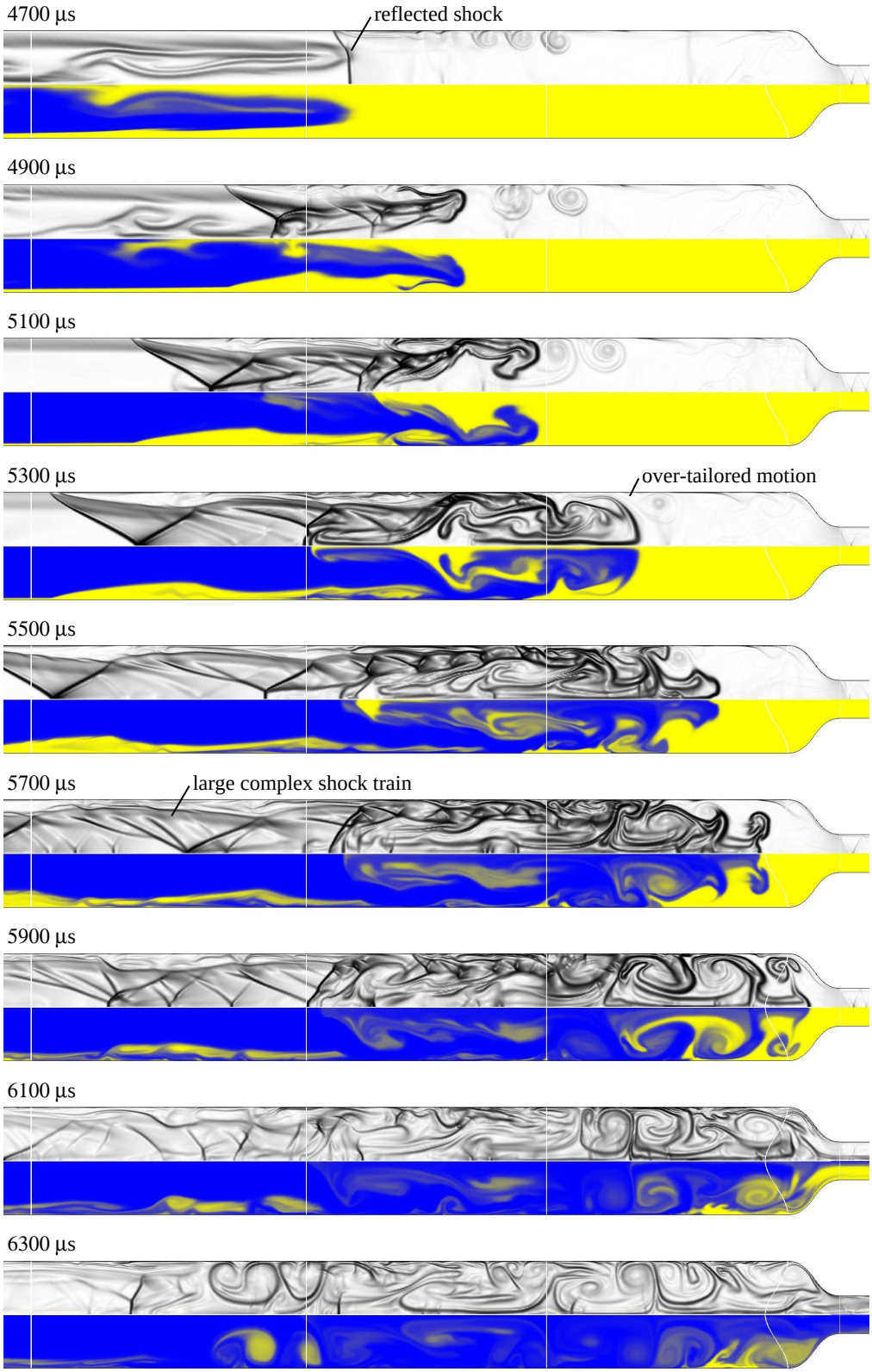

Figure 19: Sequence of numerical schlieren images (*top*) and driver gas mass fractions (*bottom*) showing the over-tailored interaction of the reflected shock with the boundary layer.

4.3 Commissioning a New Lightweight Piston for X2

4.3.1 The Free Piston Driver

The free piston driver is currently our preferred technique to achieve high performance drivers for our impulse facilities. Since this type of driver compressively heats the driver gas, it is capable of achieving both the high pressures and the high sound speeds required to generate strong shock waves. However, the free piston driver presents three main challenges:

1. Tuning its operation to prevent damage to the piston, to the buffer and to the compression tube.
2. Tuning its operation to achieve sufficient constancy of driver pressure for a sufficient duration.
3. The monetary cost of the driver assembly is very high since the structural requirements are very high.

In order to achieve a high temperature in the driver gas, large compression ratios are typically used, therefore the volume of driver gas at diaphragm rupture is relatively small. If the piston is moving with relatively low velocity at this point, the driver gas slug has approximately constant volume. The unsteady expansion will therefore lead to a rapid pressure drop in the driver gas. The effect of this pressure drop is then transmitted downstream as a reflected $u + a$ characteristic, potentially interfering with downstream flow processes before or during the test time [44].

We have recently been trying to produce high Mach number, high static pressure flow conditions in the X2 expansion tube facility, however, initial attempts did not achieve expected results. The existing 35 kg piston is relatively heavy for the length of compression tube and therefore is operated at slow speeds; the result being that the driver gas maintains its pressure for a relatively short duration. For the high speed flow conditions for which X2 is typically used (such as planetary entry between 6 and 10 km/s), critical flow processes occur in the test section before the reflected $u + a$ characteristic from the driver reaches the test section, and target flow conditions are therefore achieved.

However, considering the slower shocks generated through the dense test gas for high total pressure conditions, early pressure loss in the driver manifests itself in shock speeds which rapidly slow down before the critical flow processes reach the test section, preventing target flow conditions from being achieved. Table 2 summarises a Mach 13 high total pressure flow condition which was attempted with X2. Figure 20 shows several shock speeds measured at different points along the tunnel and compares these to theoretical estimates based on classical analytical calculations (i.e. the original target shock speeds).

Symbol	Value	Units	Description
$p_{A,0}$	1.1	MPa	Reservoir fill pressure, Air.
$p_{D,0}$	30.0	kPa	Driver fill pressure, 100% Helium.
p_{rupt}	15.5	MPa	Primary diaphragm rupture pressure.
λ	42.5	[-]	Driver compression ratio.
m_p	35.0	kg	Piston mass.
p_{sec}	150	kPa	Secondary driver fill pressure, Helium.
p_{shk}	330	kPa	Shock tube fill pressure, Air.
p_{acc}	254	Pa	Acceleration tube fill pressure, Air.
L_{sec}	3.424	m	Secondary driver tube length.
L_{shk}	1.301	m	Shock tube length.
L_{acc}	4.254	m	Acceleration tube length.
M	13.4	-	Predicted Mach number at nozzle exit; target $= 13.0$.
u	3.950	km/s	Predicted flow velocity at nozzle exit; target $= 3.952$ km/s.
p_0	$1,450$	MPa	Predicted total pressure at nozzle exit.
t_{tt}	0.063	ms	Predicted test time.

Table 2: Mach 13 calculated flow condition.

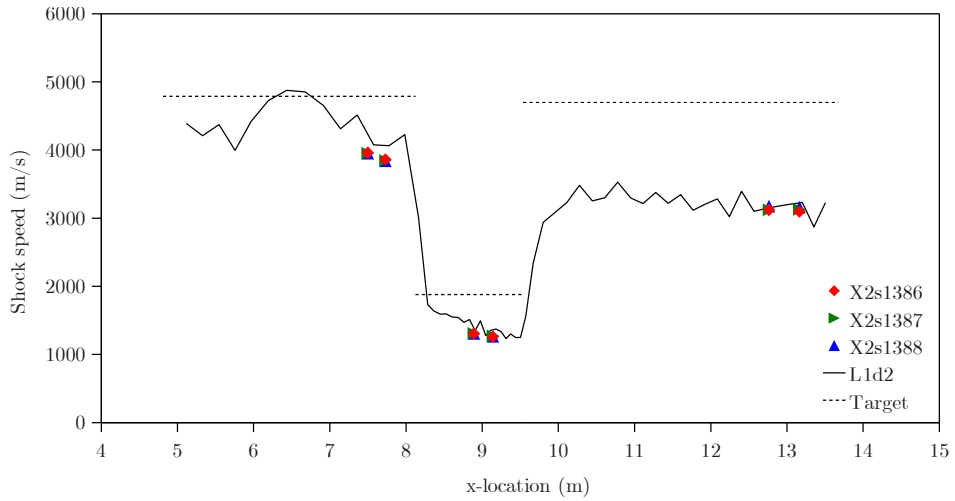

Figure 20: X2 shock speeds for Mach 13 condition, using 35 kg piston with 100% Helium driver. Data points denoted 'X2s...' indicate experimentally measured shock speeds.

Referring to Figure 20, shock speeds are seen to significantly attenuate, particularly in the high pressure (330 kPa initial fill pressure) air-filled shock tube. An analysis from `L1d2`, which shows predicted shock speed as the incident shock traverses the length of the tunnel, demonstrates good agreement with experimental results. This shock attenuation results in significantly reduced speed and total pressure in the test gas compared to the target flow condition. To address this problem, a new lightweight piston was developed for use in a tuned driver configuration, described in the next sections.

It is noted that a secondary driver was used for this experiment. The secondary driver is an intermediate tube filled with Helium, located between the primary diaphragm and the air-filled shock tube. It is configured so that the sound speed of the shock processed Helium in the secondary driver exceeds the sound speed of the expanded driver gas. This increase in sound speed across the interface between the two gases prevents transmission of transverse acoustic noise in the driver gas into the adjacent gas. If the air filled shock tube is used directly adjacent to the primary diaphragm, this sound speed increase is not achieved, resulting in significant unsteadiness in the test flow. This phenomenon is detailed in Paull and Stalker [45].

4.3.2 Tuned Piston Operation

The concept of tuned piston operation was originally proposed by Stalker in [44] and [46] and attempts to increase the duration over which driver gas is maintained at a useful pressure. It involves configuring the driver so that diaphragm rupture occurs while the piston still has sufficient velocity to compensate for driver gas loss to the shock tube [44]. Ignoring wave processes in the driver, there is a reference piston speed, U_{ref}, which will exactly compensate for driver gas loss into the shock tube, thus resulting in approximately constant pressure in the driver. The actual piston speed at the moment of diaphragm rupture, u_{rupt}, is non-dimensionalised by this reference speed, U_{ref}, to produce Itoh's [47] piston over-drive parameter, β:

$$\beta = \frac{u_{rupt}}{U_{ref}} \tag{126}$$

Stalker [46] proposed the idea of configuring the driver such that $\beta > 1$, thereby "over-driving" the piston. For $\beta > 1$, the piston will actually momentarily continue to increase the driver pressure following diaphragm rupture, before pressure begins to fall again. The duration of time over which this variation in

driver pressure is within acceptable limits (typically considered to be around 10% of the target pressure [48, 46, 44, 47]), can correspond to a significantly extended period of useful supply time. This concept is explained schematically in Figure 21.

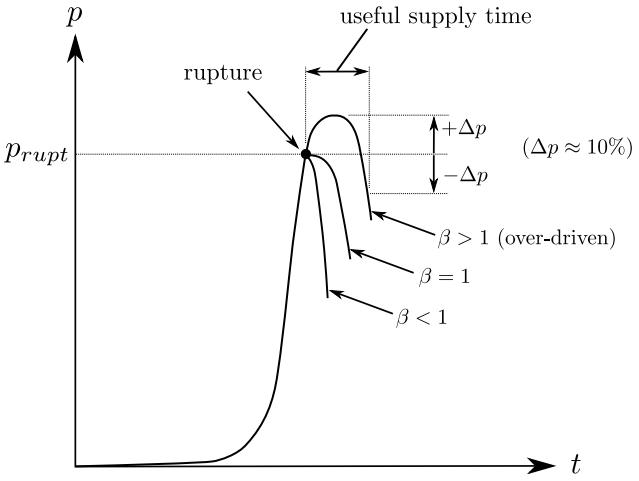

Figure 21: Effect of piston over-driving on driver pressure.

4.3.3 Piston Soft Landing Condition

Over-driving the piston results in the piston having a relatively large velocity (typically $100 - 300$ m/s) at the moment when the diaphragm ruptures. However, it is also necessary to stop the piston before it collides with the end of the compression tube, which can prove challenging since the distance available to decelerate the piston is relatively small for the high compression ratios required for driver performance. Itoh et al. [47] identified the types of motion possible, after diaphragm rupture, as the piston approaches the end of the compression tube. These are shown in Figure 22 and are defined as being either 'piston rebound', 'soft landing', or 'direct impact'. The eventual piston motion depends primarily on the properties and initial fill pressures of the reservoir and driver gases, the piston mass, and the geometry of the compression tube and reservoir. Itoh [47] proposes targeting the soft landing condition and sizing the piston buffer so that it catches the piston at its inflection point (where piston velocity and acceleration are simultaneously zero; i.e. $u_m = 0$ per Figure 22).

A soft landing condition was targeted for the new X2 free piston driver. It was considered impractical to incorporate brakes in the piston (which help prevent the rebound motion identified in Figure 22), and survivable direct impact is never feasible for anything other than low speed impacts. An analysis in accordance with Stalker [46] indicated that it was necessary to make the new piston as light as possible. Structural strength and facility interface requirements (i.e. the ability to use the piston with the existing compression tube and with the existing launcher arrangement) placed restrictions on how light the piston could be made. However, the final mass of 10.5 kg was determined to be sufficiently low to achieve a tuned driver condition which would have sufficient performance to achieve the target flow conditions. The new lightweight 10.5 kg piston is shown in Figure 23.

Considered qualitatively, tuned free-piston driver conditions require comparatively light pistons for the following reasons:

1. At the point of diaphragm rupture, the piston velocity needs to be high in order to match the mass flow of driver gas into the shock tube. Especially for a relatively short compression tube like X2's

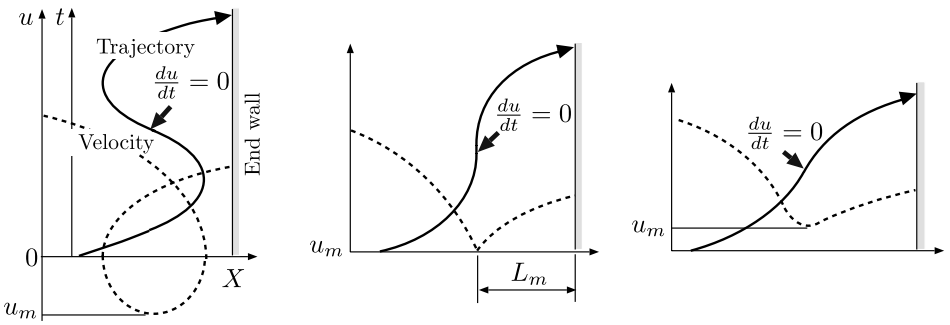

(a) Rebound impact $u_m < 0$

(b) Soft landing $u_m = 0$

(c) Direct impact $u_m > 0$

Figure 22: Characteristics of piston motion (taken from Itoh [47]). Subscript m refers to the instant when piston acceleration is zero; if $u_m = 0$ then the piston has an inflection point where it can theoretically be 'caught' by an appropriately sized buffer, thus avoiding impact.

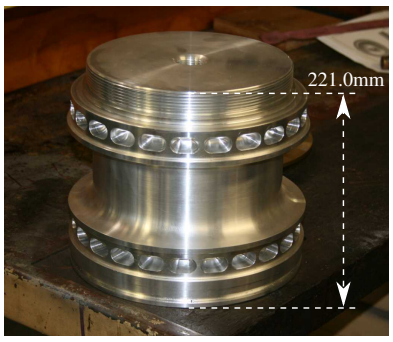

(a) Piston body, machined from 7075-T6 aluminium. Note: material removal across piston skirt, and circumferential pocketing.

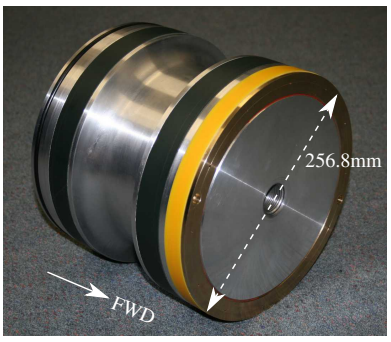

(b) Final piston assembly. Note: nylon chevron seal (yellow) and wear bands (dark green), and copper alloy seal support ring.

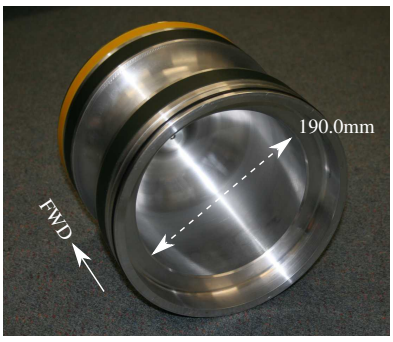

(c) Final piston assembly, viewed from behind. Note: internal cavity which interfaces with piston launcher.

Figure 23: New lightweight piston for X2.

(approximately 4.5m), a piston must be light enough to accelerate to a high speed over this short distance, or else reservoir pressures must become prohibitively high.

2. For large compression ratios, the distance between the piston and the end of the compression tube is quite short. For a given driver gas pressure at rupture, the piston needs to be very light to decelerate to rest over this short distance.

4.3.4 Calculation of New Free-Piston Driver Conditions

There are practically limitless combinations of parameters which will lead to tuned operation of a free piston driver, but several design constraints reduce the design space to a more manageable scale:

1. Piston mass: minimum piston mass is limited by structural and interface requirements (10.5 kg for X2's new lightweight piston).

2. Driver pressure: the compression tube is limited by the magnitude of pressure it can structurally contain (40 MPa for X2).

3. Reservoir pressure: the reservoir fill pressure, which accelerates the piston down the compression tube, is limited by reservoir structural strength (X2 has recently been temporarily rated to 8 MPa to permit operation of these driver conditions, however it has been designed for 10 MPa and will be re-rated accordingly at a future date).

4. Compression tube length and diameter: there is significant expense involved with changing the fundamental configuration of the facility, therefore compression tube geometry was assumed to be fixed.

Several variables remain available for driver condition design:

1. Reservoir fill pressure (0-8 MPa).

2. Driver fill pressure ($<$1 MPa).

3. Driver gas composition (Helium and Argon). The required piston speed for tuned operation depends on the speed of sound of the compressed driver gas. Reducing the sound speed (through the addition of Argon to Helium), reduces the required piston speed, however shock strength is also reduced.

4. Primary diaphragm thickness and material (in this study, diaphragm thickness was limited to 1.2, 2.0 and 2.5 mm thick, cold-rolled steel sheet; each was pre-scored to 0.2mm depth; rupture pressures were assumed to be 15.5, 27.9 and 35.7 MPa respectively, based on previous testing).

5. Buffer length (the distance from the extreme end of the tube where the piston makes contact with the buffer).

The process used to develop new driver conditions is outlined in Figure 24. The first step was to develop a rapidly solved 0-D perfect gas analytical model of the free-piston compression process. The piston equations of motion were obtained from Hornung [49] and used to predict piston motion and driver pressure before and after diaphragm rupture (assumed physical processes are shown in Figure 25). The 0-D model was used to manually identify a range of potential tuned driver solutions. The computational time was sufficiently small that each solution could be quickly identified.

Whilst the 0-D model proved capable of modeling the driver compression process fairly effectively, it could not make accurate predictions of required reservoir gas fill pressure. The reservoir gas expansion process was assumed to be an ideal unsteady expansion as shown in Figure 25b. With X2, reservoir gas must

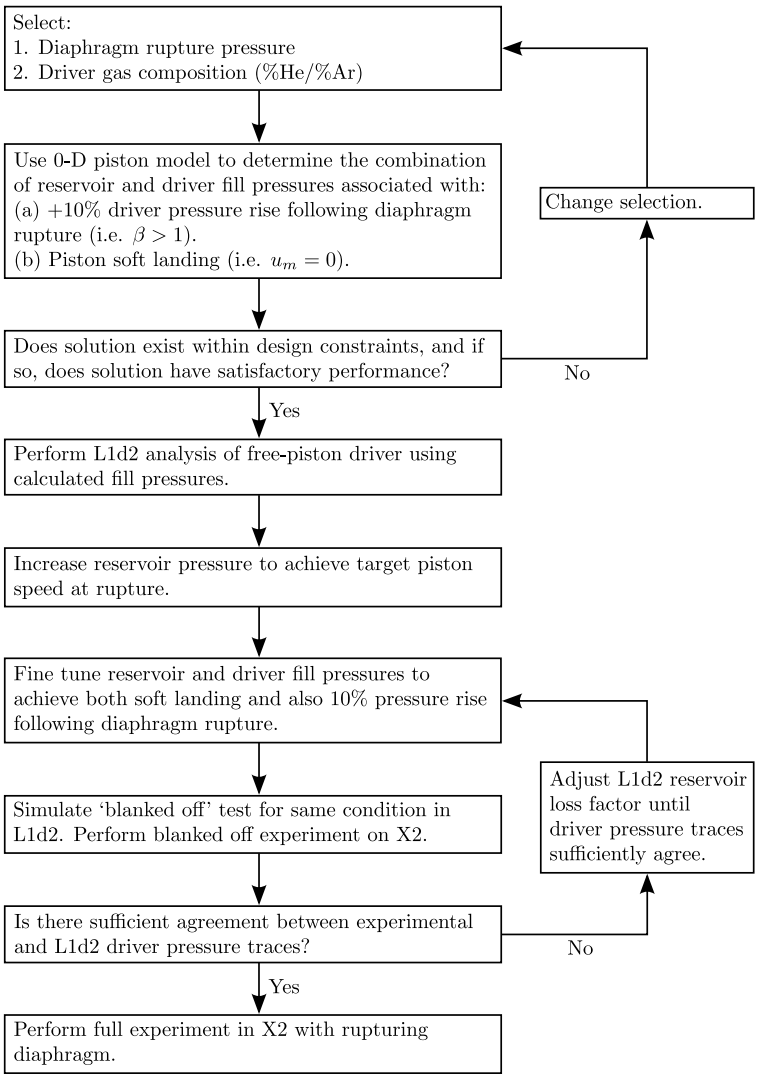

Figure 24: X2 free-piston driver condition development process.

pass through an area change and also through a slotted launcher (refer Figure 26). This convoluted flow path has the effect of throttling the expansion process, significantly reducing the strength of the reservoir pressure force eventually acting on the piston. Further, X2's reservoir has finite length, and the unsteady expansion through the reservoir eventually reflects from the extreme end and causes a further pressure drop. Both of these factors necessitate a much better predictive tool for the reservoir gas flow.

`L1d2` was used to fine tune the free-piston driver configuration prior to any experimental testing. The code is capable of capturing the longitudinal unsteady wave processes which occur during piston operation and includes piston friction, flow chemistry, and pipe-flow viscous effects along the tube walls. Gradual area changes can be handled by the code, however 3-D physical processes, such as flow through the launcher, cannot be directly modeled. To simulate the effect of these complex flow paths, `L1d2` uses loss regions, which apply a loss factor over a finite length of the tube where an area contraction etc. is present. Representative loss factors can only be determined from experimental data, therefore development of loss factors must occur in conjunction with experimental testing. There is no guarantee that a loss region will model a disturbed flow region with useful accuracy; however, anecdotal experience indicates that the modeling tool

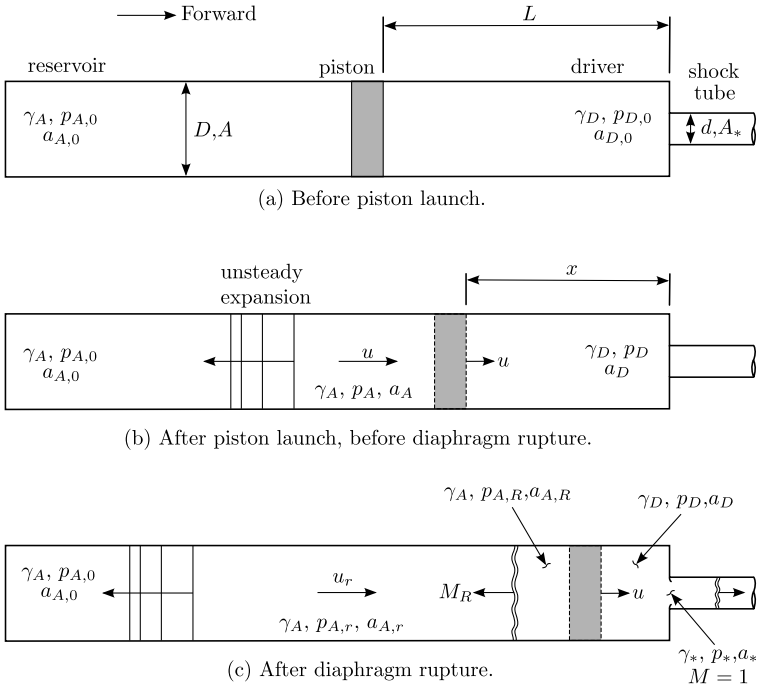

Figure 25: Assumed free piston driver states, pre- and post- diaphragm rupture.

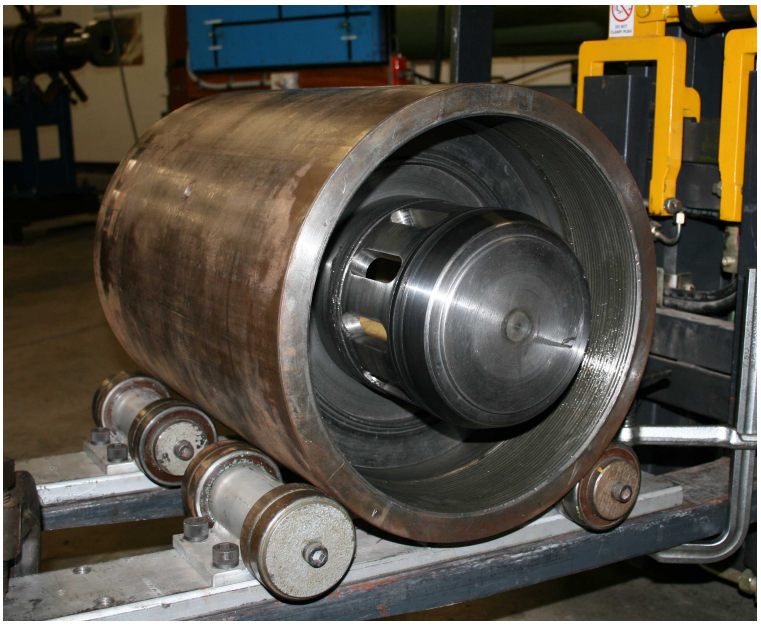

Figure 26: Piston launcher for X2 (shown detached from tunnel). Note: the launcher inserts into piston; reservoir gas must channel through the slots in the launcher, with significant resultant losses to the flow.

is quite effective once tuned for a given test condition. The `L1d2` driver geometry used to model X2 with the lightweight piston is shown in Figure 27.

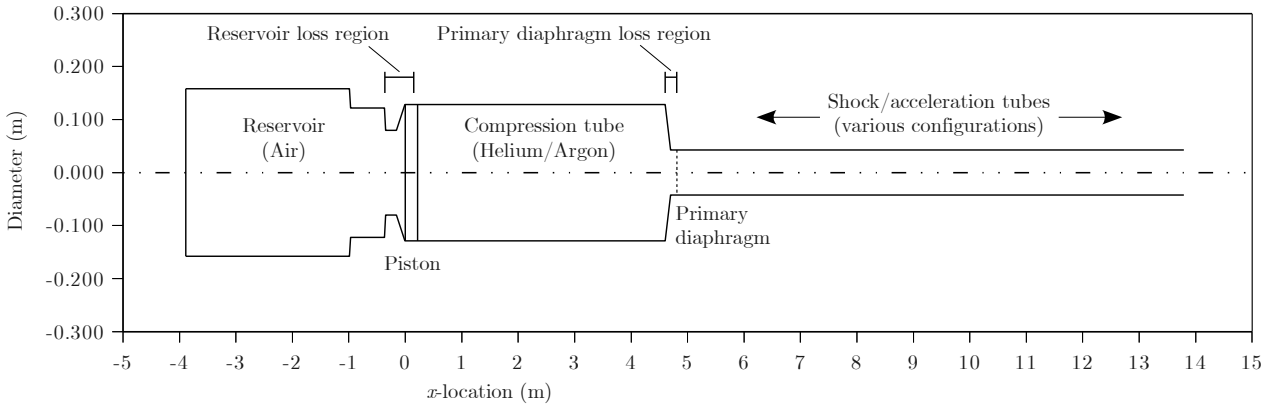

Figure 27: `L1d2` geometric representation of X2 impulse facility. Note: longitudinal scale has been compressed to fit diagram onto page.

Considering the existing 35 kg free piston driver for X2, the driver has been configured such that the amount of reservoir gas energy imparted to the piston is only a little greater than that required to rupture the steel diaphragm; for example, if the reservoir fill pressure is lowered by 10-20%, the piston will not have enough energy to raise driver pressure to the diaphragm rupture pressure, therefore the diaphragm will not rupture. The result is that the piston does not have significant energy following diaphragm rupture. Further, since the piston is heavy, this energy is not associated with a high velocity, therefore the risk of significant impact velocities into the end of the compression tube are low.

A key characteristic which differentiates tuned free-piston driver operation with the lightweight piston is that the piston is given significantly greater energy than that which is required to break the diaphragm, since it must also have sufficient energy to continue to push driver gas through the throat of the driver, at full pressure, *after* the diaphragm has broken. The lightweight tuned piston has to be accelerated to much higher velocities, be decelerated over a very short distance, and has significantly greater energy than that required to rupture the diaphragm. The risk of facility damage due to uncertainties in the analysis are much greater, therefore predictive tools must be as accurate as possible. To achieve this accuracy with `L1d2`, a series of blanked off tests was performed.

4.3.5 Blanked-Off Driver Tests

A blanked-off driver test involves operating a free-piston driver condition using a stiff, non-rupturing diaphragm, typically manufactured from thick steel. For this commissioning process, a PCB pressure transducer was located in the diaphragm, so that driver pressure could be measured during the piston compression process. During a blanked off test the piston bounces back and forth until the piston comes to rest. So long as the driver pressure does not exceed the facility pressure limit, no damage will be done to the piston. A corresponding analysis can be performed with `L1d2`. The `L1d2` model is then tuned until an acceptable level of correlation is obtained between the experimental and numerical pressure traces.

This methodology is very effective, since it allows full correlation of the driver pressure trace right up until the moment when the diaphragm rupture pressure is reached. At this point with a normal experiment, the diaphragm would then rupture, initiating shock tube flow. If strong agreement can be obtained with the

blanked off tests, then it increases confidence that the post-diaphragm rupture piston dynamics will also be predicted with good accuracy.

A broad analysis of different driver conditions using the 0-D analytical model, followed by detailed analysis with `L1d2`, eventually led to three driver configurations which were considered to be feasible. The three conditions each used an 80% Helium / 20% Argon driver gas mix. The difference between the conditions was the thickness of the cold-rolled steel diaphragm for each; 1.2 mm, 2.0 mm and 2.5 mm. Table 3 details the three new driver conditions.

			Fill pressures			
Driver condition ID [−]	Piston mass [kg]	Diaphragm thickness[1] [mm]	$p_{A,0}$ [MPa]	$p_{D,He,0}$ [kPa]	$p_{D,Ar,0}$ [kPa]	Buffer Length[2] [mm]
LWP-1.2mm-Rev-0	10.524	1.2	4.94	88.2	22.1	100
LWP-2.0mm-Rev-0	10.524	2.0	6.85	74.3	18.5	45
LWP-2.5mm-Rev-0	10.524	2.5	6.08	61.7	15.5	45

[1] Diaphragms are manufactured from cold-rolled steel and pre-scored to 0.2 mm depth.
[2] Buffer is comprised of 6x50 mm diameter nylon studs.

Table 3: X2 lightweight piston finalised driver conditions.

Blanked-off tests were performed for each condition prior to performing diaphragm rupturing experiments. Figures 28(a-c) compare pressure traces between `L1d2` predictions and experimental measurement. Close correlation is observed for the average pressure magnitudes. There is some difference in the unsteady behaviour (waviness); it was found that `L1d2` had difficulty predicting the detailed unsteady behaviour of the driver pressure through the sharp area change to the primary diaphragm. The `L1d2` pressure traces are taken just before the compression tube area reduces. It was found that loss factors had to be increased from 0.5 (which is used with the existing 35 kg piston `L1d2` model) to approximately 3.5 for the lightweight piston, to obtain good agreement between numerical and experimental driver pressure traces. This is not surprising, since the reservoir pressures are almost an order of magnitude higher, and the piston velocity and acceleration are also much higher.

It is also noted that for blanked-off experimental tests with 2.0 and 2.5 mm steel diaphragms, the driver pressure was scaled upwards to ensure peak pressure did not exceed the facility limit of 40 MPa. Since reservoir pressure has proven most difficult to predict accurately, the reservoir pressure was not scaled. Prior to the rapid increase in driver pressure as the piston nears the end of its stroke, piston dynamics is primarily dependent on reservoir pressure (i.e. driver pressures are low for most of the piston stroke). Therefore these scaled blanked-off tests still permit reasonable verification of most of the compression process.

Since `L1d2` uses a pipe flow model to calculate heat loss, it does not predict heat loss well for a compression process where the gas is very hot, but only moving with relatively low velocity (i.e. for a heavy, slow piston). For these experiments, the volumetric compression ratio of the driver gas at the end of the piston stroke was measured experimentally using sacrificial soft metal rods fixed into the end of the tube, and it was found that the volumetric compression ratio was well approximated by the `L1d2` simulations. This indicated that heat loss was not significant during the compression process.

Figure 29 shows the `L1d2` predicted piston velocity-displacement trajectory for driver condition LWP-2.0mm-Rev-0 from Table 3. It can be seen that the deceleration of the piston prior to reaching the inflection point is significant and that incorrectly locating the buffer too far forward of the tube end may result in very high speed impact. Driver heat loss is very important in this respect, since significant heat loss will result in a smaller driver gas volume at high pressure and, if not properly modeled, may result in the buffer being located too far forward.

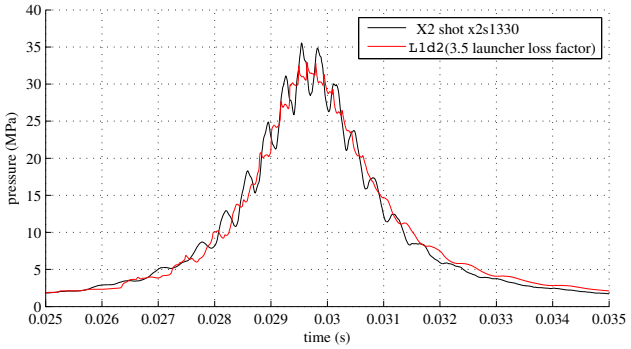

(a) Driver condition LWP-1.2mm-Rev-0 (100% driver fill pressure / 100% reservoir fill pressure)

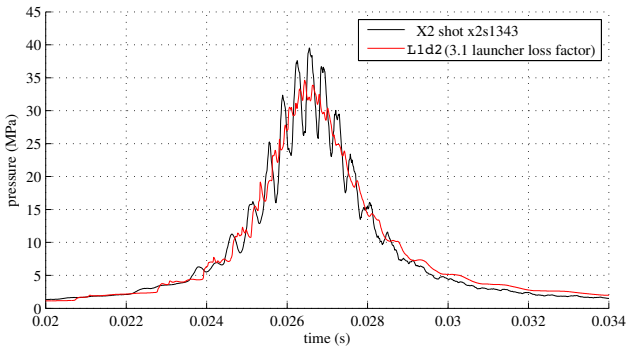

(b) Driver condition LWP-2.0mm-Rev-0 (162% driver fill pressure / 100% reservoir fill pressure)

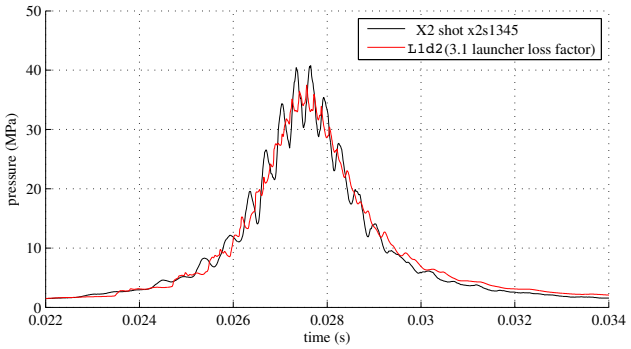

(c) Driver condition LWP-2.5mm-Rev-0 (170% driver fill pressure / 100% reservoir fill pressure)

Figure 28: Comparison of experimental and numerical driver pressures for new tuned lightweight piston driver conditions (refer Table 3). Experimental pressure traces have been time-shifted to match `L1d2` predictions.

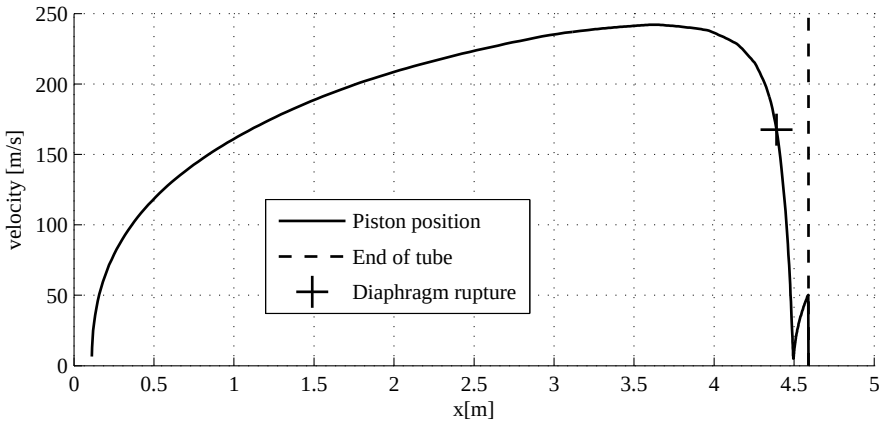

Figure 29: Piston velocity vs. position along compression tube, driver condition LWP-2.0mm-Rev-0. To achieve a soft landing for the above example, a buffer should be located at the inflection point ($x = 4.5$ m). This is the position where the piston temporarilly comes to rest before being pushed forwards again by residual reservoir gas pressure.

4.3.6 Shock Speeds with the Tuned Driver

Figures 30(a-c) show example experimental shock speeds for each of the three driver conditions described in Table 3. It can be seen that there is no longer the characteristic shock attenuation observed with the previous driver (refer Figure 20). With the 2.0mm and 2.5mm thick diaphragm conditions, target shock speeds are approached, thus achieving the original goals of the study.

It is noted that the three driver conditions detailed in Table 3 were achieved without damage to the facility. Nylon rods were used as the buffer to catch the piston; they are easily cut to a suitable length and have a high energy absorbing capacity. None of these new driver conditions caused damage to the nylon rods, indicating that the combined analytical/numerical/experimental development process managed to safely determine tuned, workable, driver conditions. This case study on the commissioning of the new lightweight piston for X2 has demonstrated a process which can be used to safely develop new driver configurations, and emphasises the use of the simulation code `L1d2` to fine tune piston response prior to experimentation.

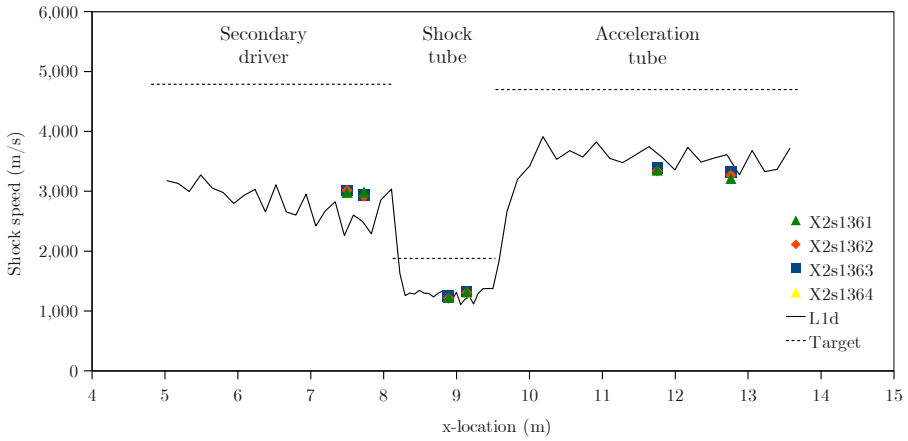

(a) Driver condition LWP-1.2mm-Rev-0

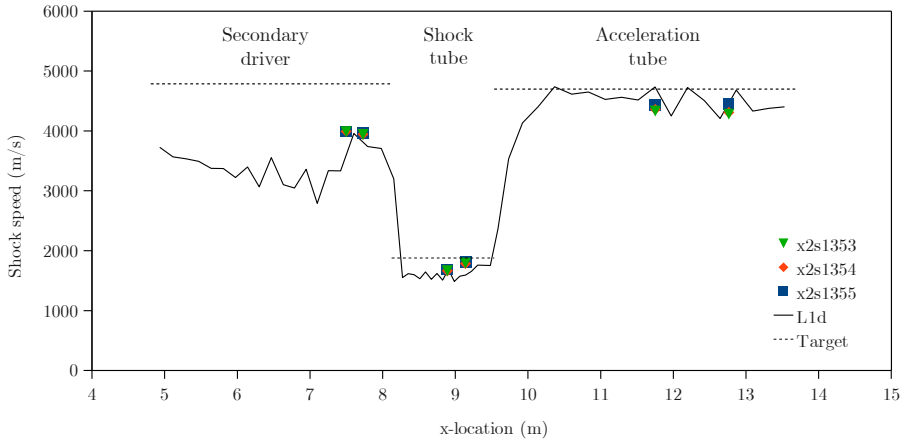

(b) Driver condition LWP-2.0mm-Rev-0

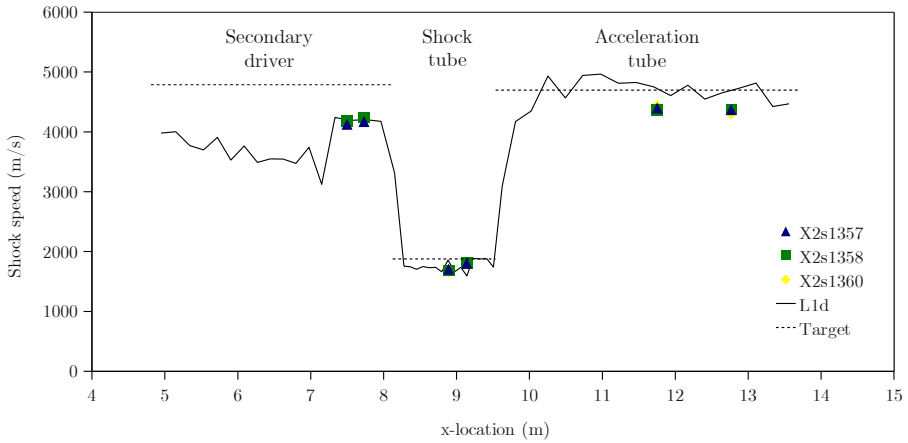

(c) Driver condition LWP-2.5mm-Rev-0

Figure 30: Comparison of experimental, analytical and numerical shock speeds for new tuned lightweight piston driver conditions (refer Table 3). Data points denoted 'X2s...' indicate experimentally measured shock speeds.

4.4 Hybrid simulation of the X2 expansion tube

As discussed in Section 2.2, there are three main processes that occur in an expansion tube:

1. free-piston compression and primary diaphragm rupture,
2. high pressure, low Mach number shock tube flow and secondary diaphragm rupture, and
3. low pressure, high Mach number acceleration tube, hypersonic nozzle and dumptank expansion.

For superorbital re-entry conditions, the first two stages involve all the important flow processes occurring at reasonably high pressures ($p > 100$ kPa) and low Mach numbers ($M < 4$), while the expansion of the test gas into the acceleration tube, nozzle and dump-tank quickly results in low pressures ($p \approx 10$ kPa) and high Mach numbers ($M \approx 10$). The hybrid simulation strategy proposed by Jacobs et al [50] makes use of these flow characteristics to simulate the X2 expansion tube in an efficient yet accurate fashion. The in-house quasi-one-dimensional Lagrangian code `L1d2` (see Section 3.1) performs well in the high pressure and low Mach number regimes where radial flow variation is small, and is therefore used for simulating the facility up to and including the secondary diaphragm rupture. As the test gas undergoes the unsteady expansion into the acceleration tube post secondary diaphragm rupture, the pressure drops drastically and the flow accelerates. The assumption of a radially uniform flow subsequently breaks down as the boundary layer development limits the shock propagation in accordance with the theory of Mirels [51]. The axisymmetric Navier–Stokes equations are therefore solved with the `mbcns2` code (see Section 3.2) to simulate this critical region of the facility. This hybrid simulation technique has been applied with success to an Earth re-entry condition in the X3 facility [50] and a Titan aerocapture condition in the X2 facility [52]. Here the hybrid simulation technique is applied to a 25 MJ/kg CO_2–N_2 expansion tunnel condition, with additional thermochemical nonequilibrium analyses of the secondary diaphragm rupture and steady nozzle expansion.

4.4.1 Operating Condition

A summary of the initial fill conditions, experimentally measured shock speeds and computationally simulated freestream conditions are shown in Table 4.

The Mars test gas was conservatively taken to be 96% CO_2 – 4% N_2 by volume, as recommended for the ESA *Radiation Workshop* test case TC2-M1 [53]. A sample population of 23 shots with Pitot and static pressure measurements of the test flow are taken to be representative of the nominal condition — the experimental values shown in Table 4 are the means of this population. The calculated freestream conditions are obtained from the hybrid simulation technique to be described in the Section 4.4.2.

4.4.2 Formulation of Hybrid Simulation

The computational approach for expansion tunnel simulation implemented here considers two distinct stages:

1. One-dimensional Lagrangian simulation of the high pressure, low Mach number shock tube flow and secondary diaphragm rupture, and
2. Axisymmetric Navier–Stokes simulation of the low pressure, high Mach number acceleration tube, hypersonic nozzle and dumptank expansion.

The driver gas conditions at primary diaphragm rupture are estimated via an idealised analysis and therefore the piston compression is not simulated. In addition to the main flow simulation, separate analyses of thermochemical nonequilibrium during the secondary diaphragm rupture and steady nozzle expansion are performed. The regions of the X2 facility considered in each simulation component are illustrated in Figure 31.

Experimental parameters		*Hybrid CFD results*	
Fill conditions		**Simulated shock speeds**	
Reservoir	1.28 MPa Air	Primary shock, $U_{s,st}$	3300 ± 50 m/s
Compression tube	30 kPa 25.0% Ar–75.0% He	Secondary shock, $U_{s,at}$	6310 ± 220 m/s
Shock tube	3.5 kPa 96% CO_2–4% N_2	**Simulated freestream conditions** †	
Acceleration tube	9 Pa Air	Total enthalpy, h_{total}	24.7 ± 0.3 MJ/kg
Diaphragms		Velocity, u	6400 ± 50 m/s
Primary diaphragm	Scored 1.2 mm steel	Pitot pressure, p_{pitot}	65 ± 10 kPa
Secondary diaphragm	13 μm Mylar (or) 10 μm Al	Static pressure, p_{static}	350 ± 50 Pa
Measured shock speeds		Density, ρ	1.6 ± 0.10 g/m^3
Primary shock, $U_{s,st}$	3240 ± 50 m/s	Transrotational temp., T_{tr}	800 ± 100 K
Secondary shock, $U_{s,at}$	6340 ± 230 m/s	Vibroelectronic temp., T_{ve}	1050 ± 100 K
Measured freesteam conditions		Equivalent equil. temp., T	850 ± 100 K
Pitot pressure, p_{pitot}	85 ± 20 kPa	CO_2 mole fraction, X_{CO_2}	0.36 ± 0.04
Static pressure *, p_{static}	500 ± 170 Pa	Mach number, M	12.5 ± 0.5
Test time, t_{test}	150 μs	Unit Reynolds Number, Re/L	2.7×10^4 m^{-1}

Table 4: Fill conditions, shock speeds and freestream conditions for the 25 MJ/kg CO_2–N_2 expansion tunnel condition in the X2 facility.

* Experimental freestream static pressure measured at wall of nozzle exit.

† Simulated freestream conditions are averaged over the central 100 mm diameter core flow and first 100 μs of test time.

4.5 Free-piston compression and shock tube flow

The quasi-one-dimensional nature of the `L1d2` geometry can result in boundary layer heat loss being significantly under-estimated. Previous attempts at modeling the free-piston compression of the driver gas have demonstrated this inadequacy [54], with the driver gas temperature at primary diaphragm rupture being unreasonably high. The `L1d2` simulation of the shock tube flow is therefore begun at the moment of primary diaphragm rupture. The driver gas pressure and slug-length at rupture are obtained from an idealised model of the free-piston compression, whilst the temperature is obtained parametrically by matching the experimentally measured primary shock speed. Momentum loss at the primary diaphragm station area change is accounted for through a loss-per-unit-length factor K_L of 0.25. The CO_2–N_2 test gas is described by an equilibrium equation-of-state using the curve fits provided by the `CEA` program [55], as are the respective transport coefficients. The Ar–He driver gas is described as a mixture of ideal gases.

4.6 Light secondary diaphragm rupture

When the primary shock through the stagnant test gas reaches the light secondary diaphragm, the first few millimeters of shock-processed test gas are stagnated by the resulting reflected shock. For the condition at hand the ratio of the stagnated to freestream density of the test gas is approximately $10^4 : 1$ — taking area change into account and using the freestream conditions from Table 4, the observed 150 μs of test flow originates from within the first 2 mm of stagnated test gas. It follows that the subsequent expansion of this very small test gas volume through the acceleration tube and nozzle must be modeled accurately.

Diaphragms are typically modeled in `L1d2` as fixed-wall boundary conditions that are held in place for a small period of time to allow the reflected shock to form before being released. This method is referred to as the holding-time model, and is widely implemented due to its relative simplicity. Bakos and Morgan [56] demonstrated the limitations of the holding-time model through comparison with an inertial diaphragm model. Space-time representations of both the holding-time and inertial diaphragm models are

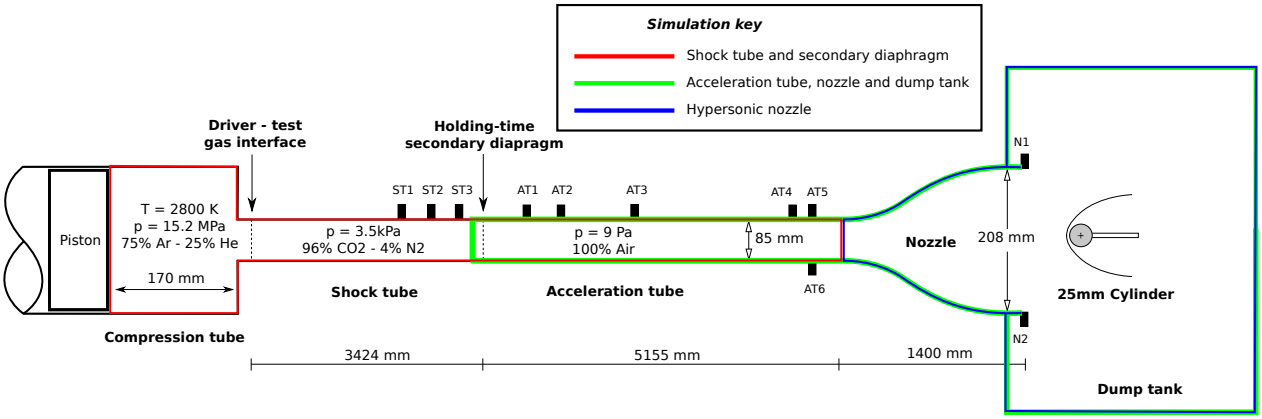

Figure 31: Regions of the X2 facility modelled in the present hybrid simulation technique

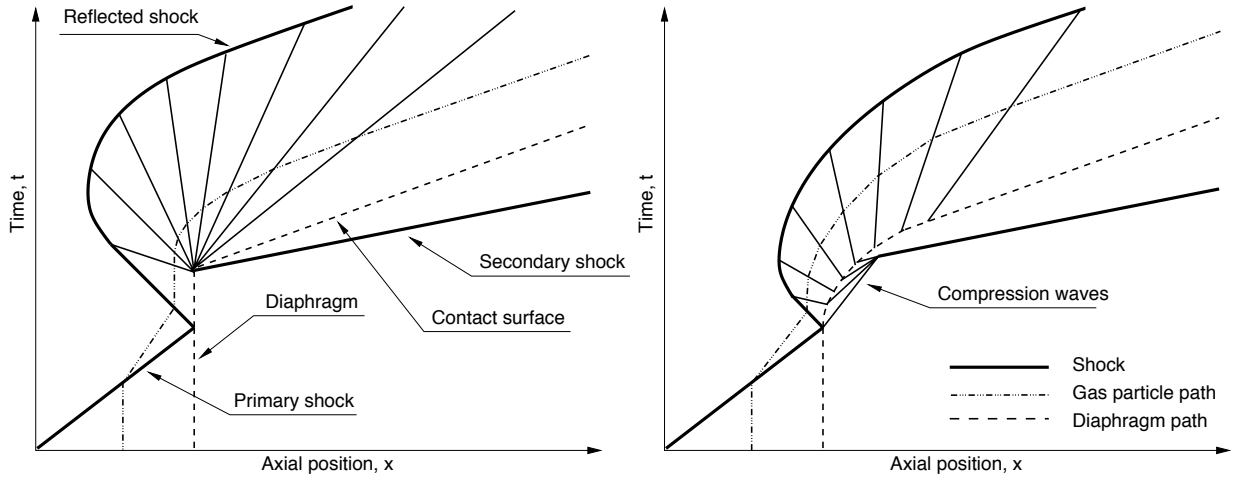

(a) Holding time model

(b) Inertial diaphragm model

Figure 32: Space-time diagrams of light secondary diaphragm rupture in an expansion tube (adapted from Bakos and Morgan [56]).

shown in Figure 32. The inertial diaphragm model represents the diaphragm as an ideal piston — the diaphragm shears cleanly at the tube wall, remains planar during its motion and provides only inertial resistance to the expanding test gas. Where a test gas particle immediately upstream of the secondary diaphragm experiences an infinite rate of expansion under the holding-time model, the inertial diaphragm model shows the contact surface must accelerate to an asymptotic limit over a finite period of time. The duration a test gas particle spends in the unsteady expansion directly determines the degree of thermochemical relaxation experienced — high expansion rates will result in frozen thermochemistry, while low expansion rates will tend towards equilibrium.

The light secondary diaphragms used for the sample population shots were 13 μm Mylar sheets weighing approximately 70 μg — the assumption that this sheet will stay intact through the entire test gas expansion is clearly invalid. A decaying inertial diaphragm model is therefore proposed for the present analysis, where the diaphragm reduces in mass exponentially after coming in contact with the hot stagnated test gas. The expression for the diaphragm mass m rate-of-change is taken to be:

$$\frac{dm}{dt} = \begin{cases} f_{\text{decay}} \times m \text{ for } m > m_{\text{limit}} \\ 0 \text{ for } m \leq m_{\text{limit}} \end{cases} \tag{127}$$

where f_{decay} is a time constant and m_{limit} an imposed lower mass limit to prevent numerical instabilities. Simulations of the secondary diaphragm rupture and subsequent unsteady expansion are performed for holding-time, inertial diaphragm and decaying inertial diaphragm models with finite-rate chemistry using the `L1d` code.

4.7 Acceleration tube, nozzle and dumptank flow

The axisymmetric flow solver `mbcns` is used for the low pressure, high Mach number acceleration tube, nozzle and dumptank flow. The computational domain is subdivided into a number of interconnected blocks, as illustrated in Figure 33, which allows the calculation to be parallelised over a distributed memory cluster computer.

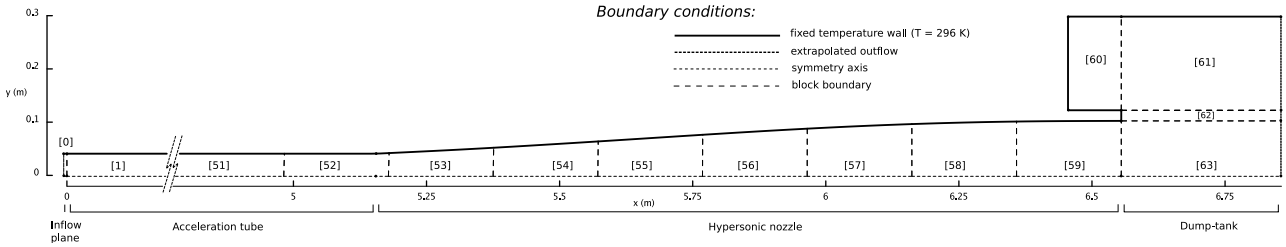

Figure 33: Computational domain for axisymmetric simulation of the X2 expansion tunnel downstream of the secondary diaphragm.

Although the holding-time secondary diaphragm rupture model is expected to underestimate test gas recombination through the unsteady expansion, it provides a simple pre-rupture flowfield that can be easily used to initialise the `mbcns` simulation. Using a holding-time of 10 μs the stagnated test gas slug is calculated to be 4 mm long at rupture. A 4 mm block thus precedes the acceleration tube, as shown in Figure 33, which is filled with the equilibrium stagnated test gas conditions. The upstream face of this block is a transient inflow boundary condition, applying the one-dimensional flow solution from the `L1d` simulation uniformally over the inflow plane.

Although thermal nonequilibrium is anticipated to occur during the nozzle expansion process, the inclusion of both thermal and chemical nonequilibrium for such a large-scale simulation is computationally prohibitive. Thermal equilibrium is therefore assumed for the Navier–Stokes simulations of the post-secondary diaphragm rupture flow, while separate inviscid simulations of the hypersonic nozzle are performed with the two-temperature model proposed by Park [57, 58]. The stagnated test gas upstream of the secondary diaphragm just prior to rupture contains negligible ionic species, and therefore only the neutral dissociation and exchange reactions listed in Table 5 (reactions 1 to 16) are included in the Navier–Stokes simulations.

4.7.1 Results and comparison with experiment

Lagrangian shock tube simulations A driver slug length of 170 mm and piston velocity of 50 m/s at primary diaphragm rupture was determined through an idealised model of the free-piston compression. A driver slug temperature of 2800 K was selected through the matching of experimental conditions in a parametric analysis. A comparison of the `L1d2` and experimental static pressure history from shot x2s248 is shown in Figure 34a. Shock arrival time observed in experiment at each transducer location is matched by the simulations within experimental and modeling uncertainties. Although the experimental data shows a higher initial pressure rise for transducer ST1, excellent agreement is shown for the first 800 μs of flow 0.5m downstream at ST3. A space-time representation of logarithmic pressure contours is shown in Figure 34b. The tail of

	Neutral reactions	Activation energy		Ionic reactions	Activation energy
Dissociation reactions			*Associative ionisation reactions*		
1	$CO_2 + M \Longleftrightarrow CO + O + M$	-526 kJ/mol	17	$N + O \Longleftrightarrow NO^+ + e^-$	-265 kJ/mol
2	$CO + M \Longleftrightarrow C + O + M$	-1073 kJ/mol	18	$O + O \Longleftrightarrow O_2^+ + e^-$	-670 kJ/mol
3	$N_2 + M \Longleftrightarrow N + N + M$	-941 kJ/mol	19	$C + O \Longleftrightarrow CO^+ + e^-$	-275 kJ/mol
4	$O_2 + M \Longleftrightarrow O + O + M$	-497 kJ/mol	*Charge exchange reactions*		
5	$NO + M \Longleftrightarrow N + O + M$	-628 kJ/mol	20	$NO^+ + C \Longleftrightarrow NO + C^+$	-193 kJ/mol
6	$CN + M \Longleftrightarrow C + N + M$	-590 kJ/mol	21	$O_2^+ + O \Longleftrightarrow O^+ + O_2$	-150 kJ/mol
7	$C_2 + M \Longleftrightarrow C + C + M$	-581 kJ/mol	22	$NO^+ + N \Longleftrightarrow O^+ + N$	-106 kJ/mol
Exchange reactions			23	$NO^+ + O \Longleftrightarrow O_2^+ + N$	-404 kJ/mol
8	$NO + O \Longleftrightarrow N + O_2$	-162 kJ/mol	24	$CO + C^+ \Longleftrightarrow CO^+ + C$	-261 kJ/mol
9	$N_2 + O \Longleftrightarrow N + O_2$	-319 kJ/mol	25	$O_2 + C^+ \Longleftrightarrow O_2^+ + C$	-78 kJ/mol
10	$CO + O \Longleftrightarrow C + O_2$	-575 kJ/mol	*Electron-impact ionisation reactions*		
11	$CO + C \Longleftrightarrow C_2 + O$	-48 kJ/mol	26	$C + e^- \Longleftrightarrow C^+ + e^- + e^-$	-1087 kJ/mol
12	$CO + N \Longleftrightarrow CN + O$	-321 kJ/mol	27	$O + e^- \Longleftrightarrow O^+ + e^- + e^-$	-1318 kJ/mol
13	$N_2 + C \Longleftrightarrow CN + N$	-193 kJ/mol			
14	$CN + O \Longleftrightarrow NO + C$	-121 kJ/mol			
15	$CN + C \Longleftrightarrow C_2 + N$	-11 kJ/mol			
16	$CO_2 + O \Longleftrightarrow O_2 + CO$	-231 kJ/mol			

Table 5: Neutral and ionic chemical reactions from the CO_2 – N_2 reaction scheme of Park et al [58] (Note that the photo-ionisation reactions have been omited).

the expansion fan eminating from the primary diaphragm station can be seen to reflect off the compression–shock tube area change and eventually coalesce with the shock at $t = 700\,\mu$s. Stagnation conditions behind the reflected shock at diaphragm rupture were determined to be 10.3 MPa and 4370 K with an equilibrium CO_2 fraction of 30% by mass.

Secondary diaphragm rupture analysis Holding-time, inertial diaphragm and decaying inertial diaphragm models were compared in the analysis of secondary diaphragm rupture. Space-time plots of shock propagation obtained from finite-rate `L1d` simulations with the three secondary diaphragm models considered are shown in Figure 35a with experimental shock arrival times overlaid. The experimental transducer shock arrival times are bounded by the holding-time and inertial diaphragm solutions, with the holding-time model predicting the strongest secondary shock as expected. Implementing a decaying inertial diaphragm model with a time constant f_{decay} of $5 \times 10^4\, s^{-1}$ was found to match the secondary shock propagation observed in experiment.

CO_2 mass fraction distributions at $t = t_{rupture}+150\,\mu s$ for each of the Lagrangian simulations conducted are shown in Figure 35b. The test gas composition was found to be chemically frozen from this time onwards for all diaphragm models. The holding-time model gives the lowest levels of CO_2 recombination, with a much more pronounced variation over the slug when compared to the relatively uniform inertial-diaphragm results. An unrealistically large initial rate of expansion for the test gas particles immediately upstream of the secondary diaphragm gives insufficient time for any recombination to occur before freezing occurs. The holding-time recombination levels only begin to approach that of the inertial diaphragm simulations at the very end of the test slug. The inertial diaphragm model with no mass decay shows significantly higher levels of CO_2 recombination and a more uniform distribution. The decaying inertial diaphragm model gives recombination levels bounded by the previous two models as expected, with an average CO_2 mass fraction in the test slug of 0.46. Assuming that the decaying inertial diaphragm model closely represents the physical

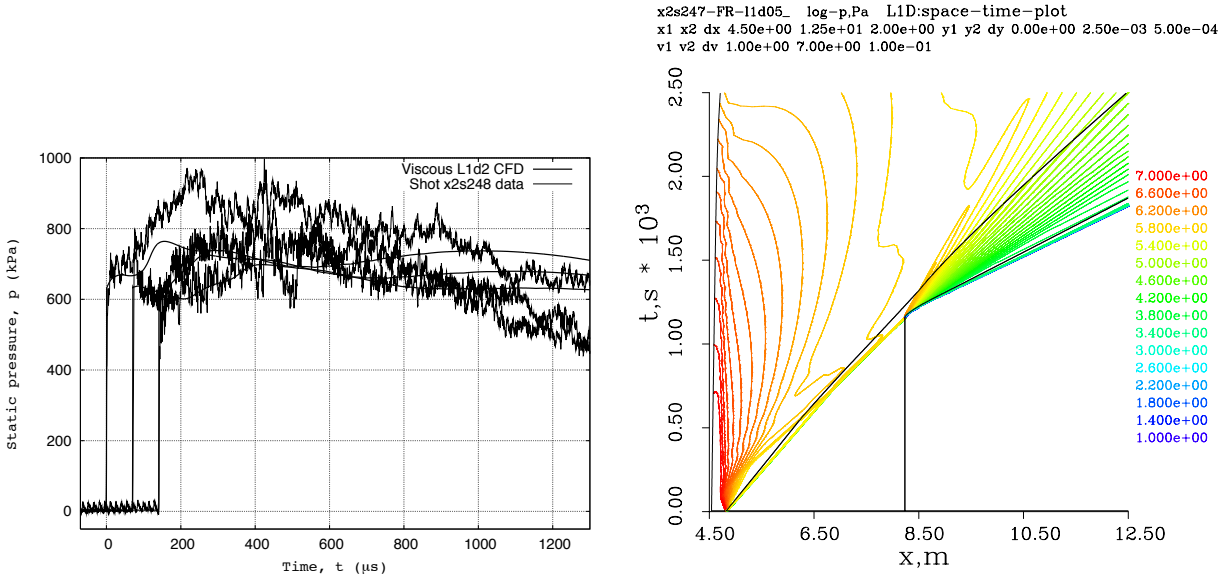

(a) Comparision of simulated and experimental static pressure traces in the shock-tube

(b) Space-time diagram of logarithmic pressure contours.

Figure 34: Results from quasi-one-dimensional Lagrangian shock tube simulation with equilibrium chemistry.

rupture behaviour, implementing a holding-time rupture model to initialise the Navier–Stokes simulations will result in CO_2 levels being underpredicted by between 25% and 4% over the test time.

Navier-Stokes expansion tunnel simulation Viscous Navier-Stokes simulations of the expansion tunnel flow were conducted with finite-rate chemistry and a pre-rupture flowfield described by the `L1d2` solution with a holding-time secondary diaphragm. Initial simulations with 37 $\times$ 4500 cells in the acceleration tube and a stagnated test gas slug length of 2mm resulted in unphysical pockets of hot, low density gas forming along the axisymmetric axis. Increasing the cell distribution to 43 $\times$ 5155 (1 mm squares, average) reduced this phenomena slightly, however disturbances were still observed during the test time. The test gas slug length was increased to 4 mm, corresponding to a hold-time of 10 μs, and the disturbances no longer formed during the test time. The stability of the flow during the test time for this final simulation is illustrated in the contours of pressure through the nozzle, Figure 36. The freestream conditions from this simulation are shown in Table 4.

A comparison of the `mbcns2` solution with experimentally obtained pressure traces is shown in Figure 37. The simulated secondary shock propagation shown in Figure 37a closely matches that of shot x2s247 which is close to the mean of the sample population. Good agreement with experiment is shown for both static and Pitot pressure at the nozzle exit for the first 200 μs of flow, Figures 37b and 37c. The simulated Pitot pressure profile 100 mm downstream of the nozzle exit shows reasonable agreement with that obtained through the experimental Pitot pressure survey, Figure 37d. For the central 100 mm of flow a test article is likely to occupy slight property variation exists, most noticeably at the extremities which has Pitot pressure 10% higher than at the central axis. Overall, the `mbcns2` simulation shows sufficient correlation with experiment to proceed with further validation through bluntbody shock layer simulations.

Nonequilibrium nozzle expansion analysis The averaged nozzle entrance conditions from the viscous, thermal equilibrium `mbcns` expansion tunnel simulation were used as initial conditions for inviscid, thermal

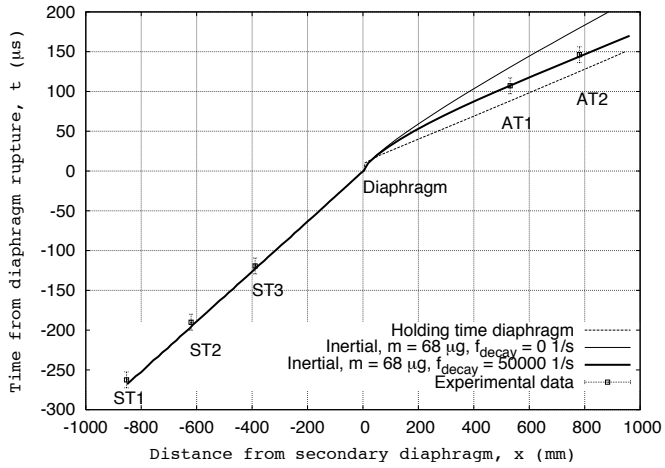

(a) XT diagram from ST1 to AT2.

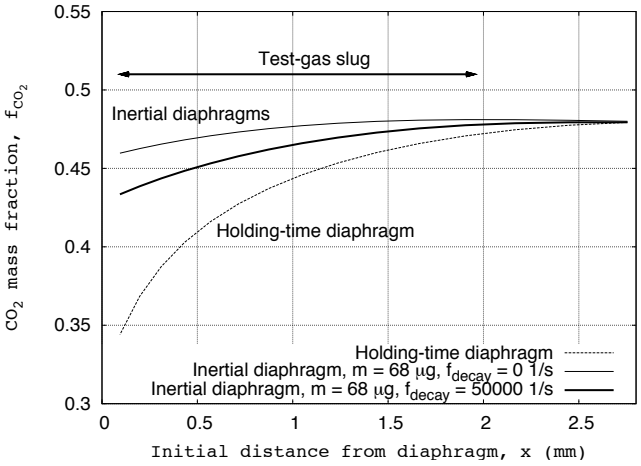

(b) Test gas CO_2 mass fractions 150 μs after rupture.

Figure 35: Comparison of shock propagation and test gas recombination for various light secondary diaphragm models.

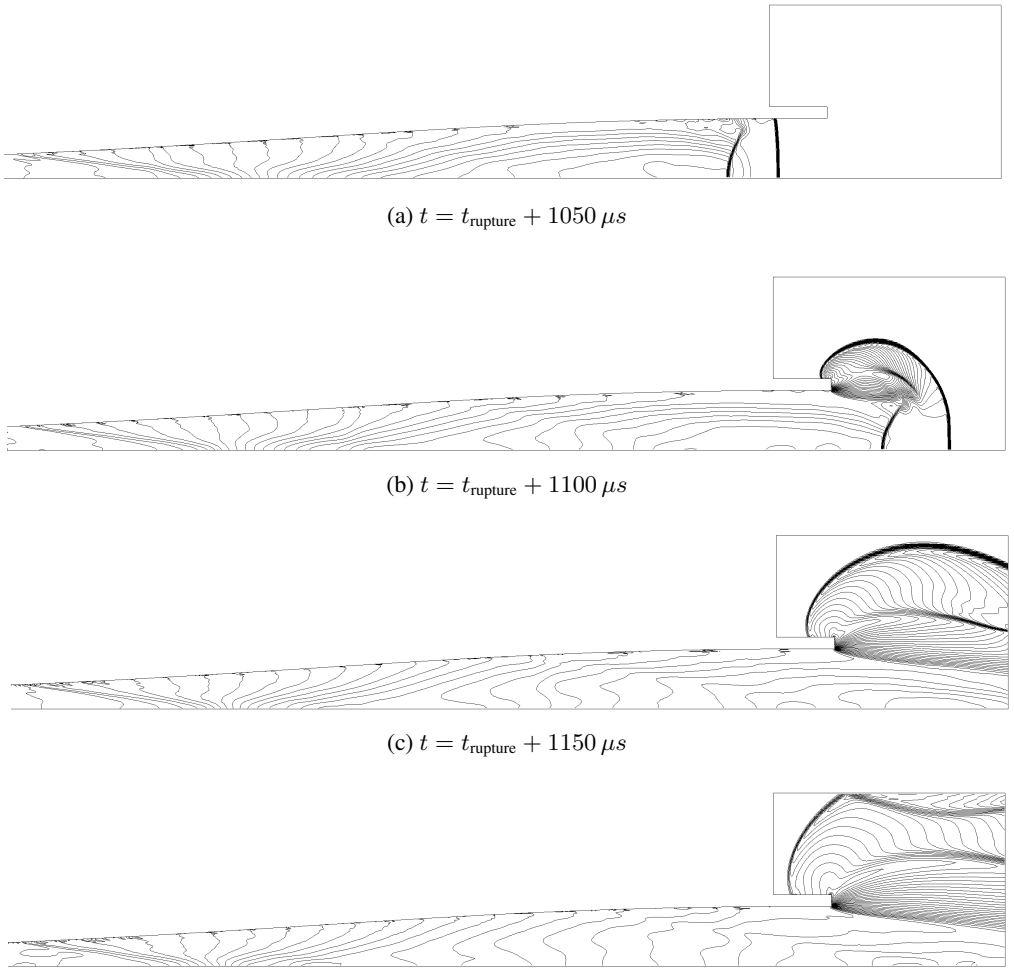

(a) $t = t_{\text{rupture}} + 1050\,\mu s$

(b) $t = t_{\text{rupture}} + 1100\,\mu s$

(c) $t = t_{\text{rupture}} + 1150\,\mu s$

(d) $t = t_{\text{rupture}} + 1200\,\mu s$

Figure 36: Static pressure contours through the hypersonic nozzle during test gas expansion.

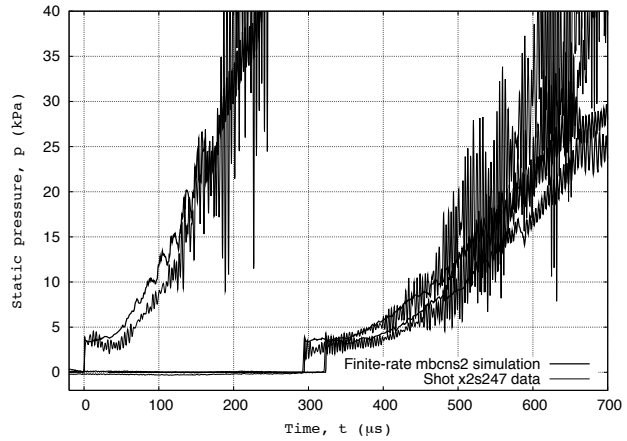

(a) Static pressure history at AT3, AT4 and AT5.

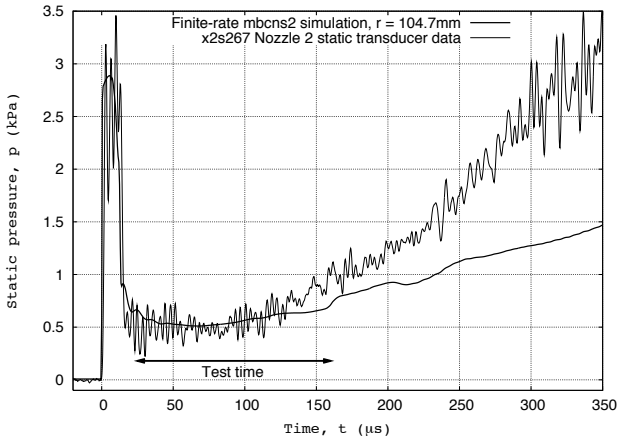

(b) Static pressure history at nozzle exit.

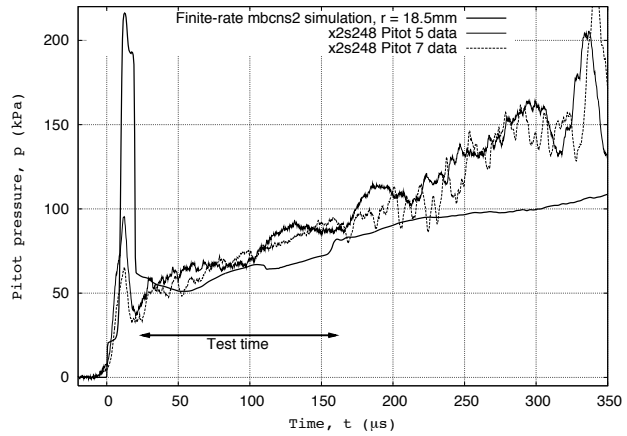

(c) Pitot pressure history 100 mm downstream of nozzle exit.

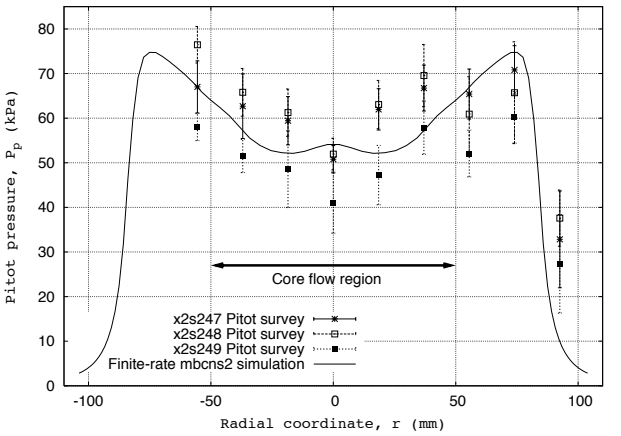

(d) Pitot pressure profile 100 mm downstream of nozzle exit at $t = t_{\text{rupture}} + 1175\mu s$.

Figure 37: Comparison of computational and experimental pressures through the acceleration tube and nozzle.

nonequilibrium simulations of the hypersonic nozzle expansion. Test gas temperature contours through the nozzle after 800 μs of flow are shown in Figure 38a, while the respective centreline temperature profile is shown in Figure 38b. Both temperatures along the centreline are seen to remain constant until the Mach cone arrives 250 mm downstream of the nozzle entrance. The transrotational temperature then begins to drop rapidly as the test gas expands, while the vibroelectronic temperature relaxes at a much lower rate. After 800 mm the transrotational temperature along the centreline is essentially frozen at 800 K while the vibroelectronic temperature continues to slowly relax. The flow close to the nozzle wall remains in a state of thermal equilibrium at 1100 K through the entire length due to a much weaker expansion than at the centreline. Slightly increased relaxation begins to occur as the test gas expands into the dump tank, resulting in a final temperatures 100 mm downstream of the nozzle exit of $T_{ve} \approx 1050$ K and $T_{tr} \approx 800$ K.

4.7.2 Quality of the Solution

A hybrid simulation technique for the X2 expansion tube incorporating a one-dimensional Lagrangian simulation of the shock tube and secondary-diaphragm and an axisymmetric Navier–Stokes simulation of the acceleration tube, nozzle and dump-tank has been applied to a 25 MJ/kg CO_2–N_2 condition. Good agree-

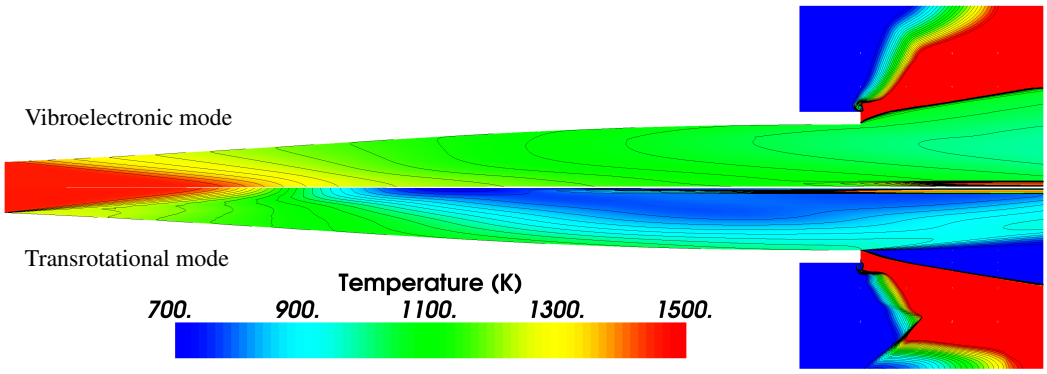

(a) Contours of temperature.

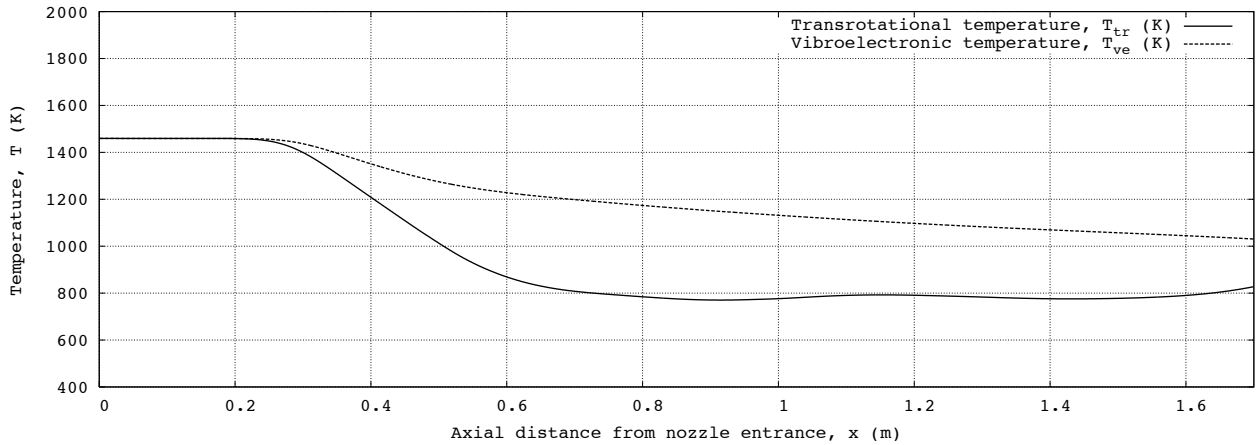

(b) Centreline temperature profiles.

Figure 38: Test gas temperature distributions through the hypersonic nozzle after 800 μs of flow.

ment with experimentally measured static pressure traces and shock speeds was obtained in both the shock and accerlation tubes, and Pitot pressure was also found to be accurately predicted in the test-section. Although the application of a simplified holding-time model allows the shock propagation and pressure levels to be accurately reproduced in the Navier–Stokes simulation, test gas recombination following secondary diaphragm rupture was found to be under predicted by as much as 25 % when compared to a simulation considering an inertial secondary diaphragm. Furthermore considerable thermal nonequilibrium is shown to develop through the steady nozzle expansion, with T_{ve} and T_{tr} deviating by 24 % and -6 % respectively from the equilibrium temperature T_{eq}. Therefore while the density, pressure and velocity obtained via the hybrid simulation technique is considered to be accurate, the species mass-fractions and thermal equilibrium temperature are considered approximate only.

4.8 Axisymmetric simulation of the X2 shock tube

4.8.1 Experiment discription

A comprehensive set of shock tube experiments with a representative Titan test gas (98% N_2 & 2% CH_4 by volume) over a pressure and velocity range of 2 to 1000 Pa and 4 to 10.5 km/s respectively were conducted by Brandis [59] in the X2 facility. Following the work of Gollan [60, 61], a 1 Torr 5.7 km/s condition was the focus of a recent computational study [62] where the CN Violet radiation intensity predicted by a one-dimensional and an axisymmetric simulation were compared with experiment. The aim of the study was to assess the assumption of one-dimensional variation of properties during the test-time, as the optical line-of-sight passes through the expanding boundary layer and Mach cone in the test section.

Table 6 summarises the fill conditions, shock speeds and spectral measurements performed in the X2 experiments that were simulated.

Shot number	**x2s522**	**x2s645**
Driver gas composition *	86.0% He, 14.0% Ar	
Primary diaphragm burst pressure	15.1 MPa	
Test gas composition *	98% N_2, 2% CH_4	
Shock speed, U_s †	5697 ± 54 m/s	5658 ± 53 m/s
Pressure, p_∞	133 ± 0.5 Pa	
Exposure time, $t_{ex.}$	100 ns	
Spectrometer range	308-450 nm	

Table 6: Two X2 shots targeting a 1 Torr 5.7 km/s Titan entry condition

* Gas percentage compositions are by volume

† Given shock speed is that between transducers AT5 and AT7 (see Figure 4)

Two shots x2s522 and x2s645 were both performed with an initial test gas pressure of approximately 1 Torr targeting a shock speed of 5.7 km/s; the measured shock speeds matched this within the bounds of measurement uncertainty. Although the pressure of this condition is an order of magnitude higher than that of Huygens-type direct entry peak heating [63], it is a useful condition for investigating the chemical kinetics of Titan gas closer to thermochemical equilibrium.

4.8.2 Formulation of Axisymmetric Simulation

The axisymmetric Navier–Stokes simulation technique implemented here is based on that described in Ref. [60], however the driver gas conditions are assumed to be uniform (T=3450 K, p=15.1 MPa, u=0 m/s) at diaphragm rupture for the present work. A single-temperature gas model is implemented alongside the Gökçen [64] chemical reaction scheme where the ionic reactions have been omitted. This relatively low order thermochemistry model was used due to computational resource constraints. The computational domain for the axisymmetric Navier–Stokes simulation of shot x2s522 is presented in Figure 39. The computational domain extends from the front piston face to 1 m into the dump-tank; the remaining length of the dump-tank is not included.

Again, the simulations were performed with the `mbcns2` code described in Section 3.2. The computational domain is decomposed into 160 roughly equally sized blocks – 5 in the compression tube cavity, 123 along the shock-tube and 32 in the dump-tank. Two grid resolutions were considered – (a) 20×2000 cells in the shock-tube and (b) 40×4000 cells in the shock-tube. The cell discretization in the compression cavity and dump-tank are matched to the shock tube on a cell per unit area basis. The higher resolution

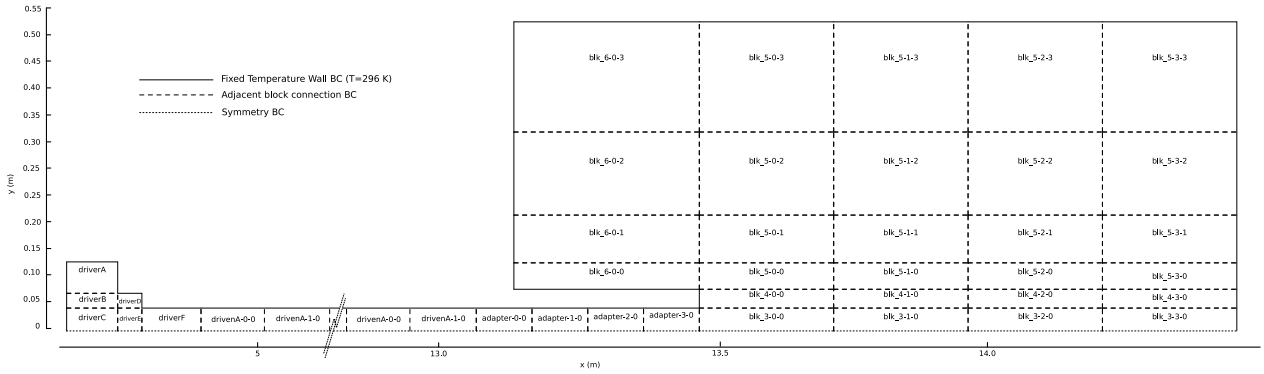

Figure 39: X2 computational domain for axisymmetric Navier–Stokes simulation of shot x2s522

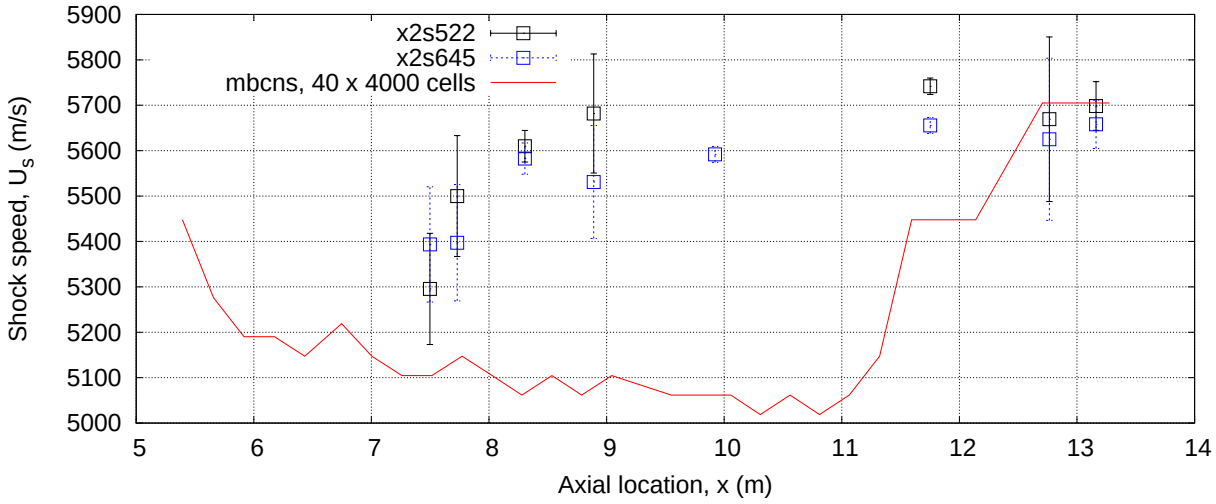

Figure 40: Comparison of shock-speed from experiments and simulations for the 1 Torr X2 condition

simulation has a total of 580,180 cells. The simulations were run on 40 quad-core Intel Woodcrest nodes and the 40×4000 simulation required approximately 140 hours for completion.

4.8.3 Results and comparison with experiment

Figure 40 compares the shock-speeds measured from experiment and those obtained from the computational simulations. The shock speeds from experiment are determined by locating the arrival time of the shock at each of the 8 pressure transducers along the shock tube and calculating the time-of-flight in between each pair. The spatial uncertainty is 1 mm and the temporal uncertainty is nominally 1 μs. Although the 40×4000 cell simulation agrees with the experimentally measured shock speed of approximately 5.7 km/s at the tube exit, the shock propagation through the shock tube is quite different. The experiments show a quick initial rise and then plateau in shock speed in the first 2 meters after the primary diaphragm, whilst the sudden rise in the simulations is only 2 meters from the tube exit. The sudden rise in shock speed is thought to be due to the reflected expansion wave catching-up with and accelerating the shock. The location of the shock/expansion wave interaction is determined largely by the initial temperature of the driver gas – for the present simulations this was set to 3,450 K which is approximately the isentropic compression temperature. If the driver gas compression process is not adiabatic the temperature of diaphragm rupture may be substantially less, and the the shock/expansion wave interaction location would be different.

The simulated and x2s522 static pressure traces at transducers ST1, AT4, AT5 and AT7 are compared in Figures 41a to 41d respectively. Generally the quantitative agreement with experiment is quite good. Of particular note, however, is the discrepancy in expansion wave arrival time at the ST1 transducer – in the experiment the arrival time is approximately 550 μs, while in simulation it is 600 μs. Such a large discrepancy so close to the primary diaphragm (3.5 m) indicates that the expansion of the driver gas is not being modeled correctly. By the AT4 transducer the simulated shock is in agreement with experiment, and this is reflected in the close agreement in the pressure histories at AT4, AT5 and AT7. Most critically, the post-shock static pressure level of approximately 50 kPa at the final transducer before the tube exit is matched almost exactly.

As described in Ref. [59], the spectral measurements in the X2 facility considered in the present work are made as the shock is expanding from the shock tube exit into the dump-tank (see Figure 3). Figure 42 displays CN mass fraction contours from the `mbcns2` simulation of the 1 Torr Titan condition as the shock emerges into the test section for spectral measurement. The spectral measurements are taken at approximately t=1720 μs. Comparing Figures 42a and 42e, the expansion of the shock layer into the test section is seen to alter the quasi-one-dimensional nature of the flow present inside the tube.

To evaluate the assumption that the emerging shock-layer remains approximately one-dimensional until the spectral measurements are taken, one-dimensional post-shock relaxation simulations with the `poshax` code are compared with the axisymmetric `mbcns2` simulations. Both simulations use the aforementioned 1 temperature thermal model with the reduced Gökçen [64] chemistry scheme. Figures 43a through 43c present comparisons of temperature, CN mole fraction and radiative intensity profiles, respectively, for the 1 Torr Titan condition in X2. The experimentally measured intensity profile from shot x2s645 is overlayed on Figure 43c and has been scaled to match the order of magnitude of the one temperature simulations. While the one-dimensional simulation uses the Rankine-Hugoniot relations to calculate the gas condition directly behind the shock (shock-slip is not considered), the finite-volume Navier–Stokes simulation captures the shock over a number of cells resulting in a diffused shock front. Furthermore the curvature of the shock as it emerges into the test section is only modelled in the axisymmetric simulations. These effects are evident in Figures 43a and 43b, where the change in temperature and CN mass fraction across the shock are more gradual in the Navier–Stokes simulations and peak at lower values. Consequently the calculated radiation intensity profile from the Navier–Stokes simulation exhibits a qualitative improvement over that from the one-dimension post-shock relaxation simulation, Figure 43c. The ratio of peak to equilibrium intensity is much closer in the Navier–Stokes simulation and the rise to the peak intensity immediately behind the shock is more realistic.

4.8.4 Quality of the Solution

The shock speed and static pressure levels calculated at AT5 and AT7 matched that measured in experiment, however the shock speed was under-predicted in the early stages of shock propagation. A better representation of shock propagation would require an axisymmetric simulation of the free-piston compression rather than the assumption of uniform driver properties at primary diaphragm rupture. Post-processing of the Navier–Stokes simulation data resulted in a radiation intensity profile that gave improved qualitative agreement with experiment compared to that from a one-dimensional post-shock relaxation simulation.

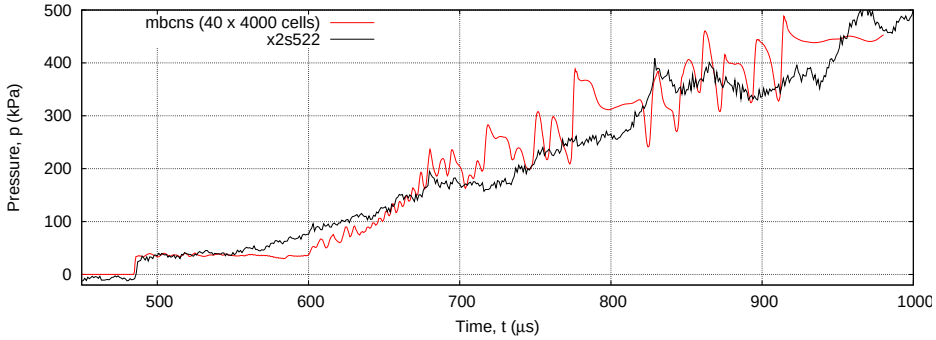

(a) ST1, x=7.381 m

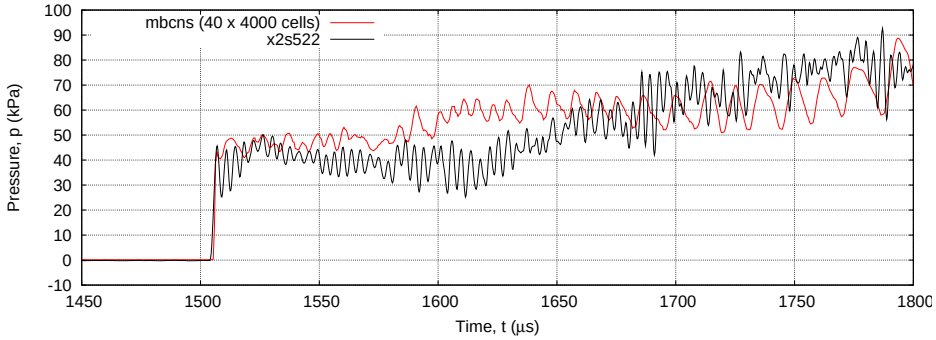

(b) AT4, x=12.675 m

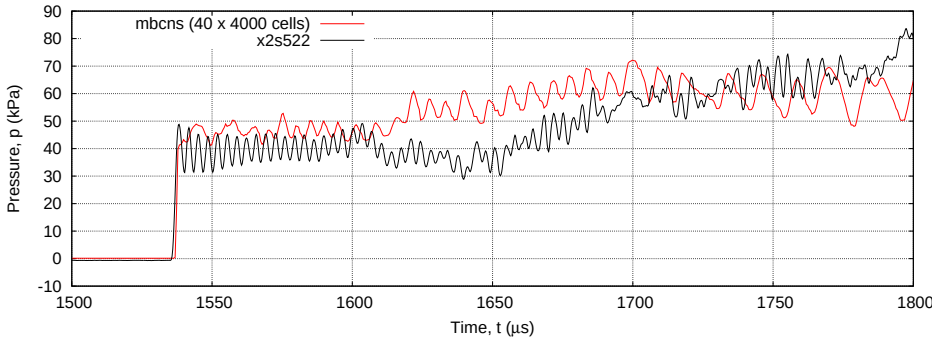

(c) AT5, x=12.855 m

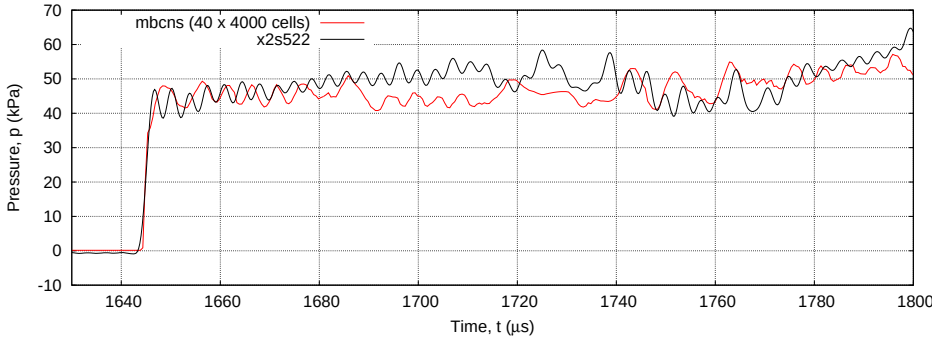

(d) AT7, x=13.469 m

Figure 41: Comparison of simulated and experimentally measured static pressure histories for the 1 Torr condition

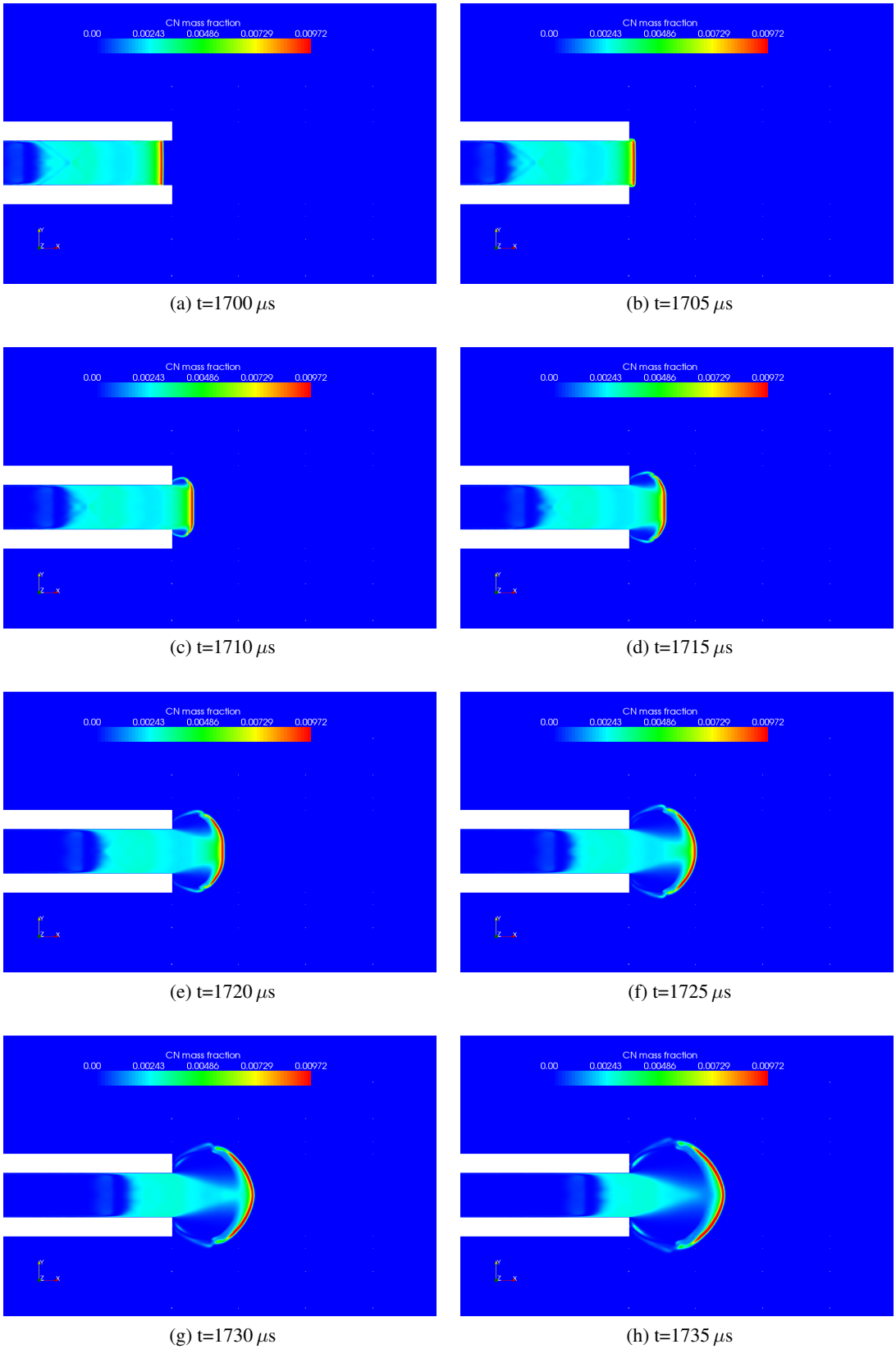

(a) t=1700 μs (b) t=1705 μs

(c) t=1710 μs (d) t=1715 μs

(e) t=1720 μs (f) t=1725 μs

(g) t=1730 μs (h) t=1735 μs

Figure 42: CN mass fraction contours from Navier–Stokes simulation of the 1 Torr Titan condition (x2s522) in the X2 facility. The spectral measurements are taken at approximately t=1720 μs.

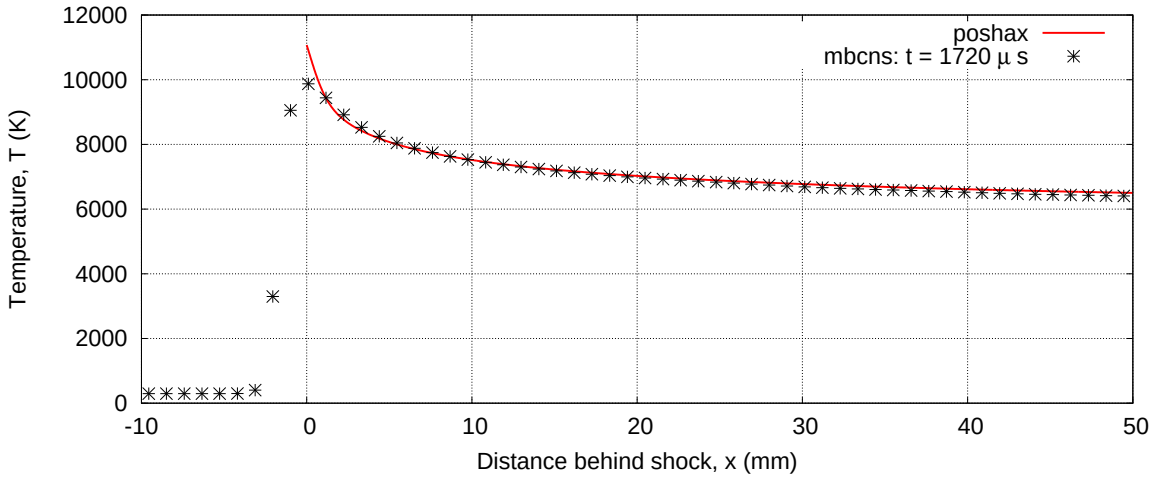

(a) Temperature

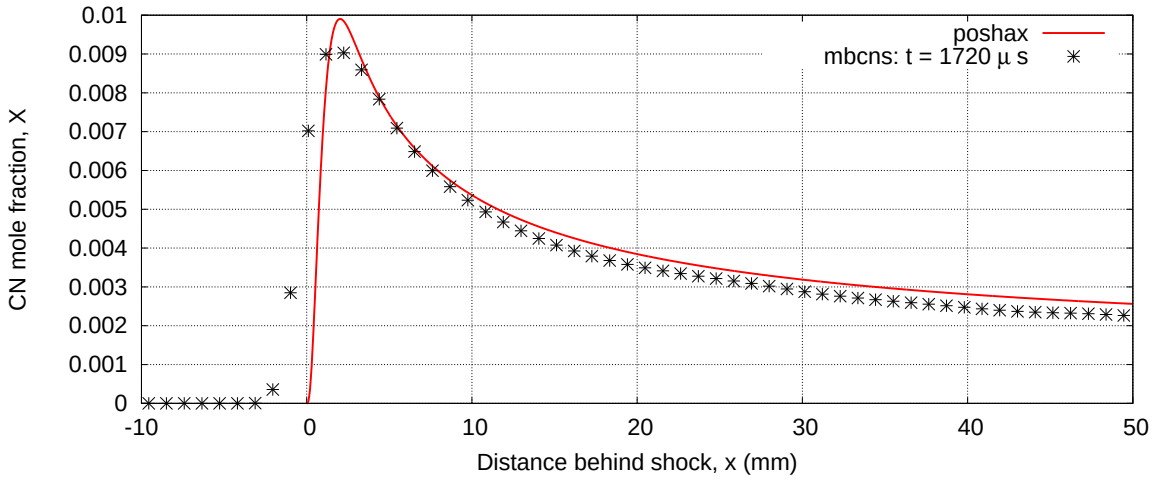

(b) CN mole fraction

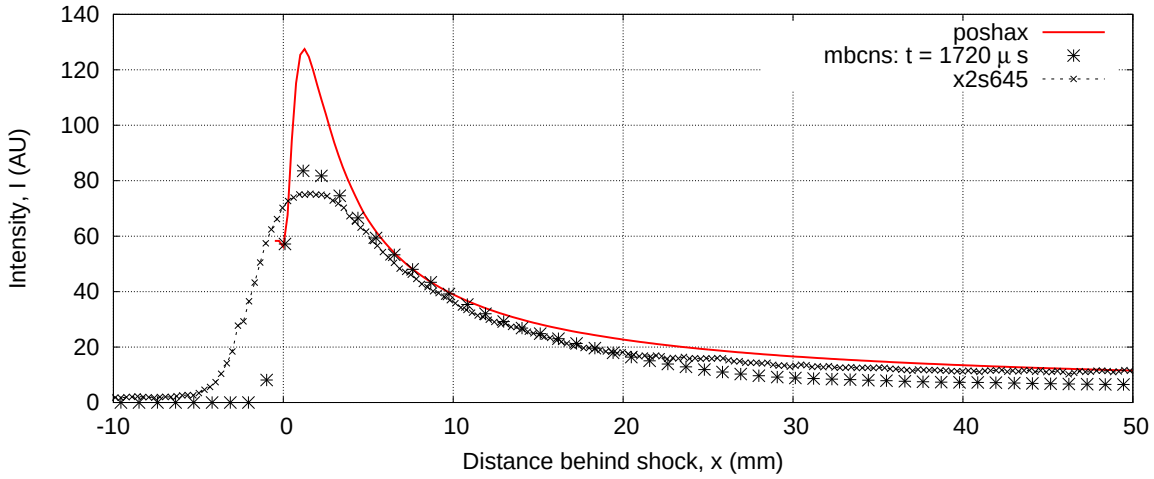

(c) Radiative intensity $310\,nm \leq \lambda \leq 450\,nm$

Figure 43: Comparison of one-dimensional and axisymmetric (centerline, $t = 1720\,\mu$s) profiles for the 1 Torr Titan condition in X2

5 WHERE TO FROM HERE?

In the flow simulation codes that we have described here, the modelling of unsteady gas-dynamic wave motion, viscous effects and finite-rate chemical processes are all well addressed. Current work is continuing on turbulence modelling, radiation energy exchange and the inclusion of moving pistons in the axisymmetric flow simulation code. With these developments, it should be possible (given sufficient, very large computational resources) to model a free-piston driven shock tunnel or expansion tube from end to end with an axisymmetric flow simulation.

On the software development side, there is a new version of both L1d and mbcns just about ready for general use. The thermochemistry module has been rewritten and generalized so that it can be include a range of thermal nonequilibrium models that are needed to better handle high-temperature radiating flow fields. The axisymmetric flow solver has also been combined with a full three-dimensional flow solver to become the new code `Eilmer3` [65].

6 ACKNOWLEDGEMENTS

It takes a lot of people a lot of hours to design, build and operate both the physical facilities and the flow simulation codes. Beyond the list of authors, material in this paper has come from the efforts of Richard Morgan, David Mee, Tim McIntyre, Paul Petrie, Joanna Austin, Chris Craddock, Ian Johnston, Con Doolan, Richard Goozee, Michael Scott, Matt McGilvray, Carolyn Jacobs and Mike Wendt.

References

[1] S. W. Hiscock, D. Kilpin, and L. J. Drummond. A versatile shock tube and its analytical instrumentation. Technical Report WRE-TR-1819(W), Defence Science and Technology Organisation, South Australia, May 1977.

[2] C. S. Craddock. Computational optimization of scramjets and shock tunnel nozzles. PhD Thesis, The University of Queensland, Australia, August 1999.

[3] R. J. Goozée, P. A. Jacobs, and D. R. Buttsworth. Simulation of a complete reflected shock tunnel showing a vortex mechanism for flow contamination. *Shock Waves*, 15(3-4):165–176, 2006.

[4] P. Barker, A. Bishop, B. Littleton, P. A. Jacobs, and H. Rubinsztein-Dunlop. Flow tagging LEI velocimetry of supersonic flow. In *First Australian Conference on Laser Diagnostics in Fluid Mechanics and Combustion*, pages 192–197, December 1996.

[5] P. A. Jacobs and R. J. Stalker. Mach 4 and mach 8 axisymmetric nozzles for a high-enthalpy shock tunnel. *The Aeronautical Journal*, 95(949):324–334, 1991.

[6] K. Hannemann, R. Krek, and G. Eitelberg. Latest calibration results of the HEG contoured nozzle. In *Proceedings of the 20th International Symposium on Shock Waves*, pages 1575–1580, Singapore, July 1995. World Scientific.

[7] A. J. Neely and R. G. Morgan. The superorbital expansion tube concept, experiment and analysis. *Aeronautical Journal*, 98:97–105, 1994.

[8] R. G. Morgan. *Handbook of Shock Waves*, volume 1, chapter Shock Tubes and Tunnels: Facilities, Instrumentation, and Techniques, Free-Piston Driven Expansion Tubes, pages 603–622. Academic Press, San Diego, 2001.

[9] T.N. Eichmann, A.M. Brandis, D.F. Potter, T.J. McIntyre, and Rubinsztein-Dunlop. Radiating hypersonic flow studies using a super-orbital expansion tube. *40th Thermophysics Conference, Seattle, Washington*, 23 - 26 June 2008.

[10] H. Bernier and J. Gambart. MOOREA, an internal ballistic code for two stage light gas gun study. In *38th Meeting of the Aeroballistic Range Association.*, 1987.

[11] C. P. T. Groth and J. J. Gottlieb. Numerical study of two-stage light-gas hypervelocity launchers. UTIAS Report 327, Institute for Aerospace Studies, University of Toronto., 1988.

[12] J. Lacey and D. Long. A wave diagram computational method with application to a free-piston shock tube. AIAA Paper 90-1378, 1990.

[13] C. P. T. Groth, J. J. Gottlieb, and P. A. Sullivan. Numerical investigation of high-temperature effects in the UTIAS-RPI hypersonic impulse tunnel. *Canadian Journal of Physics*, 69(7):897–918, 1991.

[14] D. G. Edwards, K. C. Phan, and C. V. Hurdle. Computational modelling of the gas flow from a high-enthalpy blast simulator. In *17th International Symposium on Shock Waves and Shock Tubes*, pages 891–896, 1989.

[15] V. L. Streeter and E. B. Wylie. *Fluid Mechanics*. McGraw-Hill Ryerson, Toronto, 1981.

[16] H. Schlichting. *Boundary-Layer Theory.* McGraw-Hill, New York, 1968.

[17] A. K. Jain. Accurate explicit equation for friction factor. *American Society of Civil Engineers Journal of the Hydraulics Division*, 102(HY5):674–677, 1976.

[18] J. P. Holman. *Heat Transfer*. McGraw Hill, New York, 1981.

[19] H. W. Liepmann and F. E. Goddard. Note on the Mach number effect upon the skin friction of rough surfaces. *Journal of the Aeronautical Sciences*, 24(10):781, 1957.

[20] C. R. Wilke. A viscosity equation for gas mixtures. *Journal of Chemical Physics*, 18:517–519, 1950.

[21] P. K. Sweby. High resolution schemes using flux limiters for hyperbolic conservation laws. *SIAM J. Numer. Anal.*, 21:995–1010, 1984.

[22] P. A. Jacobs. An approximate Riemann solver for hypervelocity flows. *A.I.A.A. Journal*, 30(10):2558–2561, 1992.

[23] S. Osher and F. Solomon. Upwind difference schemes for hyperbolic systems of conservation laws. *Mathematics of Computation*, 38(158):339–374, 1982.

[24] S. K. Godunov (Ed). *Numerical Solution of Multidimensional Problems in Gasdynamics.* Nauka, Moscow, 1976.

[25] J. J. Gottlieb and C. P. T. Groth. Assessment of Riemann solvers for unsteady one-dimensional inviscid flows of perfect gases. *Journal of Computational Physics*, 78(2):437–458, 1988.

[26] H. Gurgenci and W. R. B. Morrison. Rocketdyne shock tunnel: Diaphragm research and development program. WBM Report 6058, 1989.

[27] P. A. Jacobs. MB_CNS: A computer program for the simulation of transient compressible flows. Department of Mechanical Engineering Report 10/96, The University of Queensland, Brisbane, December 1996.

[28] P. A. Jacobs. Single-block Navier-Stokes integrator. ICASE Interim Report 18, 1991.

[29] E. Oran and J. Boris. *Numerical Simulation of Reactive Flow*. Cambridge University Press, New York, USA, 2nd edition, 2001.

[30] W. Gropp, E. Lusk, and A. Skjellum. *Using MPI Portable Parallel Programming with the Message-passing Interface.* The MIT Press, Cambridge, Massachusetts, 1994.

[31] M. N. Macrossan. The equilibrium flux method for the calculation of flows with non-equilibrium chemical reactions. *Journal of Computational Physics*, 80(1):204–231, 1989.

[32] Y. Wada and M. S. Liou. A flux splitting scheme with high-resolution and robustness for discontinuities. AIAA Paper 94-0083, January 1994.

[33] G. D. van Albada, B. van Leer, and W. W. Roberts. A comparative study of computational methods in cosmic gas dynamics. ICASE Report 81-24, 1981.

[34] P. J. Petrie-Repar. Numerical simulation of diaphragm rupture. PhD Thesis, The University of Queensland, Brisbane, Australia, December 1997.

[35] D. F. Potter, R. J. Gollan, T. Eichmann, T. J. McIntyre, R. G. Morgan, and P. A. Jacobs. Simulation of CO_2-N_2 expansion tunnel flows for the study of radiating shock layers. AIAA Paper 2008-1280, 2008.

[36] B. J. McBride and S. Gordon. Computer program for calculation of complex chemical equilibrium compositions and applications. Part 2: Users manual and program description. Reference Publication 1311, NASA, 1996.

[37] S. Gordon and B. J. McBride. Computer program for calculation of complex chemical equilibrium compositions and applications. Part 1: Analysis. Reference Publication 1311, NASA, 1994.

[38] E.S. Oran and J.P. Boris. *Numerical Simulation of Reactive Flow*. Cambridge University Press, New York, USA, 2nd edition, 2001.

[39] E. Fehlberg. Low-order classical Runge-Kutta formulas with stepsize control and their application to some heat transfer problems. Technical Report R-315, NASA, 1969.

[40] D. R. Mott. *New Quasi-Steady-State and Partial-Equilibrium Methods for Integrating Chemically Reacting Systems*. PhD thesis, University of Michigan, 1999.

[41] T.R. Young and J.P. Boris. A numerical technique for solving stiff ordinary differential equations associated with the chemical kinetics of reactive-flow problems. *Journal of Physical Chemistry*, 81(25):2424–2427, 1977.

[42] K. Hannemann, P. A. Jacobs, J. M. Austin, A. Thomas, and T. J. McIntyre. Transient and steady-state flow in a small shock tube. In A. Paull et al., editor, *21st International Symposium on Shock Waves*, Paper 2630, Singapore, July 1997. World Scientific.

[43] C. E. Smith. The starting process in a hypersonic nozzle. *Journal of Fluid Mechanics*, 24:625–640, 1966.

[44] R.J. Stalker. Use of argon in a free piston shock tunnel. In *AIAA Plasmadynamics Conference, Monterey, California, March 2-4, AIAA Paper No. 66-169*, 1966.

[45] A. Paull and R.J. Stalker. Test flow disturbances in an expansion tube. *Journal of Fluid Mechanics*, 245:493–521, 1992.

[46] R.J. Stalker. A study of the free-piston shock tunnel. *AIAA Journal*, pages 2160–2165, 1967.

[47] K. Itoh, S. Ueda, T. Komuro, K. Sato, M. Takahashi, H. Myajima, H. Tanno, and H. Muramoto. Improvement of a free piston driver for a high-enthalpy shock tunnel. *Shock Waves*, 8:215–233, 1998.

[48] H. Tanno, K. Itoh, T. Komuro, and K. Sato. Experimental study on the tuned operation of a free piston driver. *Shock Waves*, 10:1–7, 2000.

[49] Hans G. Hornung. The piston motion in a free-piston driver for shock tubes and tunnels. Technical Report GALCIT Report FM 88-1, Graduate Aeronautical Laboratories, California Institute of Technology, Jan 1988.

[50] P.A. Jacobs, T.B. Silvester, R.G. Morgan, M.P. Scott, R.J. Gollan, and T.J. McIntyre. Superorbital expansion tube operation: estimates of flow conditions via numerical simulation. Paper presented to the 43rd AIAA Aerospace Sciences Meeting, Reno, NV, 10-13 January, 2005.

[51] H. Mirels. Test time in low-pressure shock tubes. *The Physics of Fluids*, 6(9):1201–1214, 1963.

[52] A.M. Brandis, R.J. Gollan, M.P. Scott, R.G. Morgan, P.A. Jacobs, and P.A. Gnoffo. Expansion tube operating conditions for studying nonequilibrium radiation relevant to Titan Aerocapture. *42nd Joint Propulsion Conference and Exhibit, 9 - 12 July 2006, Sacramento, California*, 2006.

[53] Pascal Boubert. TC2 - M1: Definition of shock tunnel test-cases for gas radiation prediction in Mars-like atmosphere. In *Rebuilding of Selected Test Cases, Radiation Workshop in Roma*, volume ESA SP 629, pages 12 –, Rome, Italy, 2006. European Space Agency.

[54] M.P. Scott. *Development and Modelling of Expansion Tubes*. Phd thesis, School of Engineering, St Lucia, QLD, June 2006.

[55] S. Gordon and B.J. Mcbride. Computer program for calculation of complex chemical equilibrium compositions and applications. Part 1: Analysis. NASA Reference Publication 1311, United States, 1994.

[56] R.J. Bakos and R.G. Morgan. Chemical recombination in an expansion tube. *AIAA Journal*, 32(6):1316 – 1319, 1994.

[57] C.S. Park. Assessment of two-temperature kinetic model for ionizing air. *Journal of Thermophysics and Heat Transfer*, 3(3):233–244, 1989.

[58] C.S. Park, J.T. Howe, R.L. Jaffe, and G.V. Candler. Review of chemical-kinetic problems of future NASA missions, II: Mars entries. *Journal of Thermophysics and Heat Transfer*, 8(1):9 – 22, 1994.

[59] A.M. Brandis, R.G. Morgan, T.J. McIntyre, and P.A. Jacobs. Nonequilibrium radiation intensity measurements in simulated Titan atmospheres. *40th Thermophysics Conference, Seattle, Washington*, 23 - 26 June 2008.

[60] R.J. Gollan, C.M. Jacobs, P.A. Jacobs, R.G. Morgan, T.J. McIntyre, M.N. Macrossan, D.R. Buttsworth, T.N. Eichmann, and D.F. Potter. A simulation technique for radiating shock tube flows. *26th International Symposium on Shock Waves (ISSW26)*, July 2007.

[61] R.J. Gollan. *Computational Modelling of High-Temperature Gas Effects with Application to Hypersonic Flows*. PhD thesis, School of Engineering, The University of Queensland, June 2008.

[62] D.F. Potter. Validation of Aerothermo-Chemistry Models for Re-Entry Applications – TN 3.5: Comparison with Experiments. Technical Note 3.5, European Space Agency, European Space Research and Technology Centre, Noordwijk, The Netherlands, May 2009.

[63] J Olejniczak, M Wright, D Prabhu, N Takashima, B Hollis, E V Zoby, and K Sutton. An Analysis of the Radiative Heating Environment for Aerocapture at Titan. *AIAA Paper No. 2003-4953*, 2003.

[64] Tahir Gökçen. N_2 - CH_4 -Ar Chemical Kinetic Model for Simulations of Atmospheric Entry to Titan. *37th AIAA Thermophysics Conference, 28 June - 1 July 2004, Portland, Oregon*, 2004.

[65] P. A. Jacobs and R. J. Gollan. The Eilmer3 code: User guide and example book. Mechanical Engineering Report 2008/07, The University of Queensland, Brisbane, Australia, 2010.

A Nomenclature, Units

A	: duct area or cell area, m^2
a	: speed of sound, m/s
C_v	: specific heat at constant volume, $J/kg \cdot K$
C_p	: specific heat at constant pressure, $J/kg \cdot K$
D	: (effective) duct diameter, m
E	: total energy per unit mass $e + \frac{1}{2}u^2$, J/kg
e	: specific internal energy, J/kg
$\overline{F}$	: array of flux terms
F_p	: piston friction force, N
F_{wall}	: wall shear force due to viscous effects, N
F_{loss}	: effective force due to pipe fitting losses, N
f	: Darcy-Weisbach friction factor
f	: species mass fraction
H	: total enthalpy, J/kg
h	: specific enthalpy, J/kg
h	: heat transfer coefficient, J/s/m^2/K
$\hat{i}, \hat{j}$	: unit vectors for the cartesian coordinates
i, j	: cell index
K	: viscous loss coefficient
k	: coefficient of thermal conductivity
L	: length, m
M	: Mach number
MW	: molecular weight
m	: mass of fluid in a Lagrangian cell, kg
m_p	: piston mass, kg
n	: direction cosine
n	: driver gas polytropic index
$\hat{n}, \hat{p}$	: unit vectors for the cell interface
P, p	: pressure, Pa
$p_{D,He,0}$	: initial partial fill pressure of Helium in driver tube
$p_{D,Ar,0}$	: initial partial fill pressure of Argon in driver tube
Pr	: Prandtl number
p_{rupt}	: primary diaphragm rupture pressure, MPa
Q	: source vector in the gas-dynamic equations
q	: (`L1d2`) heat transfer rate, J/s
q	: (`mbcns2`) heat flux, W/m^2
R	: gas constant, $J/kg \cdot K$
R_0	: universal gas constant, $8.314\ J/mole \cdot K$
Re	: Reynolds number
r	: tube or duct radius, m
r	: radial coordinate, m
S	: control surface of the cell
St	: Stanton number
$\overline{U}_L, \overline{U}_R$	: Riemann invariants

T : temperature, K
t : time, s
U : state vector in the gas-dynamic equations
u : velocity, m/s
u_p : piston velocity, m/s
u_{rupt} : piston velocity at diaphragm rupture, m/s
U_{ref} : reference piston speed for constant driver pressure
V : cell volume, compression tube volume, m^3
V : piston velocity, m/s
v : volume, m^3
$\dot{w}$: work/unit time done by the wall shear stress, J/s
X, x : piston position, m
x, y, z : cartesian coordinates, m
Z : intermediate variable for the Riemann solver
α : weighting parameter
β : stretching parameter
β : piston over-driver parameter ($= u_{rupt}/U_{ref}$)
γ : ratio of specific heats
$\Delta\pm$: intermediate variable for interpolation
ϵ : absolute size of pipe roughness elements
λ : compression ratio for the free-piston driver
λ : second coefficients of viscosity, Pa.s
Λ : compressibility factor
μ : viscosity, Pa.s; friction coefficient
π : 3.14159...
ρ : density, kg/m^3
γ : ratio of specific heats
τ : wall shear stress, Pa
Ω : recovery factor

Subscripts

A	: reservoir
$A, 0$	: reservoir initial condition
acc	: acceleration tube
aw	: adiabatic wall condition
B	: back of piston
D	: driver tube
$D, 0$	: driver tube initial condition
exp	: experimentally measured quantity
F	: front of piston
f	: friction value
i	: cell index, inviscid
j	: cell index
$j \pm \frac{1}{2}$	: interface indices
$L,\ R$	: left and right states for the Riemann solver or flux calculator
$loss$	: pipe fitting value
m	: quantity at piston inflection point when acceleration is zero
max	: maximum value
n	: normal to the cell interface
p	: tangent to the cell interface
	: piston
s	: nozzle supply (stagnation) condition
	/ species index
sec	: secondary driver tube
shk	: shock tube
tt	: test time
v	: viscous
$wall$	: wall condition
x, y	: coordinate directions
0	: stagnation property
1, 2	: pre- and post-incident shock conditions in the shock tube

Superscripts

$*$	: intermediate state for the Riemann solver
	/ Eckert reference conditions
$\overline{(\cdots)}$	: cell average